THE MARSHFIELD TERRANE: REDEFINITION OF ORIGIN THROUGH ZIRCON GEOCHRONOLOGY AND GEOCHEMISTRY

A THESIS SUBMITTED TO THE GRADUATE SCHOOL
IN PARTIAL FULFILLMENT OF THE REQUIREMENTS
FOR THE DEGREE

MASTER OF SCIENCE
BY

JOSHUAH J. KLIER

DR. SHAWN J. MALONE – ADVISOR

DEPARTMENT OF GEOLOGICAL SCIENCES
BALL STATE UNIVERSITY
MUNCIE, INDIANA
JULY 2019

Abstract

The Marshfield Terrane lies in the present-day Lake Superior region of the United States and was involved in the Paleoproterozoic Penokean Orogeny. The Penokean Orogeny is among the earliest orogenic events in the assembly of ancestral North America, Laurentia. The Penokean Orogeny involved three entities, the Superior Craton, the Pembine-Wausau Terrane and the Marshfield Terrane. The Superior Craton is a hodgepodge of Archean continents and provides the central building blocks for the assembly of Laurentia. The Pembine-Wausau Terrane is a juvenile arc system which was generated at c. 1,890 Ma through ocean-oceanic subduction under the Superior Craton. This arc system collided with the Superior Craton at c. 1,875 Ma. The Marshfield Terrane collided with the Superior Craton and the Pembine-Wausau Terrane at c. 1,850 Ma, but there are questions about its origin. The Marshfield Terrane has an Archean basement, and therefore cannot be a juvenile arc system. Historical studies have provided very little data on the Marshfield Terrane. The Marshfield Terrane is quite small, so it is possible that it may be a rift fragment of another Archean craton. The most spatially logical choices for a parent terrane are the Superior Craton, the Medicine Hat Block and the Wyoming Province. A better understanding of the Marshfield Terrane may illuminate a better understanding for the formation of Laurentia and may offer additional clues for Paleoproterozoic plate tectonics as modern-style, subduction related plate tectonics has been disputed this early in Earth's history. To investigate the Marshfield Terrane, zircon U-Pb geochronology and Lu-Hf geochemistry, in association with whole rock geochemistry and petrographic analyses, were utilized. U-Pb zircon geochronology in this study yielded ages for four samples, which were combined with ages from previous studies. The Marshfield Terrane is now defined as a mid-Mesoarchean to late Orosirian (c. 3.2 – 1.8 Ga) crustal block which zircon yield a bimodal

distribution of initial Hf values. These range from somewhat depleted (+0.4 – +5.3) samples from intermediate metaigneous rocks in the west, and relatively enriched (-6.3 – -15.4) values from more felsic units to the east. Most of the crystallization ages described herein are consistent with those previously documented in the Penokean Orogeny, and Lu-Hf agree with previous Sm-Nd studies which indicate older source environments. Whole rock geochemistry suggests andesitic protoliths for many of our samples. Trace element and rare earth element (REE) on normalized multi-element variation diagrams display strongly negative Ta-Nb-Ti anomalies, suggestive of involvement of subduction in their formation. The Marshfield Terrane has similar ages and εHf values as the northern Wyoming Province and the Medicine Hat Block, which presents a possible genetic relationship.

Introduction

The assemblage of the North America continent has long been studied by geologists, but much of its evolution is still in question due to its vast complexity. This complexity results from numerous terranes and island arcs which have coalesced over time to create what we see today (figs. 1 + 2) (Sims et al., 1989; Sims et al., 1993; Chandler et al., 2007; Schultz and Cannon, 2007; Whitmeyer and Karlstrom, 2007; Craddock et al., 2013; Wunderman et al., 2018). While the assembly of Laurentia have long been studied by geologists much of its evolution is still in question due to its vast complexity. This complexity results from numerous terranes and island arcs which have coalesced over time to create what we see today and have overprinted previous events (figs. 1 + 2) (Sims et al., 1989; Sims et al., 1993; Chandler et al., 2007; Schultz and Cannon, 2007; Whitmeyer and Karlstrom, 2007; Craddock et al., 2013; Wunderman et al., 2018).

One of the many pieces of Archean crust involved in the assembly of ancestral North America (Laurentia) is the Marshfield Terrane, part of the Paleoproterozoic Penokean Orogeny.

The orogen is the oldest Proterozoic accretionary orogen (Van Schmus et al., 2007), and is responsible for the amalgamation of the Superior Province, and the magmatic Pembine-Wausau Terrane and Marshfield Terrane. The two magmatic terranes were originally believed to be a collective unit by early studies (Maass et al., 1980; Ueng and Larue, 1988; Anderson and Cullers, 1987; Sims, 1976; Van Schmus, 1976; Sims et al., 1987).

While the Pembine-Wausau Terrane and the Superior Province have well documented origins, the Marshfield Terrane has been generally disregarded. A possible relationship between the Superior Craton and the Marshfield Terrane was explored through the utilization of lead (Pb) isotopes by Van Wyck and Johnson (1997). Their results suggested the Marshfield Terrane and the Superior Province are not related due to the respective differences in $^{206}Pb/^{204}Pb$ versus $^{207}Pb/^{204}Pb$ curve from the Archean to Paleoproterozoic. This observation does not provide an answer for whether the Marshfield Terrane is a rift fragment of other Archean cratons or if it is a unique microcontinent. This issue is compounded because Archean crust is widespread across the world (Martin, 1994; Whitmeyer and Karlstrom, 2007), so there are several possible parental terranes. By matching the Marshfield Terrane with a conjugate region, we can then obtain a better understanding of Proterozoic tectonic processes and reconstruction of Laurentia. Improving our understanding of the Penokean Orogeny may help constrain the style of plate tectonics that operated in the Paleoproterozoic. A modern style of tectonics is assumed by most models (Sims et al., 1989; Schultz and Cannon, 2007; Whitmeyer and Karlstrom, 2007) but there is still debate on how far into Earth's past the uniformitarian approach can be applied.

To better characterize the Marshfield Terrane, rock samples were analyzed through petrography, whole-rock major and trace element geochemistry. In addition, a subset of samples will be processed for zircon. The zircon will be analyzed for U-Pb geochronology and Lu-Hf

isotope geochemistry. The U-Pb ages will improve our understanding of the timing of geological events in the Marshfield Terrane. The Lu-Hf system traces the evolution of the zircon with regards to a mantle magma source (e.g., Kinney and Maas, 2003) and helps to link the host rock evolution to plate tectonic settings. When all data are compiled, the origin and subsequent evolution of the Marshfield Terrane and its associated impacts into Paleoproterozoic plate tectonic processes will be clearer. The primary mission of this work is to explore the Marshfield Terrane to learn about its Archean basement. Is it a rift fragment of other Archean cratons or is it a unique entity? Answering these questions will help us better understand the assemblage Laurentia.

Laurentian assembly during the Proterozoic

Laurentia, the ancestral North American craton, has a central core known as the Canadian Shield (Whitmeyer and Karlstrom, 2007) that was assembled in ~100 Ma (Craddock et al., 2013) through multiple tectonic events. The Marshfield Terrane is among the earliest pieces to this orogen, but its role is unclear. Understanding the mechanisms for Late Archean-Early Proterozoic evolution of Laurentia has been complex because several key orogenic events in the assembly of early Laurentia have Nd/Hf model ages which are much older than their U-Pb crystallization ages (Barth et al., 2000). The specific tectonic processes responsible for Laurentian coalescence has been debated in the recent literature with three major models proposed (Fisher et al., 2010): 1) A slow, continuous build of juvenile crust (Karlstrom et al., 1999; Whitmeyer and Karlstrom, 2007), 2) reworking of existing Laurentian crust (Hatcher et al., 2004), and 3) a hodgepodge of exotic terrane accretion during the Grenville orogeny (Sinha and McLelland, 1999). Regardless of how Laurentia grew, it is confirmed that the southern edge of Laurentia was the site of tectonic growth on the craton's successive margins (Schultz and

Cannon, 2007; Whitmeyer and Karlstrom, 2007). The Penokean Orogeny was one of the first steps in the assembly of Laurentia (McDannell et al., 2018) along this southern margin. The Whitmeyer and Karlstrom (2007) figures are used as a visual explanation for Laurentian assembly. Figure 1 (Whitmeyer and Karlstrom, 2007) depicts the hypothesized complex assemblage of Laurentia by 535 Ma. The focus of my research lies on one aspect of the building of Laurentia, the Penokean orogeny, that is still somewhat poorly understood (Chandler et al., 2007) (Fig. 2 & 3) and has been difficult for geologists to reconstruct in precise detail because of overprinting with successive orogeneses. The orogeny is classified by Sims (1989) as having two distinct units, one to the north and the other to the south. These two units are the Pembine-Wausau Terrane and Marshfield Terrane (also known as the Wisconsin Magmatic Terranes) and they are distinguished by their lithology, structural variation and by their position relative to the Eau Pleine shear zone, interpreted as a paleosuture zone. (Sims et al., 1989).

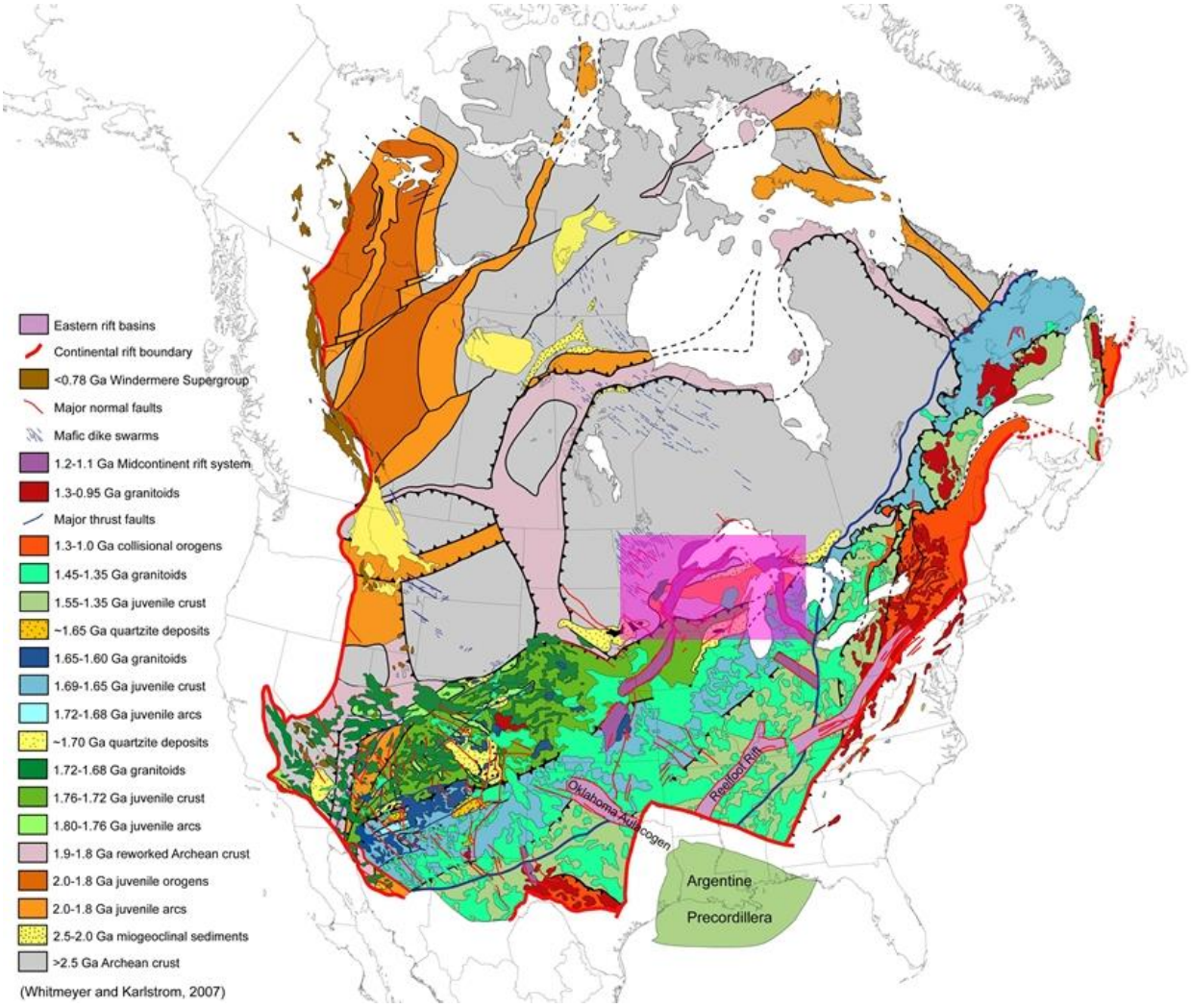

Figure 1: Reconstruction of Laurentia by 535 Ma. The pink box has been added to locate the Penokean orogen. Modified from Whitmeyer and Karlstrom (2007).

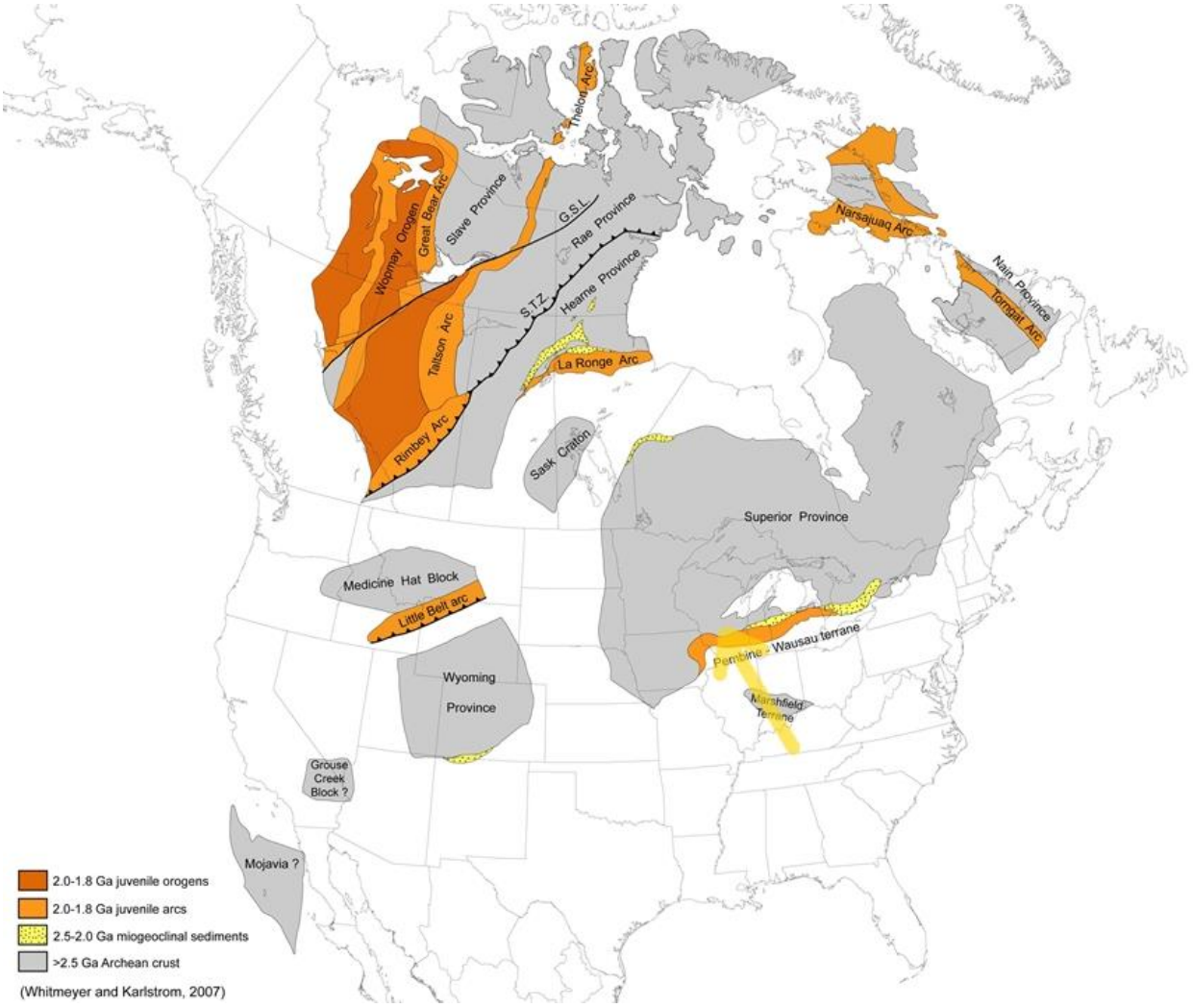

Figure 2: Reconstruction of the early formation of Laurentia. Below the Superior Province is the Pembine-Wausau Terrane which is seen accreting to it. Some of these features will be lost due to overprinting from accretion of the Marshfield Terrane and future orogeneses it as shown in figure 1. While Whitmeyer and Karlstrom's (2007) model works well for what we see today, it does not answer the question of origin for the Marshfield Terrane. (Whitmeyer and Karlstrom, 2007).

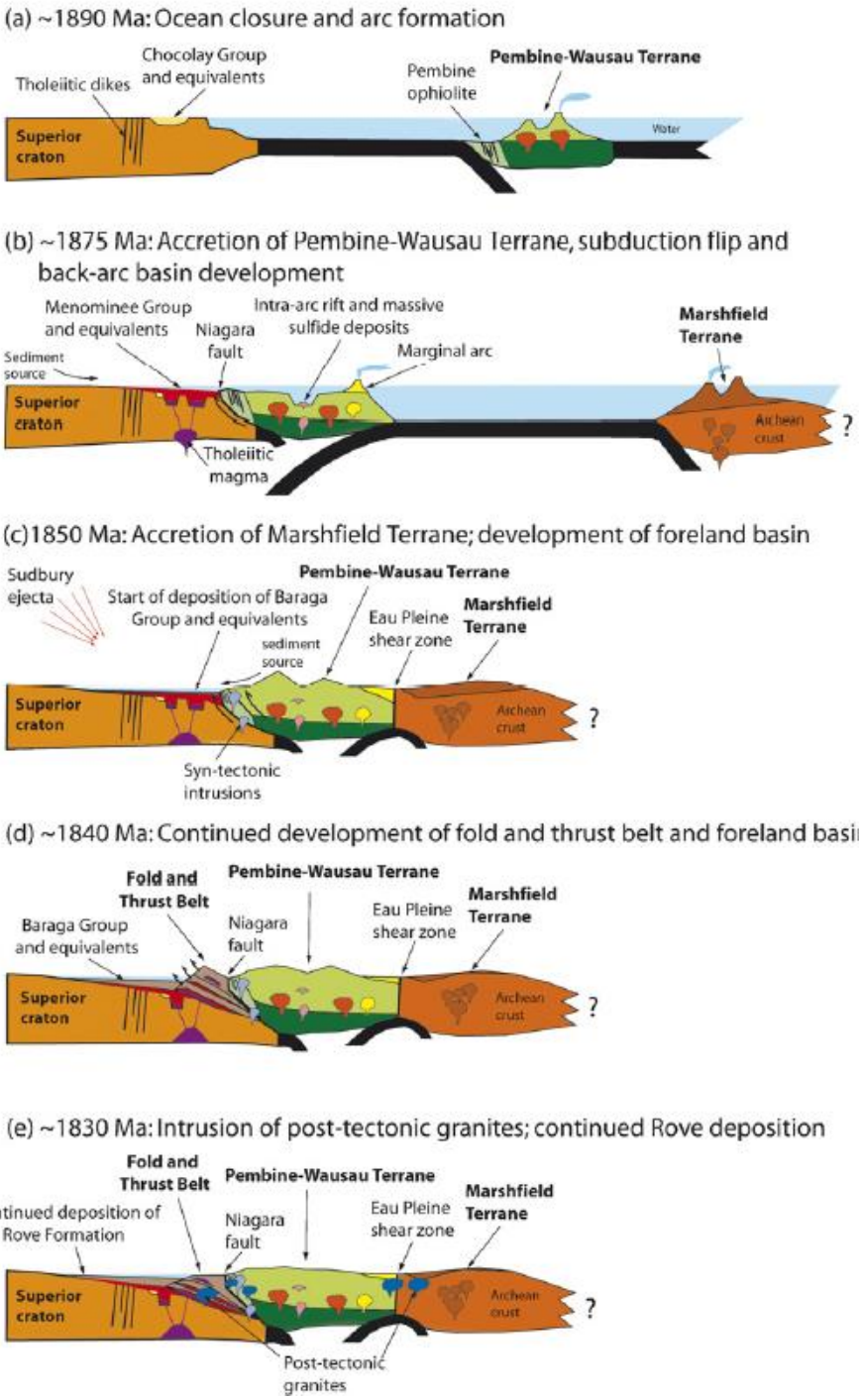

Figure 3: A synthesis and reconstruction of the events of the Penokean orogeny. While the order of events is agreed upon, the origin of the Archean basement for the Marshfield Terrane is not clear (Schulz and Cannon, 2007).

The Penokean Orogeny

The Penokean Orogeny occurred on the southern margin of the Superior Province (Sims et al., 1989; Schulz and Cannon, 2007; Whitmeyer and Karlstrom, 2007) (Fig 2) due to the initiation of oceanic-oceanic subduction at 1,890 Ma (Sims et al., 1989). The resulting subduction zone created a juvenile arc, now known as the Pembine-Wausau Terrane. This arc was subsequently accreted against the Superior Province by c. 1,875 Ma (Sims et al., 1989; Schulz and Cannon, 2007) (Fig. 3A). The collision caused the Pembine-Wausau Terrane to become uplifted and partially eroded thus creating a fold and thrust belt (Schultz and Cannon, 2007). After the Pembine-Wausau Terrane collided with the Superior Province's margin (Fig. 3B), a new subduction zone formed at the southern edge of Pembine-Wausau Terrane (Schulz and Cannon, 2007). Renewed subduction of oceanic crust caused the Marshfield Terrane to approach and subsequently collide with the Pembine-Wausau Terrane by 1,850 Ma (Fig. 3C) (Stockmal et al., 1987; Sims et al., 1989; Schulz and Cannon, 2007). The Marshfield Terrane's collision caused deformation, uplift, and erosion on the Pembine-Wausau Terrane and generated a fold and thrust belt (Fig. 3D) (Schulz and Cannon, 2007). After the accretion, post-tectonic granites were intruded into all three tectonic elements of the orogeny around 1,835-1,830 Ma, which constrains the termination of the orogeny (Schulz and Cannon, 2007) (Fig. 3E). Later deformation, related to subsequent accretionary events of the Yavapai and Mazatzal orogeneses, often overprints the Penokean deformational history (Sims et al., 1989).

Lithology of the Wisconsin Magmatic Terranes

The Pembine-Wausau Terrane and the Marshfield Terrane are exotic to one other and the Superior margin, and are defined based on lithology, structure and position relative to the Eau Pleine shear zone – the paleosuture of the two terranes (Sims et al., 1989). The Pembine-Wausau

Terrane is a juvenile arc system, while the Marshfield Terrane is an Archean rift fragment or microcontinent upon which an extensive Paleoproterozoic volcanic arc was built.

Pembine-Wausau Terrane

Rocks of the Pembine-Wausau Terrane are interpreted as the remnants of a juvenile arc system and are primarily composed of two main successions: One formed from 1,860 Ma – 1,889 Ma, and one formed from 1,835 – 1,845 Ma (Sims et al., 1989). The Pembine-Wausau Terrane, like the Marshfield Terrane, is intruded by numerous granitic plutons, some of which post-date the orogenic event (Sims et al., 1993).

1,860 – 1,889 Ma sequence

The rocks constituting the 1,886 – 1,889 Ma group consist of andesite, dacite, rhyolitic flows, pyroclastic rocks and basalt that has undergone metamorphism (Sims et al., 1989). These rocks are tightly folded with primary structures partially destroyed and are chemically tholeiitic with depletions in light rare earth elements. Depletion of light rare earth elements is often typical of basalts originating in ophiolite suites and is supported by physical observations of sheeted dikes, serpentinites and plagiorhyolite (Sims et al., 1989). Plagiorhyolite is a common feature of subduction zones due to rapid fractional melting. Additionally, Sims et al. (1989) note that these rocks are chemically similar to more modern calc-alkaline oceanic arcs (Sims et al., 1989) in terms of their geochemical signature.

1,835-1,845 Ma sequence

The rocks that constitute the southern portion of the Pembine-Wausau Terrane include calc-alkaline andesites, dacites and rhyolites (Sims et al., 1989). The slightly younger is likely due to these rocks being created shortly before relocation of the original subduction zone. The

younger sequence of rocks features a greater enrichment in light rare earth elements than the rocks further to the north, which Sims et al. (1989) proposed to be an indication of compositional zoning – a prominent feature of modern arcs (Sims et al., 1989). Unlike the rocks to the north, these rocks are not folded as tightly and feature a lower grade of metamorphism (Sims et al., 1989).

Marshfield Terrane

The Marshfield Terrane consists of variably metamorphosed Archean crystalline basement with Paleoproterozoic meta-igneous rocks; and represents an Archean microcontinent of uncertain origins (Sims et al., 1989; Schulz and Cannon, 2007). Substantial exploration has taken place on the volcanic rocks and intruded granitoids (Sims et al., 1989; Sims et al., 1992; Sims et al., 1993) but age data and subsequent exploration of the source of the Archean basement is nearly nonexistent. Sims et al. (1989) noted only a few ages that were determined to be Archean. Two of those samples had been gathered at their respective sites and reexamined: Gneiss at Jim Falls (thirty-nine) and felsic gneiss at Arbutus dam (forty-one) which had been dated at 2.5 and 2.8 Ga respectively (Sims et al., 1989); however, both ages were recorded by other authors as personal communications. Volcanic rocks of the Marshfield Terrane were produced during the Penokean Orogeny and broken down into two units (Sims et al., 1989). One of the units features felsic to mafic volcanic rocks that are interlayered, dacite porphyry, and sedimentary rocks (Sims et al., 1989). The other unit consists of rhyolite, andesite, quartzite, and conglomerate, which contain clasts of Archean granite gneiss (Sims et al., 1989). These rocks have minimal age data, but two studies have found ages of 1.85 and 1.86 Ga respectively, though neither study was published (Sims et al., 1989). As with the Pembine-Wausau Terrane, there are

numerous granitic intrusions, some of which are undeformed and are used to constrain the end of orogenic deformation in the region (Sims et al., 1989).

Previous Research on the Penokean Orogen

Historical studies on the Marshfield Terrane were often limited by the methods available at time of publication and are further complicated by Phanerozoic cover (Irving and Van Hise, 1892; Blackwelder, 1914; Marsden, 1955; James, 1958; Sims, 1976; Sims and Peterman, 1976; Van Schmus, 1976; Sims, 1980; Afifi et al., 1984; Nelson and DePaolo, 1985; Sims et al., 1987).

Modern

The Wisconsin Magmatic Terranes were reclassified as the Pembine-Wausau and Marshfield by Sims et al. (1989). The orogen was redefined as multiple terranes accreting on the Superior Province's successive margins. The Pembine-Wausau Terrane was then defined to be composed of tholeiitic and calc-alkaline sequences of volcanic rocks, with the Archean gneisses of the Marshfield Terrane accreting afterwards (Sims et al., 1989). Van Wyck and Johnson (1997) suggested a revision of Sims model due to the older age signatures detected in the juvenile Pembine-Wausau Terrane. Van Wyck and Johnson (1997) utilized whole rock Neodymium (Nd) isotopic compositions, combined with Pb isotopic data to confirm the older age signature. Their initial Nd data were found to decrease with proximity to the Superior Province which they interpreted to reflect contamination of plutons which intruded from the Archean crustal basement during the orogenic event (Van Wyck and Johnson, 1997). Van Wyck and Johnson (1997) proposed that the Pembine-Wausau had an Archean basement, and thus was a continental arc system rather than a juvenile arc system; however, this idea was dismissed by

Schulz and Cannon (2007) who preferred a model for magma mixing and partial melting as the source for an older age signature.

Since most of the Wisconsin Magmatic Terranes are concealed by Phanerozoic cover, it has been difficult to constrain them until recently. The Northern Interior Continental Evolution Working Group (NICE) defined the accretionary boundaries based on aeromagnetic compilation (Fig. 4) (NICE Working Group, 2007). Magnetic anomaly data allows the geologist to interpret the magnetic rocks in the Lake Superior region which are covered by more recent, nonmagnetic strata (NICE Working Group, 2007). The study highlights the progressive youth movement to the southwest of Laurentia and highlights the various orogeneses on Laurentia's successive margins (NICE Working Group, 2007).

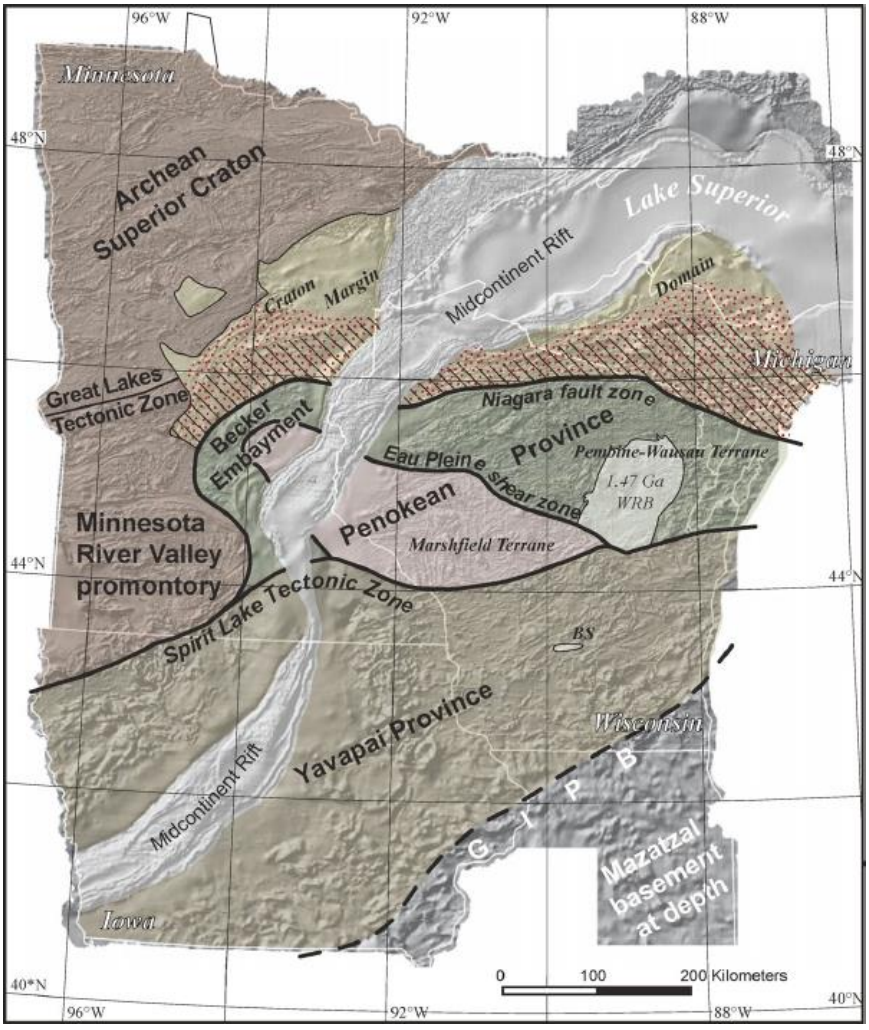

Figure 4: Aeromagnetic compilation data displays the boundaries of the Pembine-Wausau and Marshfield Terrane in relation the Superior Province. Also displayed are the subsequent terranes that followed (NICE Working Group, 2007).

The Penokean Orogeny today

The Penokean Orogeny is now known to have occurred along the southern margin of Laurentia in present-day Wisconsin, Michigan and Minnesota (Schultz and Cannon, 2007). The orogeny is principally responsible for the suturing of the Superior Province, the Pembine-Wausau Terrane and the Marshfield Terrane. The latter terranes are distinguished via structure, lithology and their geographic location to the Eau Pleine shear zone (the paleosuture of the two terranes) (Sims et al., 1989; Sims et al., 1993; Schultz and Cannon, 2007; Whitmeyer and

Karlstrom, 2007). The Pembine-Wausau Terrane is interpreted to be a juvenile arc and the Marshfield Terrane is interpreted to be an Archean microcontinent (Sims et al., 1989; Schultz and Cannon, 2007; Whitmeyer and Karlstrom, 2007). Recently published abstracts (Hannack and Radwany, 2018; Hafften and Radwany, 2018) begin to explore pressures and temperatures of the Penokean Orogeny with respect to the Marshfield Terrane utilizing the Chippewa amphibolite complex part of the Marshfield Terrane exposed in the Chippewa River Valley. Hafften and Radwany (2018) analyzed a garnet amphibolite from the Chippewa amphibolite complex to estimate the pressures and temperatures of metamorphism on the Marshfield Terrane with respect to Penokean orogenesis. A hornblende-plagioclase thermometer suggested temperatures between 606-646°C and pressures between 5.74-6.64 Kbar (Hafften and Radwany, 2018). Hannack and Radwany (2018) utilized a sample from the Eau Claire River Complex, south of Lake Wissota along the Eau Claire River, for edenite-richterite thermometry. The sample had undergone temperatures between 719-769°C (Upper Amphibolite facies) (Hannack and Radwany, 2018). The timing of this metamorphism remains uncertain.

Sedimentological indicators of the Penokean Orogeny

Marquette Range Supergroup

Proximal lithologies of the Superior Province with respect to the Wisconsin Magmatic Terranes provide key evidence for the Penokean Orogeny and may offer lithologic clues of the Penokean Orogeny. The Marquette Range Supergroup is a Paleoproterozoic continental margin assemblage (Schneider et al., 2002) and has been proposed to be deposited between 1.9 to 2.1 Ga (Larue and Sloss, 1980) and records cyclic rifting, ocean development leading up to the Penokean Orogeny creating a foreland basin. It consists of variable sedimentary rocks with some volcanics (Schulz and Cannon, 2007) and may be broken down into three main groups: The

Chocolay Group, Menominee Group, and the Baraga Group (James, 1954; James, 1958; Larue and Sloss, 1980; Larue, 1981a; Larue, 1981b; Schulz and Cannon, 2007). A fourth succession, the Paint River Group is also present, but the unit is structurally complex and its tectonostratigraphic relationship to the Penokean Orogen is not yet clear (Vallini et al., 2006). The Marquette Range Supergroup, found in Michigan and Wisconsin, has been correlated to the Animikie, North Range, and Mille Lac Groups which are found in Minnesota and Ontario, Canada – together they constitute the foreland fold and thrust belt of the Penokean Orogenic event (Schneider et al., 2002). The Supergroup is generally believed to be a progression sequence from intracratonic sedimentation to a passive margin and ends at a foredeep phase with respect to the Chocolay, Menominee and Baraga (Ojakangas et al., 2001), however others have suggested possible development in a back-arc basin (Van Wyck and Johnson, 1997).

Post-Penokean Overprinting

Penokean deformation and metamorphism have been the subject of numerous overprints, making it difficult to determine whether deformation structures are truly Penokean. Several post-Penokean events which have caused overprinting, including: intrusion of a 1.83 Ga suite of granitic-rhyolite plutons, intrusion of a 1.76 Ga succession of granitic plutons, intrusion of the c. 1.47 Ga Wolf River Batholith, and the deformation associated with accretion in the Yavapai-Mazatzal provinces.

Wisconsin Gravity Minimum

While Yavapai-Mazatzal deformation (Magnani et al., 2004) may have affected the Marshfield Terrane, the intrusion of the Wolf River Batholith creates more uncertainty. The Wisconsin Gravity Minimum, which is associated with the 1.5 Ga Wolf River Batholith, extends

through the Wisconsin Magmatic Terranes (Allen and Hinze, 1991). The Wisconsin Gravity Minimum is most prominently documented where the Wolf River Batholith outcrops (Fig. 5), but it extends through the Marshfield Terrane and the Pembine-Wausau Terrane (Allen and Hinze, 1991). The anomaly is produced by a density contrast between the batholith and the Penokean rocks (Allen and Hinze, 1991). Allen and Hinze (1991) hypothesized the rocks, which lie in and above the Wisconsin Magmatic Terranes, may have been emplaced through Eau Pleine Shear Zone which is the paleosuture between the two Magmatic Terranes. The paleosuture between the Pembine-Wausau Terrane and the Marshfield Terrane is not a simple suture between the two terranes; rather, it is a zone of juxtaposed rock formed in unique tectonic environments. These were translated from their original location by multiple thrust faults resulting in a juxtaposition of volcanic rocks, sedimentary rocks and the Archean basement (Sims et al., 1992). Due to the density difference, the batholith may have also experienced differential uplift post deposition (Allen and Hinze, 1991). The presence the intrusion is hypothesized to have influenced the evolution of the craton by: 1. Controlling the location of a Midcontinent rift system dated at 1.1 Ga, and 2. Because it is prominently covered by other strata, it indicates that the area has been tectonically stable since its intrusion (Allen and Hinze, 1991). As the batholith lies above the Penokean rocks in many areas, the Penokean rocks have been largely protected from erosion, but also causes them to be inaccessible and may have subjected them to some amount of contact or regional metamorphism (Allen and Hinze, 1991).

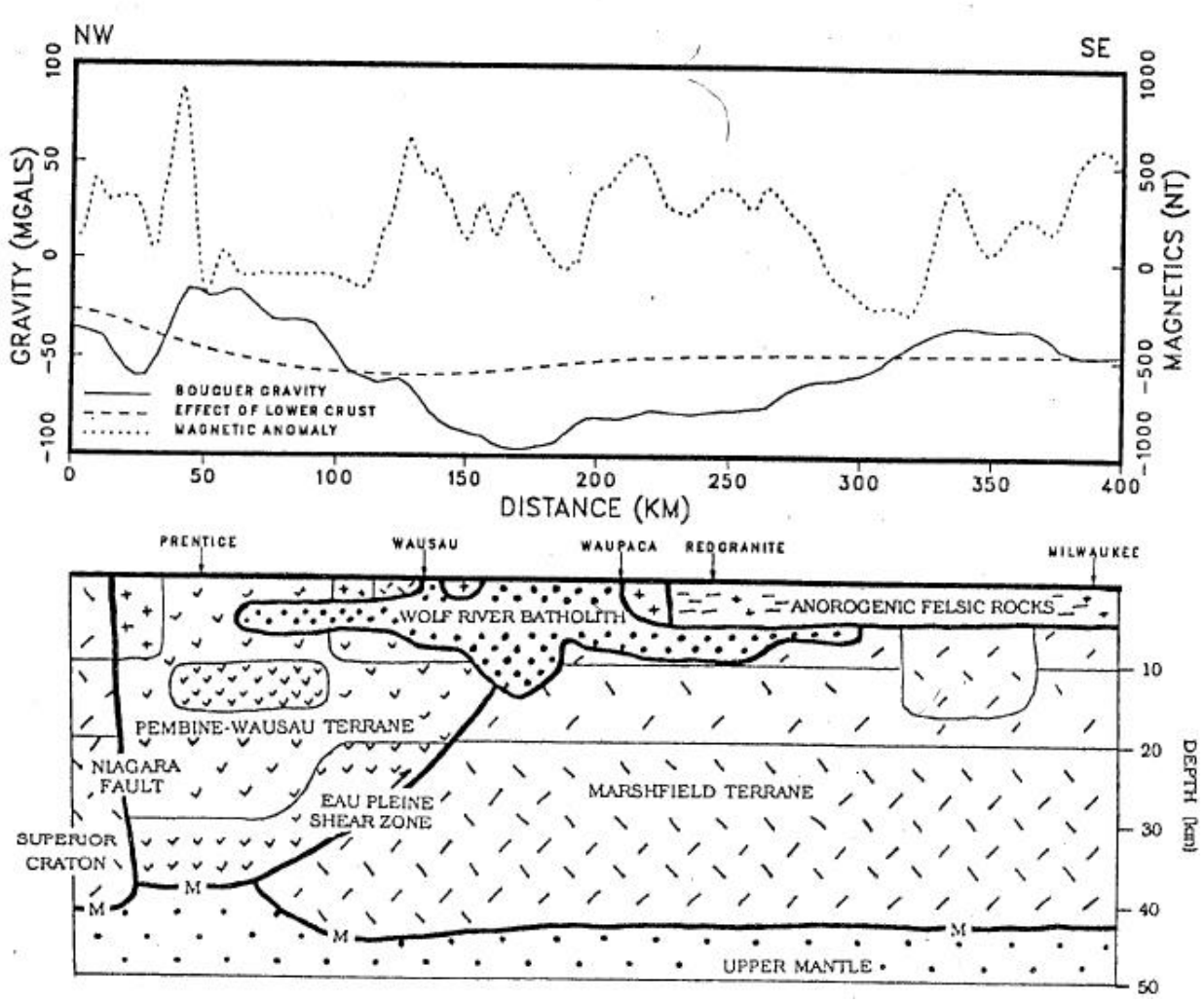

Figure 5: The Wisconsin Gravity anomaly is created due to the Wolf River Batholith which may have been intruded through the Eau Pleine Shear Zone. The body may be responsible for altering the geologic clocks of some zircons (Allen and Hinze, 1991).

Superior Province Lithologies

General geology

While the Marshfield Terrane does not appear to be related to the Superior Province with respect to Pb isotopes (Van Wyck and Johnson, 1997), we will review the Superior Province's petrology and geochemistry to test if geochemical/geochronological connections are apparent.

Petrology and geochemistry of the Superior Province

The Superior Province is a hodgepodge of terranes and domains which together form the core of North America (Card, 1990) with most of the crust formation occurring between 2.72 and 2.68 Ga (Percival, 2007). The craton has been tectonically stable since approximately 2.6 Ga, but its outer margins have been overprinted due to Paleoproterozoic and Mesoproterozoic tectonics (Percival et al., 2006). If the Marshfield Terrane is indeed an ancient rift fragment of the Superior Province, then evidence of such a phenomenon may exist in the trace element geochemistry. Archean felsic metavolcanics in several areas of the Superior Province of the Canadian Shield may be broken down into three major groups on a basis of trace element geochemistry: FI, FI, FIIIa and FIIIb (Lesher et al., 1986). The FI - FIII domains have each been identified in several areas of the Abitibi Belt, Wabigoon Belt, and the Uchi Belt (Lesher et al., 1986). The terranes lie along the southern edge of the Superior Province and provide an excellent to test the relationship between the southern margin of the Superior Craton and the Marshfield Terrane.

The Abitibi Terrane has been interpreted as an oceanic arc setting in which volcanic rocks formed between 2.77 – 2.69 Ga and plutonic rocks were intruded between 2.74 – 2.65 Ga with Nd model ages depicting a source which is less than 2.8 Ga (Percival et al., 2012). The Wabigoon area consists of two sub provinces where the western half is defined by oceanic crust and arc deposits with tonalite-granodiorite plutons (Percival et al., 2006). Volcanic rocks of the western half are tightly constrained between 2.77 – 2.71 Ga with plutonic intrusions occurring between 2.74 – 2.66 Ga (Percival et al., 2012). Nd model ages also reflect a source younger than 2.8 Ga (Percival et al., 2012). The eastern half of the Wabigoon province constitutes of Mesoarchean and Neoarchean greenstone belts with granitic plutons. The Uchi domain consists

of volcanic rocks (2.99 – 2.72 Ga) and plutonic rocks (2.98 – 2.68 Ga) with Nd model ages less than 3.0 Ga (Percival et al., 2012).

FI-FIII

The FI group is comprised of dacites and rhyodacites that feature steeply dipping REE patterns under chondrite normalization with a pronounced abundance in strontium (Lesher et al., 1986). Examples of this domain may be found in localities of the Abitibi belt, Wabigoon belt, and the Uchi belt. Anomalies of europium are weakly negative or positive, and there are low abundances of high field strength elements (Lesher et al., 1986). REE patterns for the FII group, comprised of rhyodacites and rhyolites, have small slopes and their europium anomalies vary per sample (Lesher et al., 1986). The abundances of the high field strength elements are higher than FI and strontium abundances are less pronounced than FI. Examples of this domain may also be found in certain localities of the Abitibi, Wabigoon, and the Uchi belts. FIII felsic metavolcanics are broken into two groups, a and b (Lesher et al., 1986). Both groups represent rhyolites and high silica rhyolites with nearly flat REE patterns (Lesher et al., 1986). They differ in their abundances of scandium, high field strength elements and their europium anomalies. FIIIa typically feature moderately negative europium anomalies, moderate abundances of the high field strength elements and high abundances in scandium whereas FIIIb have pronounced negative europium anomalies with low abundances of scandium and strontium, and high abundances of high field strength elements (Lesher et al., 1986). FIIIa may be found in the Abitibi belt, whereas FIIIb has been identified in both the Abitibi belt and the Uchi belt (Lesher et al., 1986).

Hafnium geochemical analyses on the Superior Province

Hafnium isotopic studies on zircons derived from Archean crust of the southern Superior Province in Canada have been reported separately by Smith et al., (1987). They reflect wide variation as εHf ranges from 9.2 – -1.3 (Smith et al., 1987). Whole-rock εHf on basaltic rocks (+8.7 – +11.3) indicate model ages between 3,100-2,900 Ma (Smith et al., 1987). Lower εHf have been found in felsic samples (-1.3 – + 1.4) suggest the remelting of older crust and is comparatively lower than intermediate rocks that have εHf of +1.4 – +3.9 (Smith et al., 1987).

Age domains of the Superior Province

Other entities in the Superior Province are more tough to compare with respect to the Marshfield Terrane because data paucity for the Late Archean. The Western portion of the Superior Province is composed of the following domains: Northern Superior Superterrane, North Caribou Superterrane, English River Terrane, Winnipeg River Terrane, Wabigoon Terrane, Quetico Terrane, Wawa Terrane, Oxford-Stull Domain and the Kapuskasing uplift (Percival, 2007; Percival and Helmstaedt, 2006). Collectively, the various domains of the Western Superior Province range in age from 3.2 – 2.6 Ga, with detrital zircons dating as far back as 3.9 Ga (Percival, 2007). Rocks from this area principally volcanic and plutonic, many of which have been strongly metamorphosed due to numerous tectonic events which were responsible for orogeneses, faulting, granitic magmatism and regional metamorphism among others (Percival, 2007). The Eastern portion of the Superior Province is composed of the Abitibi Terrane, Pontiac Terrane, Opatica Subprovince, Opinaca Subprovince, Ashuanipi Complex, La Grande Subprovince, Bienville Subprovince, and the Northeastern Superior Province (Percival, 2007). The rocks in this area are dominantly plutonic and volcanic and to a lesser degree metasedimentary (Percival, 2007). Ages range from 3.65 Ga to circa (c.) 2.6 Ga (Percival, 2007).

Methodology

To better investigate the origin of the Marshfield Terrane, samples from the western portion of the Marshfield Terrane were collected in 2016 by Dr. Shawn Malone. The rocks of the Marshfield Terrane have been characterized by XRF for major elements, ICPMS for minor and trace elements, petrographic analyses, zircon U-Pb geochronology, and zircon Lu-Hf isotopic geochemistry.

Whole-Rock Major Element Analysis: X-Ray Fluorescence

Our samples were processed through a Thermo QuanX EC X-ray fluoresce machine (XRF) at Ball State University. Small rock fragments were pulverized to approximately <75µm using a Tungsten-Carbide ring mill. The Tungsten-Carbine ring mill may have small amounts contamination of tungsten, cobalt, tantalum, and niobium (Rollinson, 1993), but this was corrected through standards. In addition to corrections by standards, nearly pure quartz sand was run through the tungsten-carbide ring mill and subsequent to XRF analysis and no pollution was noticeable. The samples were then introduced to a pelletization machine for XRF analysis. Each sample was analyzed under four different conditions to optimize the fluorescent yield for each of the elements of interest. The excitation energies were 6, 12, 16, and 30 keV and each sample was run for 300s. After analysis, the resulting counts were then divided by the current in order to account for the disparities in the current values.

Principles of XRF

The XRF determines the elemental composition of the rocks and is a useful tool in the geological sciences because it is sustainable, whereas LA-ICPMS ablates a portion of the sample (Rollinson, 1993). Unlike the LA-ICPMS which gives data in a narrow focus, XRF reflects whole rock chemistry and determines the elements in the sample by introducing radiation to

them to excite the electrons (Rollinson, 1993). When they become excited, they are ionized and may dislodge from the inner system of the atom and electrons from higher orbital levels will take their place (Rollinson, 1993). Once this occurs, energy is released which is known as fluorescent radiation (Rollinson, 1993). This energy is released because of decreased binding energy of the inner electron's orbital cloud. This energy release is unique to each element and the machine detects these different variations in the sample through its spectrometer and can determine the composition based on how the atoms interact with the X-ray radiation (Rollinson, 1993).

Whole-Rock Trace Element Analysis: Inductively Coupled Plasma Mass Spectrometry

Samples 16MT01 – 09 were sent to SGS Canada for sodium peroxide (Na_2O_2) fusion and trace element analysis. Sodium peroxide is a solution which is basic and strongly oxidizing; it allows refractory minerals (those typically resistant to temperature, pressure and chemical changes) to become soluble (SGS, 2018). These include minerals such as garnets, spinels and other oxides (SGS, 2018). Sodium peroxide fusion is completed at low temperatures (500° C) to reduce the loss of volatile elements (SGS, 2014). Once dissolved, samples were then analyzed by inductively coupled plasma mass spectrometry (ICP-MS) (SGS, 2014) to measure 56 elements for whole rock geochemistry. ICP-MS utilizes a plasma to heat the sample and form positively charged ions (SGS, 2014). The ions pass through the detector where they are separated on their ratio of mass and charge. The signals received by the detector are compared to samples of known concentration to determine the elements available and their associated concentrations (SGS, 2014). ICP-MS is typically very precise and accurate with virtually all elements being able to be detected to the parts-per-million level (SGS, 2014).

Zircon Analysis: Mineral separation

To prepare samples for U-Pb and Lu-Hf analytical work, zircons had to be extracted from the rock. Portions of rock samples were reduced to fine sand-sized particles using a BICO jaw crusher and disk mill pulverizer. This material was fed onto a Gemeni water table, where low density and high-density minerals were separated. The heavy mineral fraction was then passed through a Frantz magnetic separator at three different levels to purify the sample. The low magnetic susceptibility fraction was later passed through a heavy liquids process which utilizes Methylene Iodide (CH_2I_2), which has a density of 3.32 to purify the sample for zircon. Depending on sample size, 60-100 mL of Methylene Iodide is poured into a large separatory funnel. The low-density minerals (e.g. feldspars) float to the surface, while the dense minerals (zircon, pyrite, apatite, among others) sink. After separation the dense mineral fraction is reprocessed through the Frantz magnetic separator for further purification. This fraction is then handpicked for under zircon in alcohol. Zircons were picked from the five most promising samples (16MT03, 16MT04, 16MT05, 16MT07 and 16MT09).

Zircon Analysis: U-Pb and Lu-Hf by Laser Ablation ICP-MS

Our U-Pb and Lu-Hf data were collected utilizing laser ablation inductively coupled plasma mass spectrometry (LA-ICPMS) at the University of Arizona's LaserChron Center. The zircons are mounted and polished to expose grain interiors and imaged with cathodoluminescence (CL) which allows the different domains of the crystals to be identified (Gehrels and Pecha, 2014). To obtain the crystallization age, zircon cores were the primary target of analysis. Once chosen, zircon CL domains were ablated with a Photon Machines Analyte G2 excimer laser equipped with a HelEx ablation cell (Gehrels and Pecha, 2014). The laser creates a spot diameter of 20 microns across, no more than 12 micros deep and an energy density of 5 J/cm^2 for a duration of a few seconds (Gehrels and Pecha, 2014). During ablation, it is carried to

the Element2 HR ICPMS detector which sweeps through the resultant sample ion beam to count for uranium and lead isotopes. Various corrections are made, isotopic ratios of uranium and lead are calculated, and then corrected based on zircon standards (FC, SL and R33). Concordia diagrams were generated through IsoplotR, revealing discordancy and inheritance patterns in the dataset.

For Lu-Hf analyses, a subset of the zircon were chosen based on age and concordancy. Hf analyses are conducted with a Nu HR ICPMS which utilizes a Photon Machines Analyte G2 excimer laser (Gehrels and Pecha, 2014). The laser spot diameter shoots over the U-Pb spot as it is twice as large (Gehrels and Pecha, 2014). The laser will fire for sixty seconds per sample with the same fire power as for U-Pb (Gehrels and Pecha, 2014). Following isotope fractionation, corrections are emplaced based on the aforementioned standards (Gehrels and Pecha, 2014).

Principals of LA-ICPMS

The word laser is an acronym for Light Amplification by the Stimulated Emission of Radiation, and it is used in geochronology to ablate a sample with a narrow and intense beam of radiation allowing for the ablation of atoms, ions, and molecules (Košler and Sylvester, 2003). The ablated materials are measured to determine the isotopic abundances the geologist is interested in (Košler and Sylvester, 2003). The collected data needs to be corrected due to issues with instrument mass discrimination, isotopic fractionation and laser-induced depth dependent fractionation. Fractionation is the separation of isotopes from a parent element during naturally occurring processes because of mass differences between their atomic structure. Košler and Sylvester, (2003) describe instrument mass discrimination as resulting from changes to the distribution of ions released from the machine due to various factors. Isotopic fractionation is a process which involves a chemical change to the isotope resulting in different isotopes. Since

radiometric dating are calculated through parent and daughter isotopes, changing the ratio of isotopes will lead to incorrect ages. Isotopic fractionation can be caused by numerous factors including gaussian beams, the presence of ambient gas, depth of pit, and the laser's wavelength, pulse duration, profile, energy density, repetition rate, and focus (Košler and Sylvester, 2003).

Issues and resolutions in LA-ICPMS

In LA-ICPMS, there are many different parameters that can strongly influence the precision and accuracy of the data (Košler and Sylvester, 2003). When the laser hits the sample, it may cause fractionation of the isotopes, which will yield incorrect ratios and thus incorrect ages (Košler and Sylvester, 2003). To combat this from happening, great care must be regarded when considering the laser's wavelength, pulse duration, profile, energy density, repetition rate, focus, and the presence of ambient gas. When the laser is introduced to the sample, it will create a pit and refractory elements like uranium are more likely to stay in the confines of the crater, which will have an impact on the U/Pb ratio, and thus the age (Košler and Sylvester, 2003). The duration of the laser's pulses is also a significant factor in the possibility of sample ablation/melting during analysis (Košler and Sylvester, 2003). These lasers will generally pulsate in 5 to 10 nanoseconds. When run for this duration, photons in the sample have time to dissipate resulting in significantly incorrect age ratios (Košler and Sylvester, 2003). Another significant factor of ablation is the surface area and distribution of power on the tip of the laser (Košler and Sylvester, 2003). A gaussian beam (rounded) will not only produce rounded holes that reduces sample yield, but it also may result in non-representative sampling because the center of the beam is hotter and thus certain elements may leave the system more quickly. A flat-topped beam creates a laser, which can produce a homogenous supply of energy across the surface area of the surface of the sample and is less likely to cause melting (Košler and Sylvester, 2003).

Utilizing LA-ICPMS for the Marshfield Terrane

In order to obtain a better understanding of the Marshfield Terrane both U-Pb and Lu-Hf must be characterized to define an age of the rocks and their source environment. Zircons are frequent carriers of hafnium at the weight percent level as well as large amounts of uranium, thorium and rare earth elements at the parts per million level (Kinny and Maas, 2003). A number of these elements undergo spontaneous decay and these ratios of decay are utilized to determine a suite information, including age.

Uranium-Lead geochronology system

Zircon, a tetragonal nesosilicate, is among the most fundamental minerals for geochronologic studies (Davis et al., 2003; Harley and Kelly, 2007). Zircon, $ZrSiO_4$, may undergo a simple substitution process where uranium (U) or thorium (Th) replaces zirconium in the zircon's crystal structure. ^{238}U, ^{235}U, and ^{232}Th are radiogenic and will undergo spontaneous decay down a complex decay chain to lead (Pb): ^{206}Pb, ^{207}Pb, and ^{208}Pb respectively. A fourth lead isotope, ^{204}Pb, is nonradiogenic. Zircon strongly discriminates against Pb during crystallization, thus most Pb found is likely from the radioactive decay of U or Th (Davis et al., 2003). The ratio of parent (uranium) and daughter (lead) isotopes may be used to determine a crystallization age for the zircon (Davis et al., 2003). ^{238}U and ^{235}U may be utilized simultaneously to allow for two age determinations – an agreement of ages reflects a closed system referred to as concordance (Davis et al., 2003).

Zircon resiliency and concordia

Zircon crystals are remarkably refractory due to low diffusion rates for several elements within the crystal structure and thus, tend to maintain the same compositions from crystallization

regardless of the host rock being metamorphosed, melted or weathered away (Scherer et al., 2007; Kinny and Maas, 2003). A zircon which remains a closed system attains secular equilibrium where the products of the parent and intermediate/final daughter are all equal; for every atom of U which is decayed, an atom of Pb is/will be created (Schoene, 2014). This is not to say lead loss is impossible, and methods are available to validate or invalidate ages (Schoene, 2014). The concordia curve (Wetherill, 1956) is a XY comparison of $^{207}Pb/^{235}U$ and $^{206}Pb/^{238}U$. A curved line, concordia, represents the ratio of U/Pb that should exist for a given age in a closed, secular equilibrized system (Davis et al., 2003; Harley and Kelly, 2007; Schoene, 2014; Wetherill, 1956). Ages that agree are concordant and if the ages of the two systems do not lie on the concordia curve, they are said to be discordant. If a geologic event occurs when the zircon reaches its closing temperature or is caused heated above that temperature following crystallization then the secular equilibrium is disturbed, and the zircon may lose intermediate/final daughters (Schoene, 2014). The zircon may also experience self-inflicted damage due to the radioactive decay of radiogenic elements that may cause several secondary internal textures that are observed through cathodoluminescence (CL) and backscattered electron (BSE) imaging (Geisler et al., 2007). Radioactive damage the zircon crystal structure has been found to cause the periodic loss of Pb; however, it has been found that periodic loss decreases with time due to crystal annealing – re-equilibration of the mineral (Geisler et al., 2007). Zircon may be re-equilibrated in the presence of a fluid or through a coupled dissolution-reprecipitation process (Geisler et al., 2007).

Geochronology Standards and Precision

The international LA-ICPMS U-Th-Pb community has recently redefined its standards for reporting and interpreting geochronologic data (Horstwood et al., 2016). Statistical

parameters such as mean square weighted deviation (MSWD) – also known as the reduced chi-squared statistic – are typically utilized to define how well the data fits the weighted mean (Horstwood et al., 2016). The closer the MSWD is to one is said to reflect an undisturbed data set. Weighted mean calculations may present a problem because they can only define data down to the level of data point uncertainty (Horstwood et al., 2016; Ludwig, 2012). Data uncertainties may be either random or systematic (Horstwood et al., 2016) but only random uncertainties may be reduced to low levels (Vermeesch, 2018). As such, age calculations are only as precise as their decay constants (Vermeesch, 2018). Due to these constraints, Horstwood et al. (2016) have proposed not put emphasis in the MSWD value and as such they were not a factor when considering which analyses would be kept or removed. Ages that were less than five percent discordant and within a singular tight age population were utilized to calculate crystallization ages.

Lutetium-Hafnium system

Crustal rocks are typically thought to be chemically complimentary to a depleted mantle reservoir (Kinny and Maas, 2003).The Lu-Hf isotopic system provides a record of this differentiation between a low Lu-Hf reservoir (depleted mantle) and a higher Lu-Hf reservoir (crustal rock), similar to the Sm-Nd isotopic system (Kinny and Maas, 2003). For this study, the Lu-Hf system is particularly valuable due to its preservation in zircon. ^{176}Lu undergoes radioactive decay to form the stable isotope ^{176}Hf that provides a time frame for a melt leaving the mantle (Kinny and Maas, 2003). If the age of the zircon is known, then this system may be used to infer the host rock's original plate tectonic setting (Kinny and Maas, 2003). The system utilizes a ratio of ^{176}Hf/^{177}Hf where ^{177}Hf is a stable, constant value which is assumed for the bulk silicate portions of the Earth. The value is determined from undifferentiated meteorites,

collectively called chondritic uniform reservoir (CHUR), where refractory elements such as hafnium have stayed in the silicate portions of Earth since its original differentiation in the early Earth system (Scherer et al., 2007). ^{176}Lu decays to ^{176}Hf with a half-life of 35 billion years, meaning that changes to the ^{176}Hf value may be considered a negligible rate thus the initial ^{176}Hf ratio is essentially preserved and serves as an indicator of source environment (Kinny and Maas, 2003).

The Lu-Hf system is utilized to trace the evolution and differentiation of the zircon regarding a mantle magma source because Lu-Hf fractionation occurs during the generation of the magma (Kinny and Maas, 2003). Zircon is a highly refractive mineral and its internal chemistry and structure are often retained even if the host rock is metamorphosed (Scherer et al., 2007) meaning that one may still learn about timing of the initial crystallization and the tectonic environment in which the zircon crystalized in (Kinny and Maas, 2003). Initial Hf values are recorded in epsilon notation which is expressed as parts per ten thousand (Kinny and Maas, 2003) to allow for the expression of change in whole numbers. An initial Hf composition of zero defines CHUR, a positive value represents a depleted source, and a negative value suggests an enriched source (Kinny and Maas, 2003). Mixing between sources with different evolutionary properties may also generate a εHf between DM and highly enriched values.

Results

Overview

The rocks of the Marshfield Terrane have been described by petrography, XRF, sodium peroxide fusion with ICP-MS and zircon geochronology & geochemistry. The following results

were obtained and their relation to the origin and evolution of the Marshfield Terrane is discussed in the discussion section.

Petrography

Figure presentation

All petrographic figures are broken into four sections where A and C will represent the thin section in plane polarized light (PPL) and cross polarized light (XPL). All figures are at the 10x objective with a 1000 μm scale, unless stated otherwise. Figures C & D will generally represent rotation of the stage under XPL, unless stated otherwise. All mineral percentages are estimates. Eight of the nine samples have confirmed variable amounts of dynamic recrystallization as defined by Stipp et al., (2002), and several samples feature alkali feldspar to sericite alteration due to weathering. Minerals are abbreviated in accordance with the naming conventions of Whitney and Evans, (2010): Act – Actinolite, Afs – Alkali feldspar, Ano – Anorthoclase, Bt – Biotite, Chl – Chlorite, Cum-Gru – solid solution series of cummingtonite and grunerite, Ep – Epidote, Hbl – Hornblende, Ms – Muscovite, Pl – Plagioclase, Ser – Sericite, Tr – Tremolite, Ttn – Titanite, Qz – Quartz. Many of the samples have undergone quartz dynamic recrystallization. We use the classification of the quartz deformation from Stipp et al. (2002) to estimate deformation temperatures.

16MT01

16MT01 (Fig. 6) is a porphyritic and hypidiomorphic hornblende biotite granodiorite which is dominantly characterized by clear minerals in plane polarized light. Grain size varies throughout, from tens to a few thousands of micrometers. Mineralogy includes: quartz (35%), plagioclase (20%) and alkali feldspar (18%), hornblende (15%), biotite (10%), epidote (1%),

titanite (1%), muscovite (< 1%) and zircon (< 1%). Quartz grains (hundreds – ~1500 μm) are clear with low relief in plane polarized light and feature low first order interference colors in cross polarized light. Subhedral to anhedral crystal structures are common with the grains featuring irregular sutured boundaries. They have undergone grain boundary migration dynamic quartz recrystallization which suggests temperatures greater than 500° C upon deformation (Stipp et al., 2002). Undulatory extinction is weak and found throughout the grains. The feldspars (hundreds – 1500; a few megacrysts at ~4000 μm) are colorless with low relief in plane polarized light. Subhedral grains with polysynthetic (plagioclase) or carlsbad (alkali) twinning is common with oscillatory zoning rarely present. Coarse grained feldspars display weak undulatory extinction. Rarely, portions of plagioclase grains have altered to sericite. Sericite is seen as anhedral, fibrous blobs with bird's eye extinction. The minerals reside as symplectites in feldspar structures. Hornblende (hundreds μm) is strongly pleochroic, from light tannish green to dark green, and displays typical amphibole cleavage. Grains are typically euhedral when their C axis is perpendicular to the thin section, and subhedral when parallel. Biotite (hundreds μm) grains are pleochroic light tannish brown to dark brown in plane polarized light with basal cleavage easily recognizable. A small percentage of grains have inclusions of zircon with pleochroic halos. Very rarely clear micas are seen. These grains, muscovite (hundreds μm), display high birefringence; up to third order pinks. A few crystals of subhedral-anhedral epidote (hundreds μm) are found with pale green pleochroism and with high relief in plane polarized light. In cross polarized light, second to third order blues, purples and greens are present. Titanite (hundreds μm) is occasionally found as clearish-brown, coarse euhedral crystals that have become fragmented sometime after crystallization. They have prominent relief in plane polarized light with a thick, dark stain, which follows the immediate outline of the crystal. Zircon (tens-

hundreds μm) are rarely present as small euhedral crystals with high relief and occasionally high interference colors. Some zircon grains are rarely included into biotite, and pleochroic halos are visible.

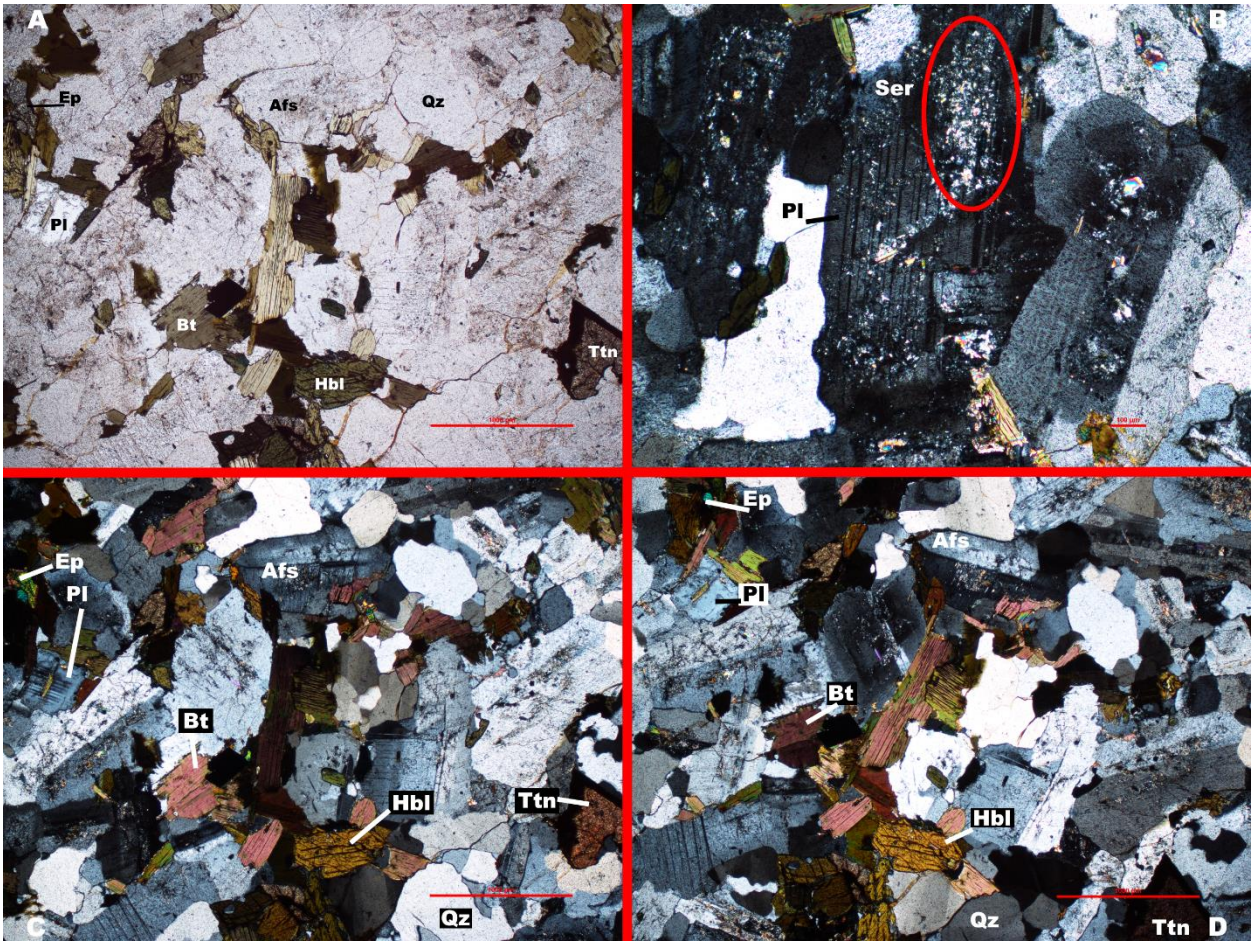

Figure 6: 16MT01 – A+C displays the same image under different lighting. C and D display the rotation of the same view under XPL. A) Plane polarized light (PPL). Grains are not notably weathered in PPL, but unusual black bands around titanite are apparent. B) Under cross polarized light (XPL), weathering is apparent with plagioclase and alkali feldspars developing inclusions of sericite. C) & D) Polysynthetic and carlsbad twinning are apparent for feldspar identification. Quartz grains feature moderate amounts of undulatory extinction, suggesting some amount of tectonic structural perturbation.

16MT02

16MT02 (Fig. 7) is a pegmatitic and porphyritic K-feldspar intrusion that cross-cut 16MT03 in the field. In thin section, the sample is impoverished of any colored minerals in plane

polarized light, except for a few small opaque minerals. Mineralogy includes anorthoclase (65%) quartz (32%), plagioclase (3%), and zircon (< 1%). It is strongly porphyritic with some of the largest minerals stretching far beyond the view finder at the lowest power setting. K-feldspar (thousands – 10,000s μm) grains are anorthoclase, strongly pegmatitic and display strong undulatory extinction. The grains are subhedral to anhedral with intergrowths and granophyric textures occasionally present. The anorthoclase grains are clear to very light tannish brown in plane light and have first order greys and whites in cross polarized light. One set of cleavage planes is always visible, and the second set is occasionally present; they meet at approximately 92 degrees. Some grains have fractured, and deposits of micro-veined quartz have been emplaced. Rarely, quartz may be included into a single K-feldspar grain. Quartz grains are very inequigranular (tens – hundreds μm) and are most frequently present as subhedral to anhedral crystals in micro-veins both between, and inside of, fractured alkali feldspars. A few larger, more euhedral grains are rarely present outside of the veins. Quartz grains appear stretched and strained and have undergone either subgrain rotation recrystallization or grain boundary migration recrystallization. This indicates temperatures of at least 400° C during some deformational event (Stipp et al., 2002). In cross polarized light, first order greys to pale yellows are common with a variable amount of undulatory extinction across the grains. A couple of plagioclase grains with polysynthetic twinning are rarely found in quartz veins. Zircon (tens-hundreds μm) are very rarely present as small euhedral crystals with high relief and occasionally high interference colors. A couple of grains rarely appear to have no interference colors due to them either not being polished down or them residing under other minerals; alternatively, they may be apatite.

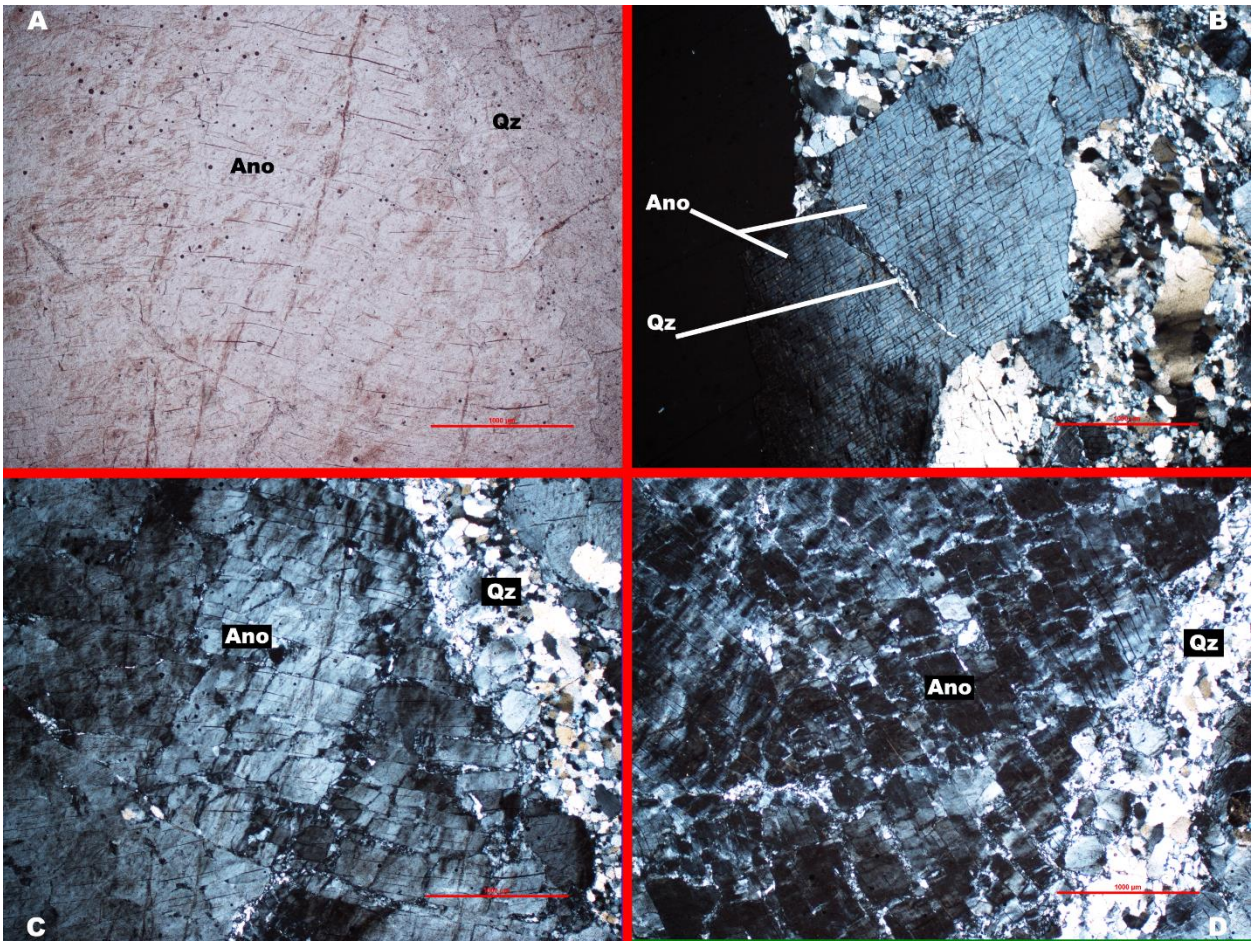

Figure 7: 16MT02 – A+C displays the same image under different lighting. C and D display the rotation of the same view under XPL. A) Under PPL, grain boundaries are not clear. B) Under XPL anorthoclase grains exhibit two cleavages not at ninety degrees. C) & D) With rotation of the stage under XPL, a sweeping undulatory extinction is prominent.

16MT03

16MT03 (Fig. 8) is a biotite quartzofeldspathic gneiss with mylonitic textures. Mineralogy includes: quartz (60%), anorthoclase (25%), biotite (15%), and zircon (< 1%). There are prominent bands of porphryoblastic quartz and cryptocrystalline dark mineral bands (likely biotite). Biotite is also present rarely as larger "destroyed" grains. Quartz (tens – ~1000 μm) is the abundant through the thin section and occurs as large anhedral grains separate of banding, as

somewhat large anhedral grains which are clustered together to form the coarse bands or as small, anhedral grains which form the fine-grained bands. Quartz has undergone grain boundary migration recrystallization which suggests temperatures greater than 500° C upon deformation (Stipp et al., 2002). Only a portion of the grains appear to be rounded by sedimentary processes. K-feldspar (tens – ~ 1000 μm) is less abundant in 16MT03 compared to 16MT02, but several grains may still be found. They are of anorthoclase origination with one set of cleavage planes is always visible, and the second set is occasionally present; they meet at approximately 92 degrees. Some feldspar grains display domino-type fragmented porphyroclastic textures which is very common in mylonitic rocks. As before, most of the grains have strong undulatory extinction textures. Typical anorthoclase twinning is present, but a small sample of the grain's boarder on more microcline-like twinning and have cleavage planes at ~90 degrees. Rarely, portions of feldspar grains have diminished to sericite. Sericite is seen as anhedral, fibrous blobs with bird's eye extinction; The minerals reside as symplectites in feldspar structure. Biotite bands are visible as mostly cryptocrystalline bands with rarely very fine crystals. Some of these bands appear to have been on the path to chlortiziation, some displaying a clear to very light green pleochroism. Elsewhere, the grains are clear, destroyed with symplectite-like alteration and may have partially altered to clays. Zircon (tens-hundreds μm) are very rarely present as small euhedral crystals with high relief and high interference colors.

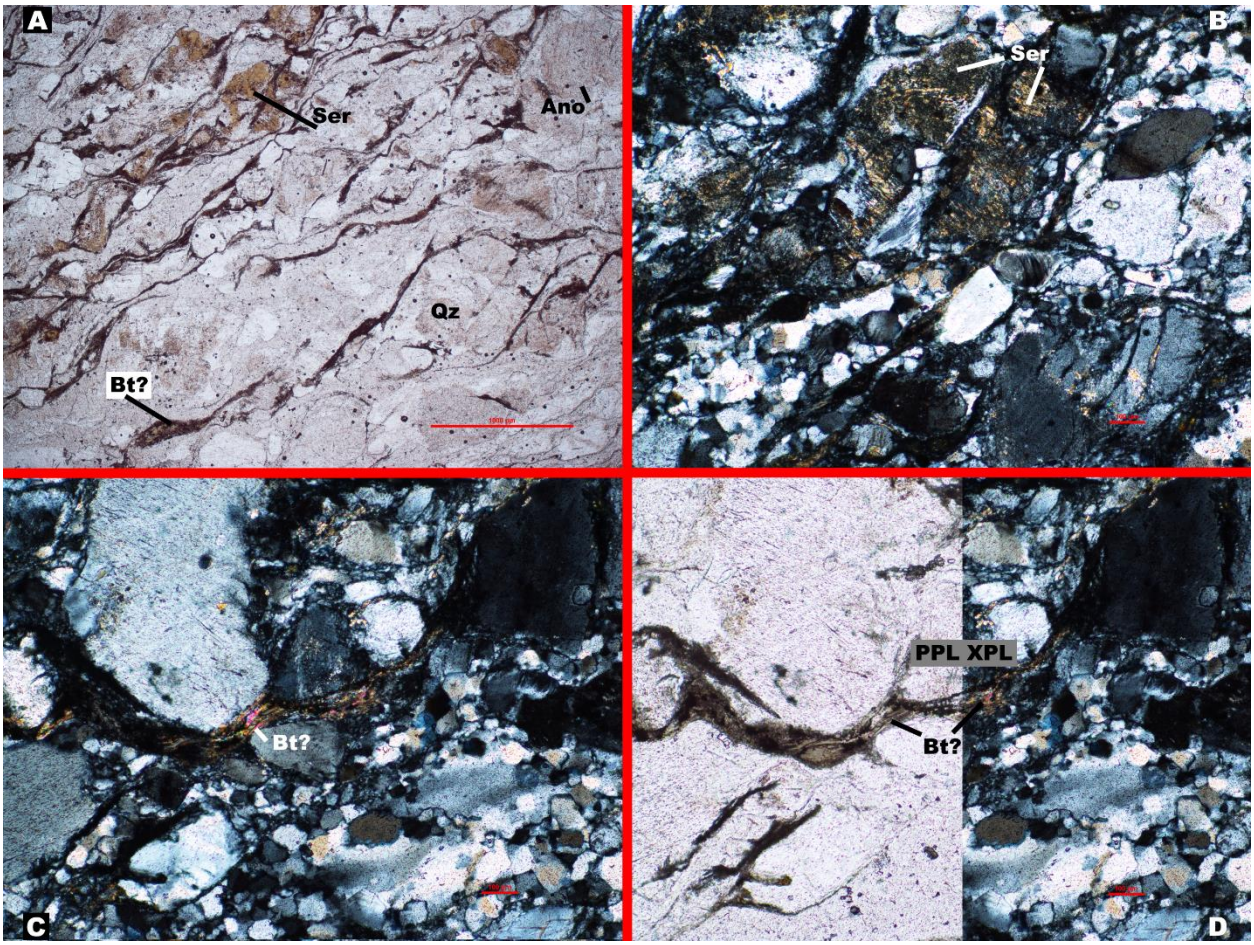

Figure 8: 16MT03 – A) PPL. Sericite completely replaces a feldspar structure. B) XPL. Sericite displays anomalous, rainbow like interference colors. C) XPL & D) PPL & XPL. Cryptocrystalline bands of mica, likely biotite, are visible.

16MT04

16MT04 (Fig. 9) is a fine-grained, amphibole biotite quartzofeldspathic schist. Mineralogy includes quartz (40%), amphibole (40%), biotite (15%), epidote (3%), plagioclase feldspar (2%) and zircon (< 1%). Grains are fine with a mean grain size estimated to be on the order of a couple hundred micrometers. Banding is moderately present throughout the sample at a microscopic scale; however, it appears to be occasionally fractured against the foliation with deposits of minerals filling in the void. A prominent vein with a partially unique mineralogy

crosscuts the foliation across the entire thin section. In one area of the vein is a quartz crystal that follows the fracture in both directions and the foliation in one direction suggesting synchronous formation of the foliation and fracture, although other grains don't feature this morphology. The quartz bands are often crosscut by veins of mafic composition, suggesting nonsynchronous formation. Several other fractures run through the thin section, but none of these appear to have missing material or replaced material. Quartz (tens to a few hundred μm; a large coarser grained band stretching across most of the thin section, with crystals ~ 3000 μm) grains are well banded, fairly subhedral to anhedral and feature undulatory extinction. Their boundaries are somewhat irregular and indicative of bulging recrystallization, suggesting deformation temperatures of at least 300° C after crystallization (Stipp et al., 2002). Two or three bands of quartz are significantly coarser grained with grains as large as 3000 micrometers. Amphibole (tens to a few hundred μm) grains feature green to dark green pleochroism with typical amphibole cleavage in plane polarized light. In cross polarized light, first order yellow and oranges are common (hornblende), but they may also feature high first order reds and pinks (tremolite?) with occasional low second order blues (actinolite). A few amphibole grains are clustered around an iron oxide and feature mid to high second order blues, greens and pinks. Amphiboles rarely show both cleavage plains as many of the grains are (010) sections (Nesse, 2013). Biotite (tens to a few hundred μm) grains appear as brown to light green grains and typically feature an irregular brown line running through them. It is possible these brown bands are cryptocrystalline biotite which have become highly strained and smeared. Some of these bands appear to have been chloritizatized with slight light green pleochroism visible. The finest biotite grains feature high interference colors whereas the coarser grains have their birefringence are masked by the mineral's color. Epidote (~100 μm) grains are rarely seen as subhedral fragmented crystals with

pale green to light green pleochroism and high relief. They feature third order pink and green interference colors. Feldspar (tens to a few hundred μm) grains are rarely seen with polysynthetic twinning and are likely of a plagioclase composition. Zircon (tens-hundreds μm) are very rarely present as small euhedral crystals with high relief and high interference colors.

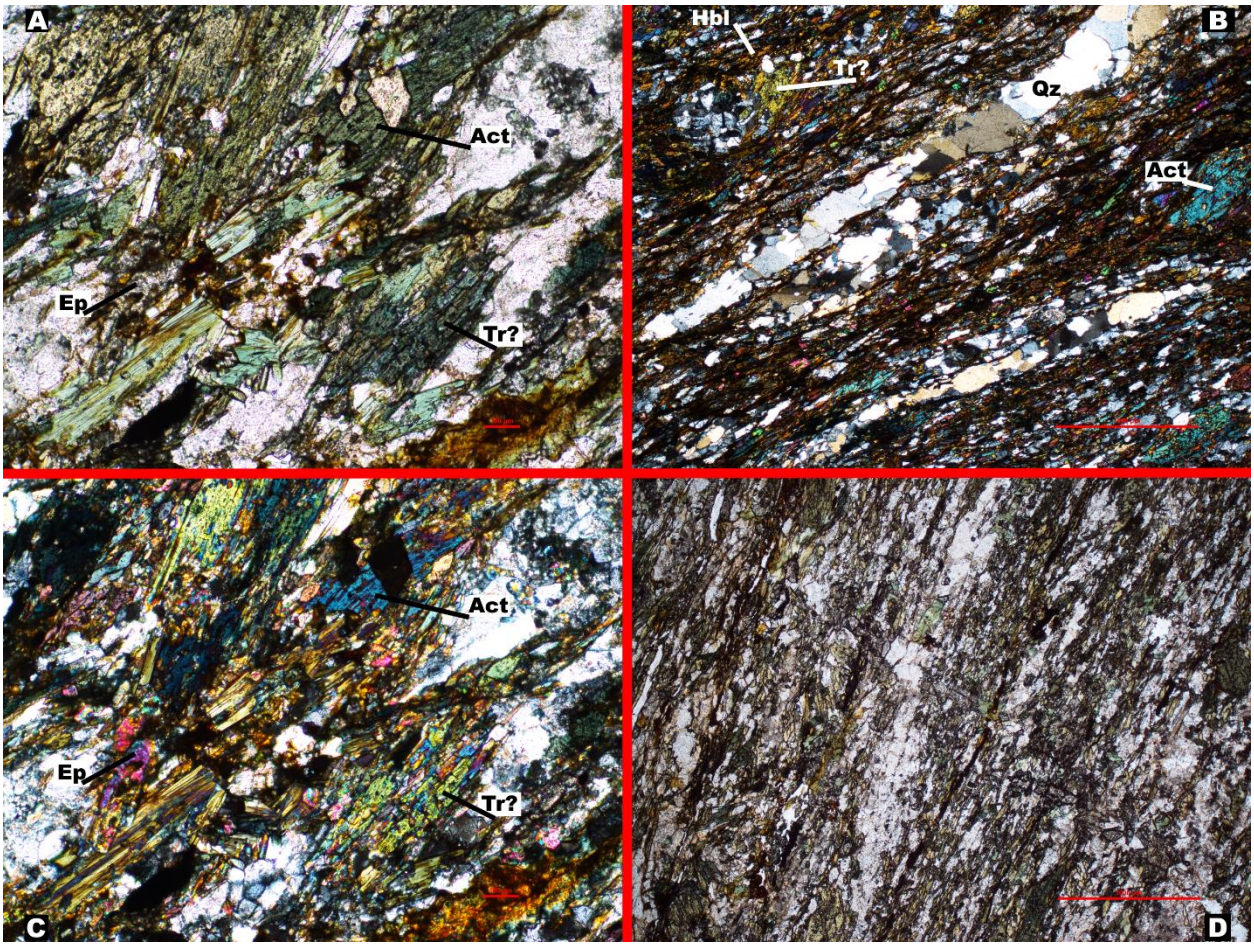

Figure 9: 16MT04 – A+C displays the same image under different lighting. A) PPL. Amphiboles intermixed with biotite clearly stand out. C) When switching to XPL, actinolite and tremolite are easy to distinguish based on birefringence. B) XPL. Amphiboles distinguished by birefringence. A coarser grained band of quartz runs with the foliation. D) PPL. The foliations are clearly visible and are running roughly north-south in the current orientation.

16MT05

16MT05 (Fig 10) is an amphibole quartzofeldspathic gneiss with two distinct zones that repeat in bands: 1) a felsic rich zone dominated by quartz (60%) with lesser amounts of plagioclase and rarely alkali feldspar (10%), 2) bands rich in amphibole (15%), chlorite (10%), biotite (5%) and epidote (3%) which are subhedral to anhedral and feature sutured boundaries, especially towards the termination of the crystal on their C and A axes respectively. Quartz (tens – ~1000 μm) grains appear to have undergone grain boundary migration recrystallization as defined by Stipp et al. (2002), suggesting deformation temperatures of at least 500° C. The subhedral to anhedral grains have irregular, sutured boundaries and are generally on the order of a few hundred micrometers. Euhedral quartz grains are generally coarser and range from a few hundred to ~2000 micrometers. The quartz grains are clear with low relief in plane polarized light with first order greys and yellows in cross polarized light. Undulatory extinction is weak, but present through the quartz grains. Plagioclase and alkali feldspars (tens – several hundred μm) are less common but present in the quartz rich bands. Plagioclase grains have low first order greys with polysynthetic twinning under cross polarized light. A presence of a few alkali feldspar grains with cleavages not at ninety degrees are rarely visible. Most of the alkali feldspars have carlsbad twinning, but a couple of coarser grains do not show this. Feldspar grains are subhedral to anhedral with irregular sutured boundaries with grain features twins are curved – possibly due to strain of post-depositional tectonic activity. A couple of epidote crystals are present at the felsic-mafic boundary. Epidote crystals in this area are euhedral-subhedral with pale green to light green pleochroism with high relief with second to third order blues, purples and greens. The mafic bands are less organized and anhedral quartz is present throughout the bands as well as hornblende, biotite, and epidote. Hornblende (hundreds – ~1000 μm) rarely shows both cleavage plains as many of the grains are (010) sections (Nesse, 2013). Hornblende has brown to dark

greenish brown pleochroism with moderate relief in plane polarized light; interference colors are often masked the minerals color in cross polarized light. Where present, first order yellow and oranges are common, but some grains display low second order blues and likely have an actinolite component. Biotite (tens – ~1000 μm) grains are light brown in plane polarized light and feature a weakly present birds eye extinction in cross polarized light. The finer biotite grains feature fourth order pink and green interference colors whereas the coarser grain's birefringence is masked by the mineral's color. Chloritization has taken place on several biotite grains. Epidote (hundreds μm) is present but is notably more euhedral compared to those found at the quartz-mafic boundary. They have high relief and pink third order or blue and purple second order interference colors. Zircon analyses were conducted on 16MT05, however zircon in thin section was not immediately apparent.

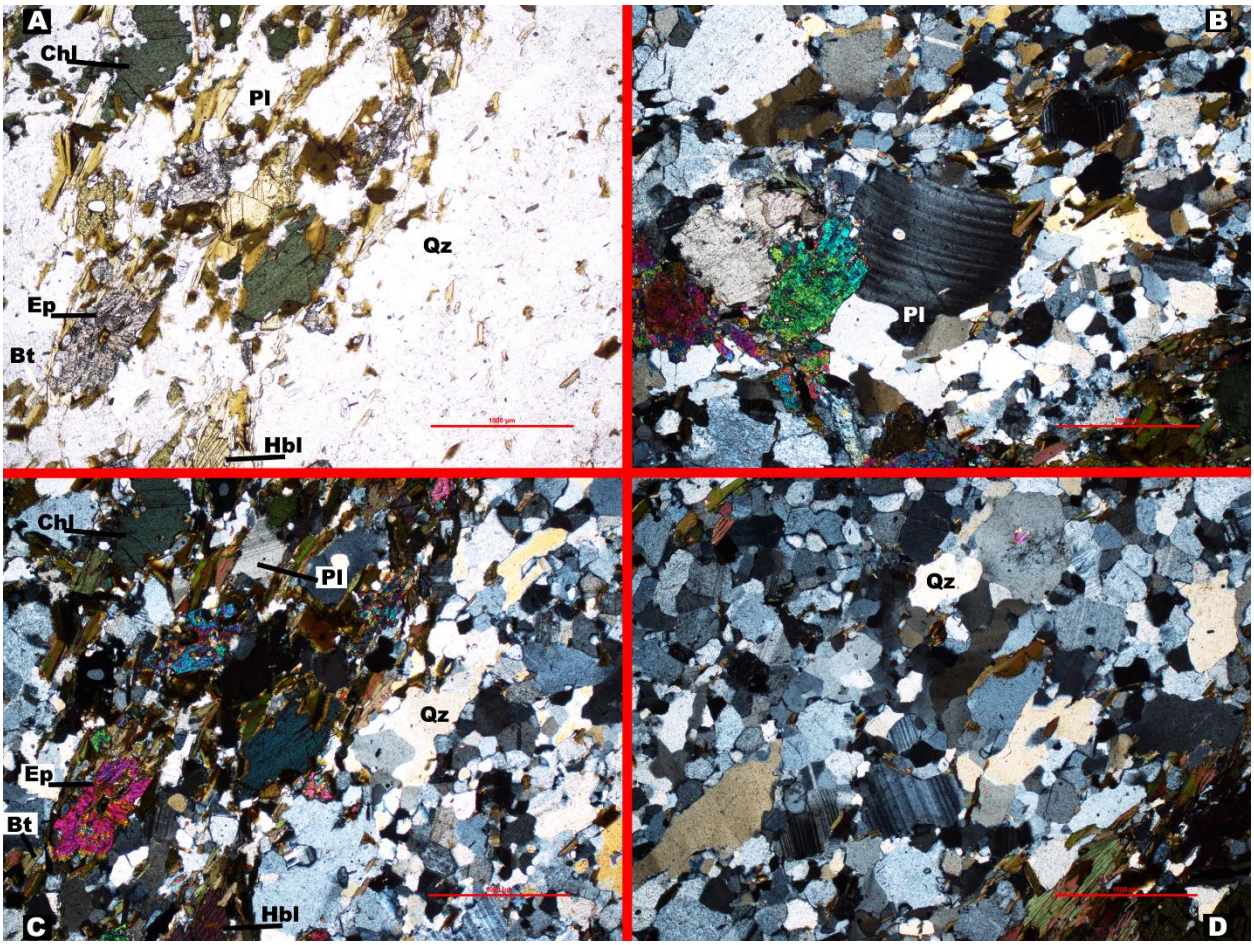

Figure 10: 16MT05 – A+C displays the same image under different lighting. A) PPL. Chlorite grains stand out and do not display a visible cleavage. C) When switching to XPL, epidote displays distinct, bright birefringence colors. B) XPL. A plagioclase with bent polysynthetic twins, likely due to strain. D) Grain boundary migration is clear on several quartz grains with irregular, sutured boundaries common.

16MT06

16MT06 (Fig. 11) is an amphibole quartzofeldspathic schist. Minerals are weakly organized in foliations and typically on the order of tens of micrometers except for a couple of short quartz bands which may be have crystals a few hundred micrometers across. Mineralogy includes several amphiboles (65%) (hornblende, tremolite, actinolite and the possibly solid solution series of cummingtonite-grunerite), quartz (30%), alkali feldspar (5%), and plagioclase

(5%). Actinolite is the most common amphibole and is pale green, fibrous and weakly pleochroic (light green to slightly darker light green) in plane polarized light with high positive relief. The grains are needle-like with low second order royal blue interference colors. Tremolite is also found as pale green, but its pleochroism is more pronounced and changes to deeper shades of green than actinolite and has higher interference colors, second order yellows and oranges. Hornblende is also seen as pale green in plane polarized light. It is pleochroic with a light green to lime green transition. Birefringence is most commonly displayed in deep first order oranges. Other amphiboles display an array of interference colors with single crystals displaying a range of upper second order to mid third order colors. These amphiboles feature slightly inclined extinction and indistinguishable from other amphiboles in plane polarized light. The inclined extinction and range of interference colors is suggestive of a solid solution between cummingtonite and grunerite. Quartz (tens – ~ 400 μm) is generally coarser than the amphiboles with subhedral to anhedral crystals that feature undulatory extinction moderately present throughout. There are a couple of bands of quartz which are significantly coarser (~1000 μm). They have undergone grain boundary migration dynamic quartz recrystallization which suggests temperatures greater than 500° C upon deformation (Stipp et al., 2002). Feldspars (tens – ~400s μm) are rarely present with polysynthetic (plagioclase) or carlsbad (alkali). A megacryst (~several hundred μm) of plagioclase may be found among the coarse quartz bands.

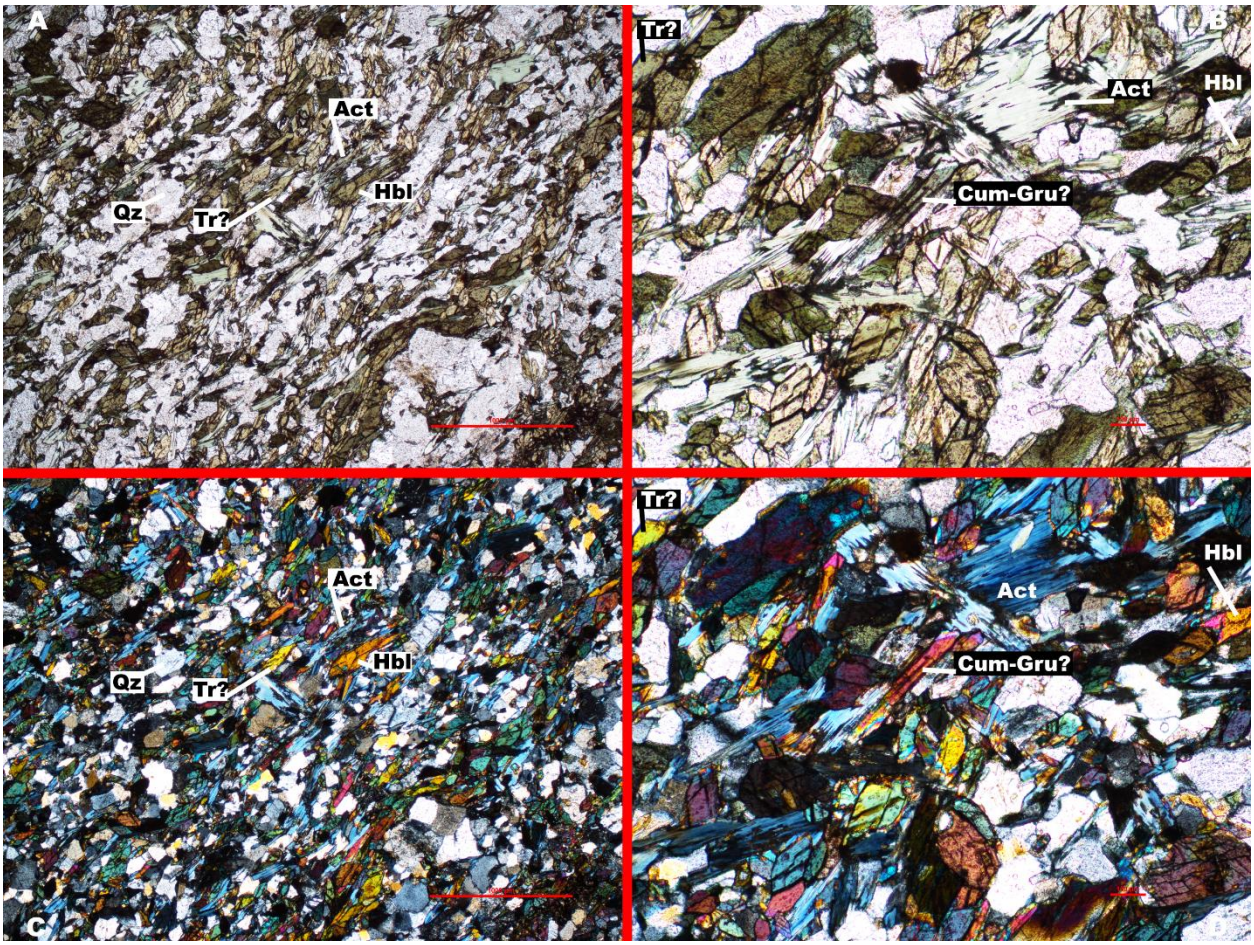

Figure 11: 16MT06 – A+C and B+D display the same images under different lighting. A) Amphiboles are difficult to distinguish from each other in PPL. C) When switching to XPL, several amphiboles are found. Tremolite displays bright yellow birefringence, whereas hornblende is a deeper first order orange. B) & D) display a closer view on the amphiboles under PPL and XPL respectively. Actinolite is royal blue in XPL and somewhat fibrous. Cummingtonite – grunerite (?) feature a range on interference colors and slightly included extinction.

16MT07

16MT07 (Fig. 12) is a biotite granite. Mineralogy includes quartz (50%), alkali feldspar (20%), plagioclase feldspar (17%), biotite (7%), hornblende (6%) muscovite (<1%), and zircon (<1 %). Quartz (tens – a few thousand μm) grains are clear with low relief and generally subhedral-anhedral, however, a few euhedral grains may be found. For this thin section, there is

a general trend with quartz coarseness – the coarser the quartz crystals are, the more euhedral they become. The subhedral to anhedral grains have irregular, sutured boundaries and are generally on the order of a few hundred micrometers. Subhedral to anhedral quartz grains are generally coarser and range from a few hundred to about 1000 micrometer except for a quartz megacryst which is about 4500 micrometers in length. Undulatory extinction and bulging recrystallization suggest deformation at c. 300° C (Stipp et al., 2002). Undulatory extinction typically becomes stronger with increased crystal size. Quartz more prominently features first order pale yellow birefringence rather than greys compared to other samples. Plagioclase and K-feldspar (tens – ~500 μm) are common and are defined by their respective twinning patterns. Where present, towards the edges of the thin section, anorthoclase cleavage and twinning are visible, and it displays a felty texture. Along some cleavage boundaries and fractures are very small microlites (only a couple of μm) euhedral-subhedral and occasionally anhedral crystals with low relief and high interference colors are present. Zircon and apatite are ruled out based on relief and interference colors. Outside of fractures/cleavage planes, other K-feldspar grains have numerous inclusions of this mineral. Sericite is easier to identify elsewhere in the thin section where it is not within grains, and more developed. Zircon (tens-hundreds μm) crystals are also rarely included into feldspar grains although easy to miss under low powered objectives. They are as small as sericite, (tens - < 10 μm) but with notably high relief, euhedral morphologies and high birefringence. Zircon is much more prevalent in 16MT07 than the other samples. Micas are typically found as subhedral biotite which has brownish green to dark brown pleochroism. Hornblende (~100 μm) crystals are rarely seen and appear to have had their crystallization disturbed. Where found, they terminate quickly, and biotite intergrowths are found. It is plausible hornblende became unstable and began to crystallize as biotite. When alone, biotite (~100 μm)

grains feature fourth order pink and green interference colors when they are very fine, coarser grains are masked by the mineral's color. Muscovite is rarely present as a somewhat fibrous anhedral blob which is clear in plane polarized light.

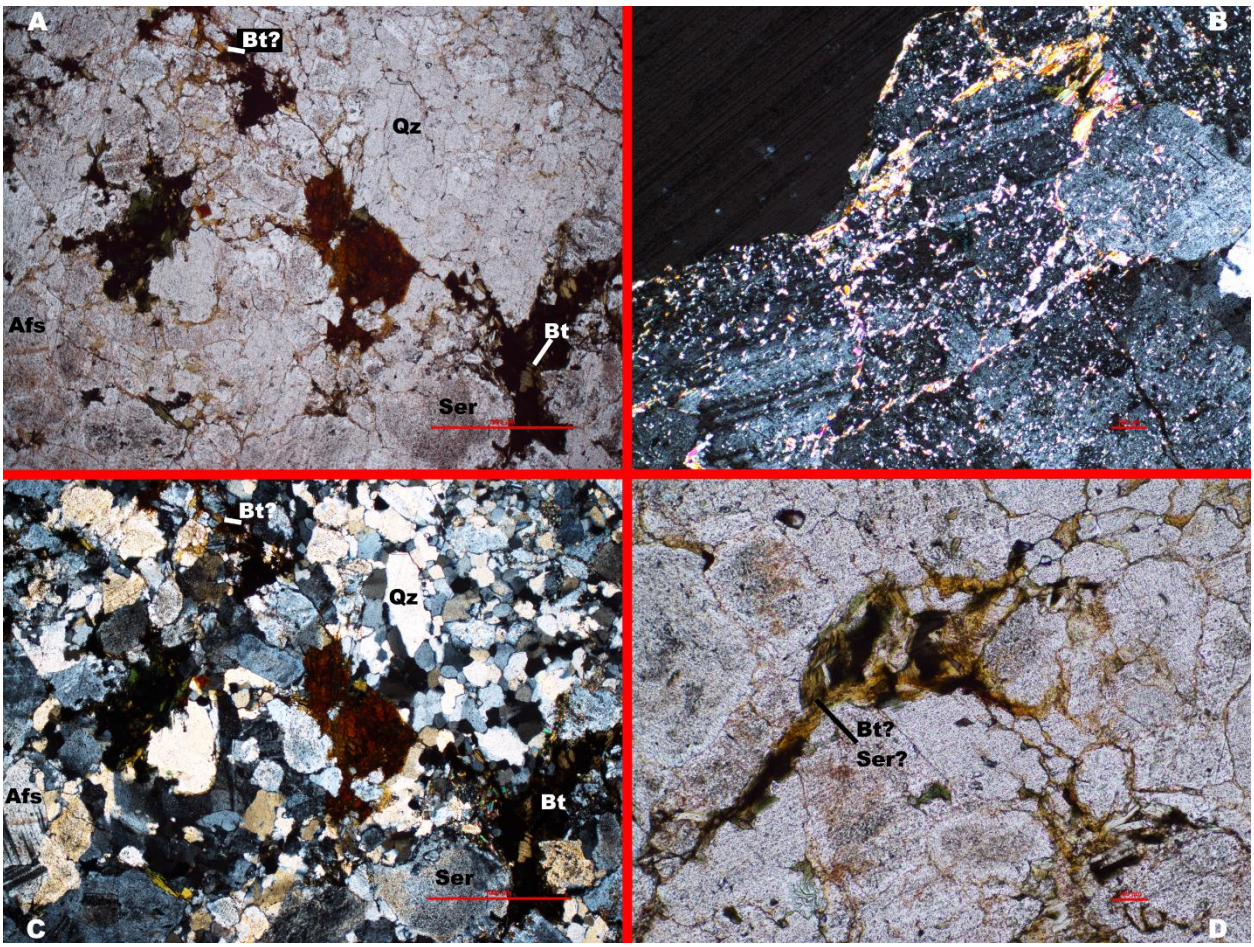

Figure 12: 16MT07 – A+C displays the same image under different lighting. A) PPL. Quartz if the most common mineral in the thin section. C) Dynamic quartz recrystallization is more apparent as grains in PPL break into several domains under XPL. B) Sericite development in feldspars. D) Biotite or sericite development under PPL.

16MT08

16MT08 (Fig. 13) is a metamorphosed equigranular aphanitic greenstone with no visible foliations. Mean grain size in the tens of μm and coarsest grains are no larger than a few hundred μm. Mineralogically the sample has been chloritized (50%). Chlorite is seen are light green

pleochroic mineral grains in plane polarized light. Micas are rarely visible as biotite (3%) and even lesser so as muscovite (1%). The matrix (~ 36%) is cryptocrystalline and may be some combination of quartz and calcic plagioclase. A large, fragmented amphibole is visible; much of the mineral has fragmented away and has been altered. The remaining percentage (10%) is composed of opaque minerals. Due to the nature of the matrix, dynamic quartz recrystallization could not be identified nor ruled out.

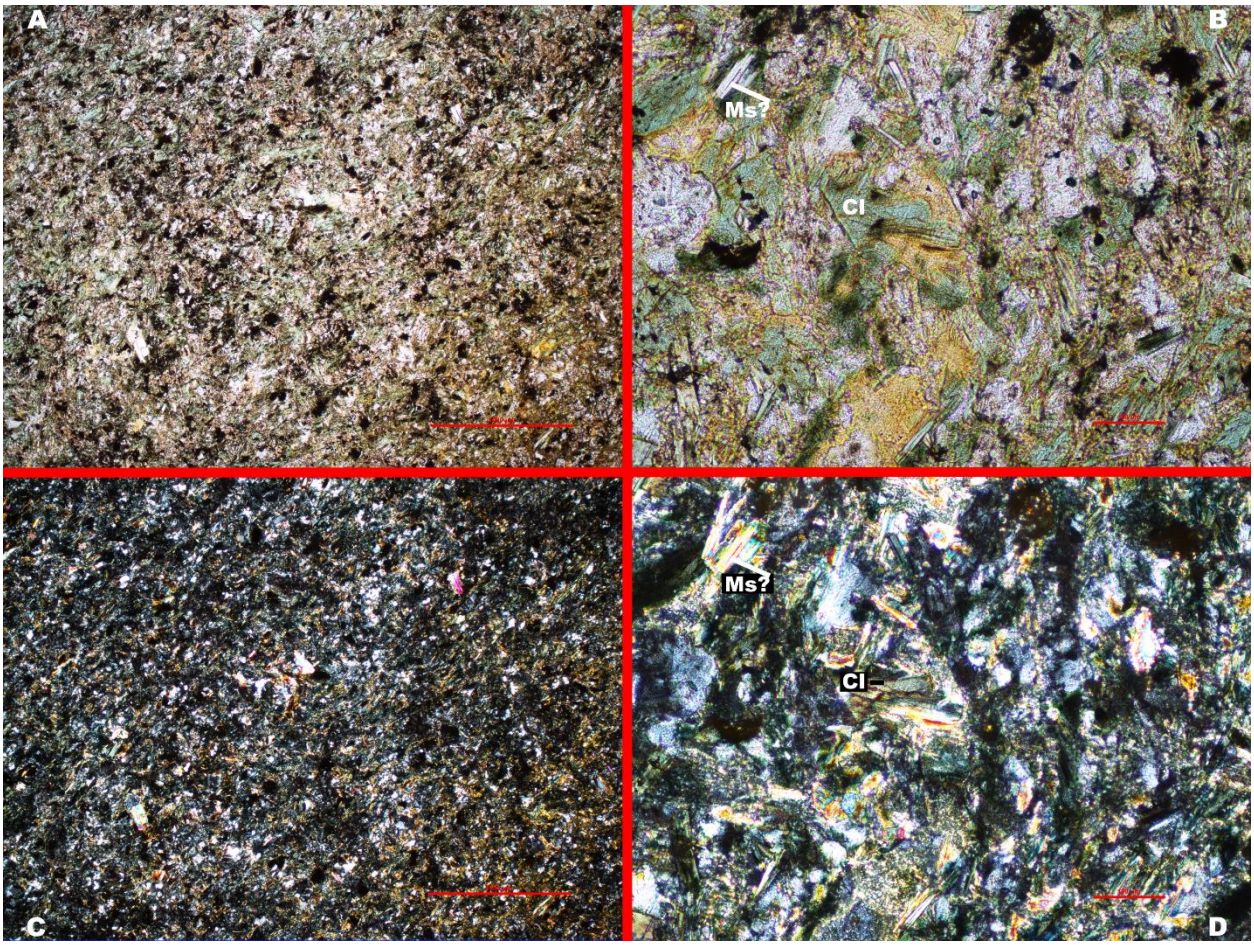

Figure 13: 16MT08 – A+C and B+D display the same images under cross polarized light. A) PPL. Fine chlorite grains float in a felsic matrix. C) Under XPL, the chlorite grains display anomalous interference colors. B) PPL. Under x20 magnification, chlorite is easier to distinguish. D) Under XPL, muscovite's high birefringence is apparent.

16MT09

16MT09 (Fig. 14) is an altered, heavily fragmented granofels which features two distinct zones which may be seen by simply hold the thin section up to light: 1) A heavily iron oxide stained zone with pronounced orange staining, and 2) an unstained zone. Mineralogically, the two zones are similar, however the stained zone has several dark brown iron oxide deposits that appear amorphous and non-crystalline. In zone two, these same phenomena are present, but are represented as opaque blobs rather than iron oxide stained. Alkali feldspar is notably lacking. Sericite (40%) is seen as anhedral, fibrous blobs residing as symplectites in former feldspar structures. The sample also contains quartz (50%), muscovite (7%), k-feldspar (3%), and zircon (< 1%). Quartz (tens -500 μm) is subhedral to anhedral with weak undulatory extinction. Their boundaries are somewhat irregular and indicative of bulging recrystallization, suggesting deformational temperatures of at least 300° C after crystallization (Stipp et al., 2002). Alkali feldspar (tens -500 μm) is rarely present as many of the crystals have altered to sericite. Where present, carlsbad twinning is occasionally present, and sericite inclusions are common. Muscovite is rarely present as clear grains in plane polarized light. When reacting with cross polarized light, high birefringence pinks, yellows and greens are displayed. Zircon (tens-hundreds μm) is rarely seen, but has high relief, euhedral morphologies and high birefringence.

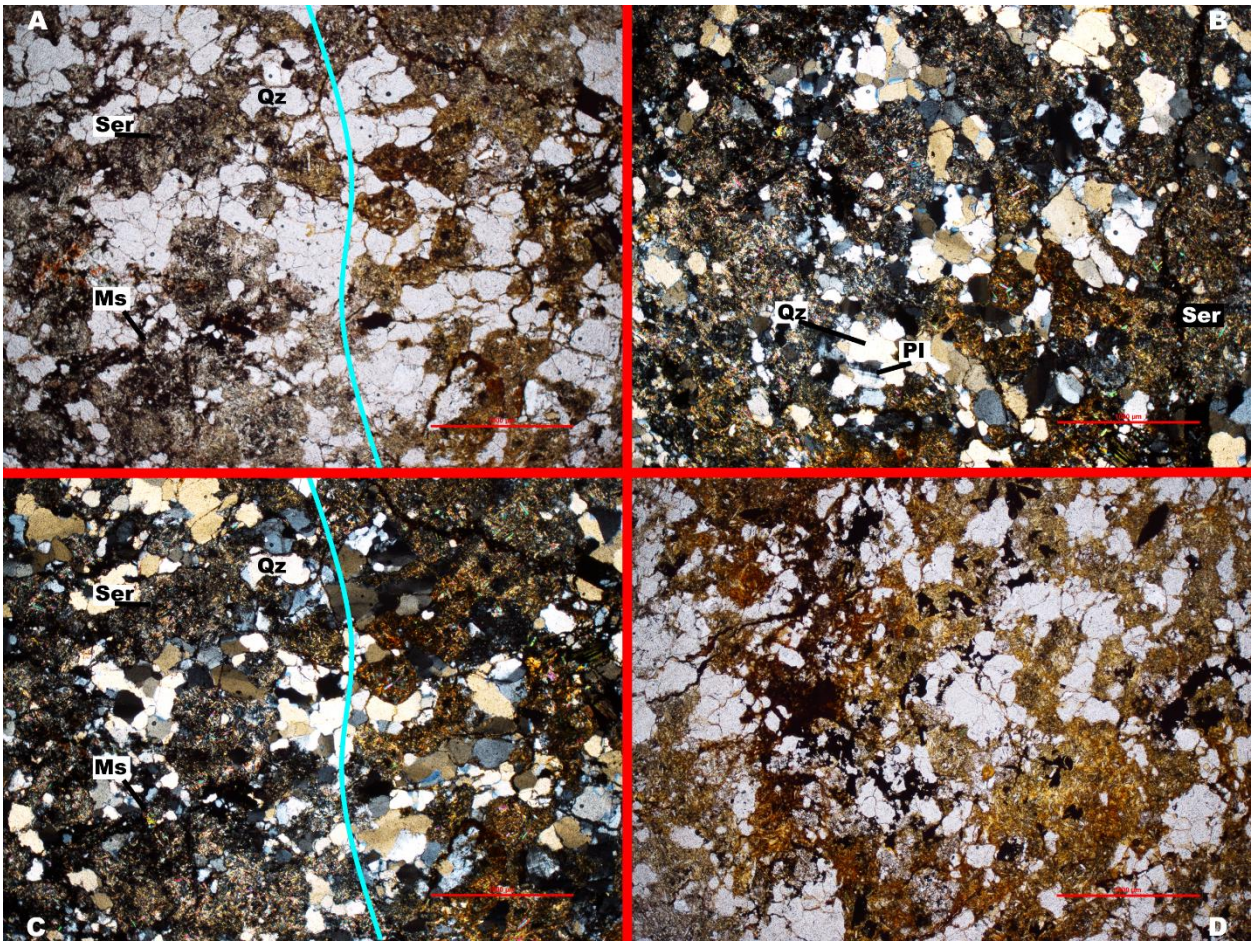

Figure 14: 16MT09 – A+C displays the same image under cross polarized light. A) PPL. The blue line separates the stained zone from the non-stained zone. C) Under XPL, dynamic quartz crystallization is apparent. B) Sericite development is prominent throughout, with anomalous interference colors and birds eye extinction. D) Iron oxide staining is prevalent throughout the sample.

Whole Rock Geochemistry

Preliminary whole-rock geochemical results on samples collected from the western Marshfield Terrane illustrate the role of subduction in the terrane origin and tectonic evolution. All felsic samples yielded a geochemical signature typical of a volcanic arc or syn-collisional system when plotted on tectonic discrimination diagrams. Likewise, the intermediate-mafic samples of the Marshfield Terrane were found to come from a continental arc system.

Winchester & Floyd (1977) produced several graphs useful for describing the protolith of altered rocks using immobile elements. Figures 15 – 17 illustrate possible geochemical origins for our samples and are summarized in table 1. Data for these figures were produced by XRF (Fig. 15 and 16) and ICPMS (Fig. 17). For XRF analyses, two pellets were produced per sample, and ICPMS data have only one analysis per sample. Our ICPMS data is of much higher precision than XRF and as such, ICPMS data is favored – especially when data do not agree.

Geochemical classification of protolith using immobile elements

Immobile elements

As seen by the petrography, these rocks have been altered by metamorphic and weathering processes. As such, we focus on attempting to characterize protolith using immobile elements. While figures 15 – 17 may display some conflicting results, this may be due to their history even though relatively immobile elements are in play. For unmetamorphosed samples, these geochemically support the petrography. For metamorphosed samples, these suggest a protolith.

Felsic samples – 01, 02, 03, 07, 09

XRF and ICPMS data for 16MT01 indicate that the sample is consistent with a rhyodacite – the extrusive equivalent of a granodiorite. This is consistent with hand sample and thin section identification of 16MT01 being a granodiorite. 16MT02 is notably deformed in thin section, but still recognizable in hand sample. Geochemically, it was not defined due to high ratios or because levels of Zr, and Y were below XRF and ICPMS detections limit. 16MT03 has the highest silica weight percentage among all samples, and generally charts off the Y axis values for the graphs below. It would plot as a high silica rhyolite, but after zircon

geochronology and analysis of petrographic textures, suggests that this is a rock with a sedimentary origin. As such, no igneous protolith is assigned. 16MT07 plotted in the rhyolite fields in all cases, matching our petrographic analyses of a granite which has later become deformed. The plot of Co versus Th concentration suggests the sample is highly potassic and shoshonitic (Fig. 19). Shoshonites are subduction related, alkali-rich trachyandesites that may occur with calc-alkaline volcanism or continental arcs (Murphy, 2007). 16MT09 plots in the high silica rhyodacite-dacite fields for all XRF data, and all data points are proximal to the rhyolite fields. A plot of Co versus Th concentration suggests the sample is highly potassic and shoshonitic.

Mafic samples – 04, 05, 06, 08

The protolith for 16MT04 is proposed to be a sub-alkaline basalt with calc-alkaline affinities (Fig. 16-19). 16MT05 is geochemically complex as XRF graphs varied. In Nb/Y vs. SiO_2 wt % space, 16MT05 A plotted as in the Comendite Pantellerite field, but 16MT05 B could not be plotted as the ratio of Nb and Y was too high. On the second graph, 16MT05 A and B plotted in the rhyodacite field; however, ICPMS data indicate an alkaline basalt and thus is considered the proposed protolith. Figure 19 suggests the sample is highly potassic and shoshonitic. 16MT06 is depicted a sub-alkaline basalt with calc-alkaline affinities. ICPMS data indicate an andesite protolith – the most likely protolith based on the quartz percentage. 16MT08 is characterized as an andesite with calc-alkaline affinities, which is notably proximal to more mafic compositions on both XRF plots. Initial hand sample specimens and petrographic analyses suggested a metabasalt. Since the matrix is cryptocrystalline, it is possible there the protolith was more of a mafic andesite rather than basaltic.

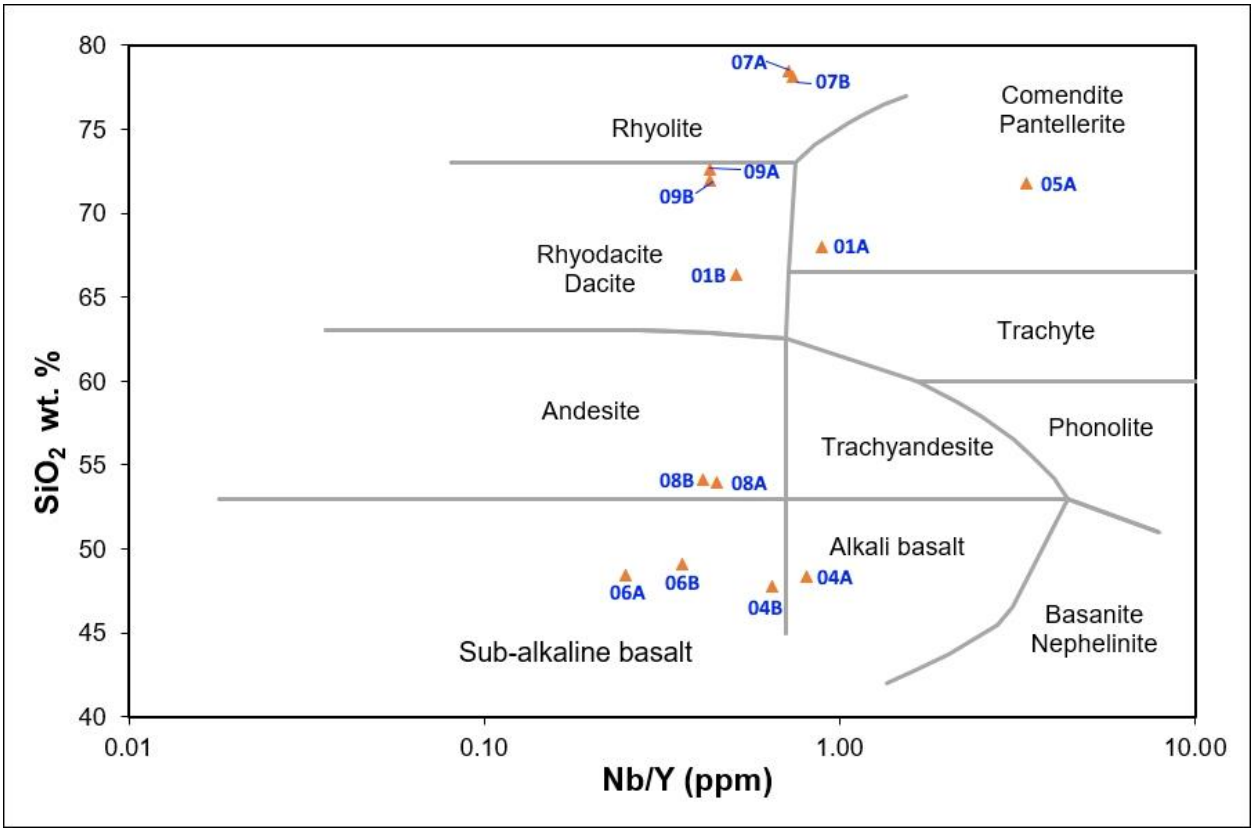

Figure 16: XRF data displaying possible igneous protoliths for altered samples (Winchester & Floyd 1977).

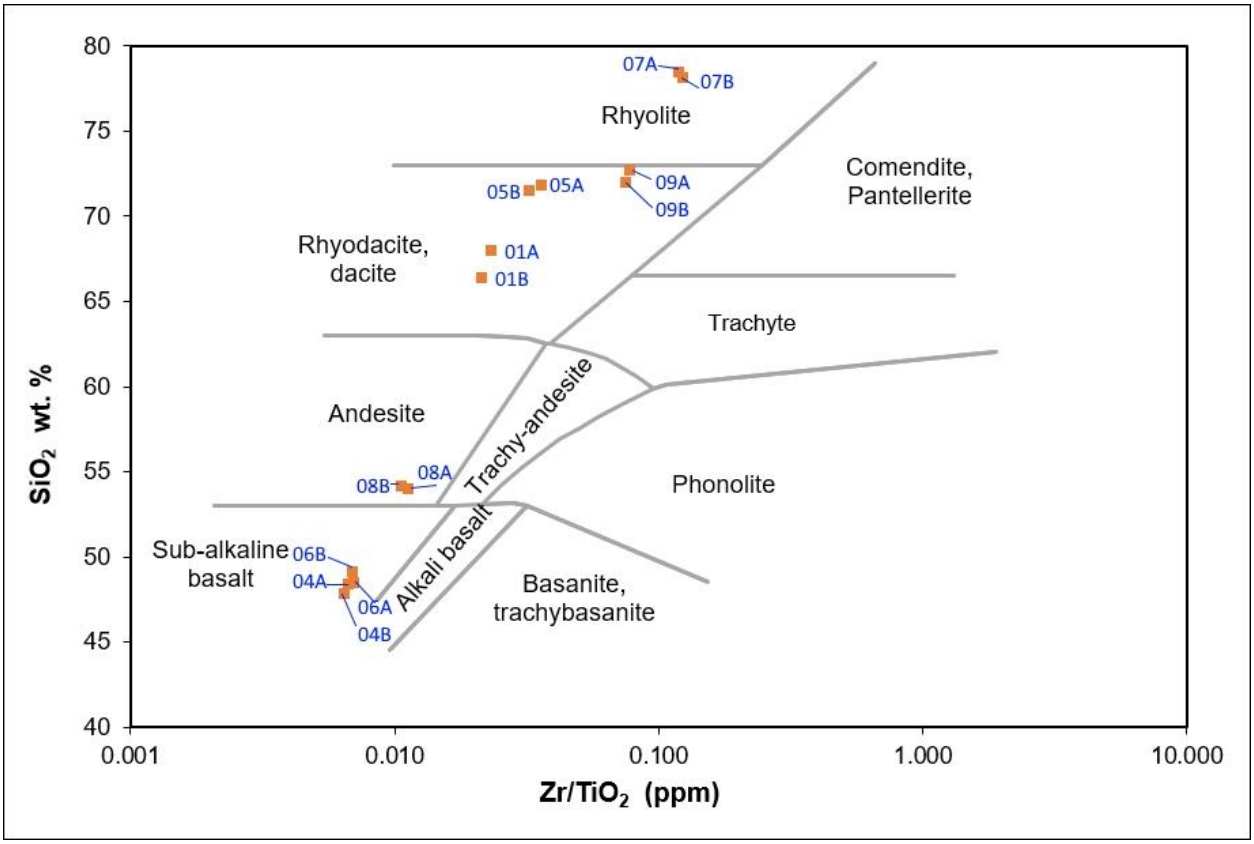

Figure 17: XRF data displaying possible igneous protoliths for altered samples (Winchester & Floyd 1977).

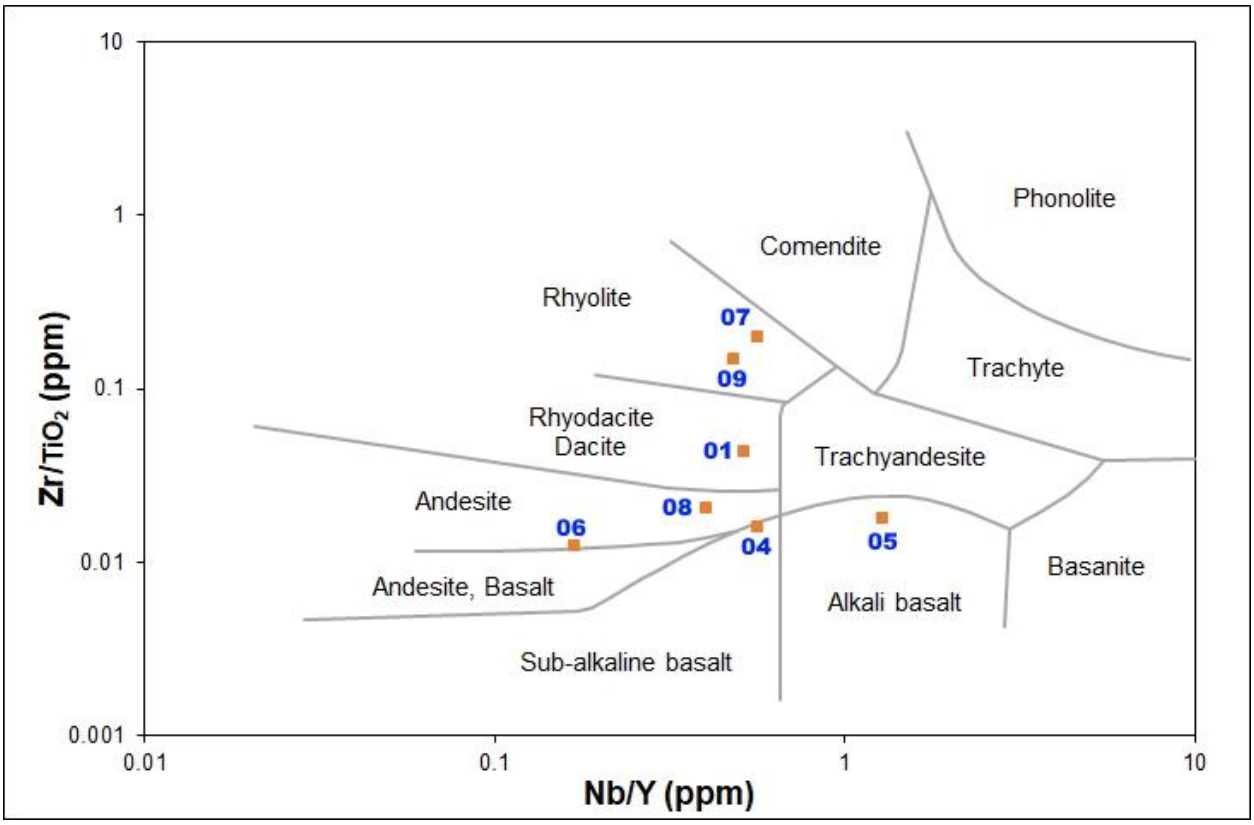

Figure 18: ICPMS data displaying possible igneous protoliths for altered samples (Winchester & Floyd 1977).

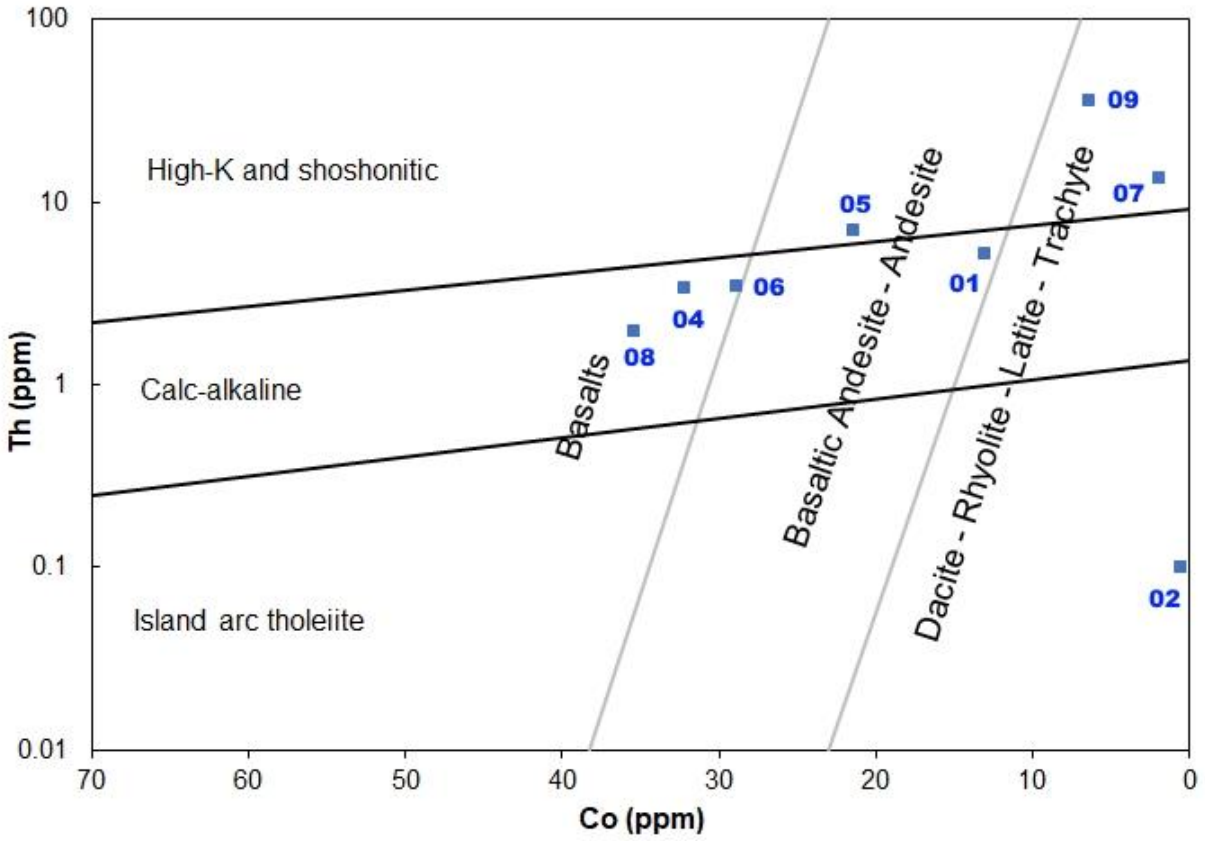

Figure 19: ICPMS data displaying possible igneous protoliths for metamorphosed samples (Hastie et al., 2007).

Felsic samples	Figure 16 (XRF)	Figure 17 (XRF)	Figure 18 (ICPMS)	Figure 19 (ICPMS)	Proposed geochemical lithology
16MT01 A	Comendite Pantellerite	Rhyodacite Dacite	Rhyodacite Dacite	Calc-alkaline andesite	Granodiorite
16MT01 B	Rhyodacite Dacite	Rhyodacite Dacite			
16MT02 A	*Inconclusive*	*Inconclusive*	*Below detection limit*	Island arc tholeiite felsic	K-Feldspar intrusion
16MT02 B	*Inconclusive*	*Inconclusive*			
16MT03 A	Metased.	Metased.	Metased.	Metased.	Metased.
16MT03 B	Metased.	Metased.			
16MT07 A	Rhyolite	Rhyolite	Rhyolite	High-K and shoshonitic rhyolite	Granite
16MT07 B	Rhyolite	Rhyolite			
16MT09 A	Rhyodacite dacite	Rhyodacite dacite	Rhyolite	High-K and shoshonitic rhyolite	Rhyolite
16MT09 B	Rhyodacite dacite	Rhyodacite dacite			

Mafic samples	Figure 16 (XRF)	Figure 17 (XRF)	Figure 18 (ICPMS)	Figure 19 (ICPMS)	Proposed geochemical lithology
16MT04 A	Alkali basalt	Sub-alkaline basalt	Sub-alkaline basalt	Calc-alkaline basalt	Sub-alkaline basalt
16MT04 B	Sub-alkaline basalt	Sub-alkaline basalt			
16MT05 A	Comendite Pantellerite	Rhyodacite Dacite	Alkaline basalt	High-K and shoshonitic basaltic andesite	Alkaline basalt?
16MT05 B	*Ratio is too high to plot*	Rhyodacite Dacite			
16MT06 A	Sub-alkaline basalt	Sub-alkaline basalt	Andesite	Calc-alkaline basalt	Andesite
16MT06 B	Sub-alkaline basalt	Sub-alkaline basalt			
16MT08 A	Andesite	Andesite	Andesite	Calc-alkaline basalt	Andesite
16MT08 B	Andesite	Andesite			

Table 1: Generated to compile the results from figures 16-19 (Winchester & Floyd 1977). 16MT02 A could not be plotted because data on the Y axis exceeded the graphing parameters. 16MT02 B could not be plotted Nb was below detection limit for ICPMS and Y was below detection limit for XRF. Note that, for metamorphosed samples, the geochemical lithology represents an inferred protolith.

Zircon geochronology and geochemistry

U-Pb ages

U-Pb data that were collected at the University of Arizona's LaserChron lab, were entered into IsoplotR to plot concordia diagrams. Figures of the concordia diagrams show three MSWD values where the first number is the MSWD for concordance, the second number is the MSWD for equivalence, and the last being the MSWD for concordance + equivalence (Vermeesch, 2018). MSWD values for equivalence are reported with for completeness, but not considered as a factor when determining age. The decision whether to keep analyses for age calculation was based on its proximity to the main age population rather than determining the best concordance + equivalence MSWD (Horstwood et al., 2016). Age data that are greater than

five percent discordant or otherwise tens of million years off the mean age were not considered for age calculation. Tera-Wasserburg concordia diagrams were utilized in lieu of the typical concordia plot as it tends to be better suited for older age analyses (Tera and Wasserburg, 1975).

16MT03

16MT03 (Fig. 20) is a metasedimentary rock whose zircons have a detrital origin with a maximum zircon crystallization age of 2.841 Ga, a minimum of 1.782 Ga and a range of 1.059 Ga. Six of those ages (No. 1-6) have been utilized to determine a minimum concordia age for the rock, 1,803.65 ± 4.62 Ma. This was our only sample of those that were dated that yielded presumed detrital zircons and were too small of a sample for provenance studies.

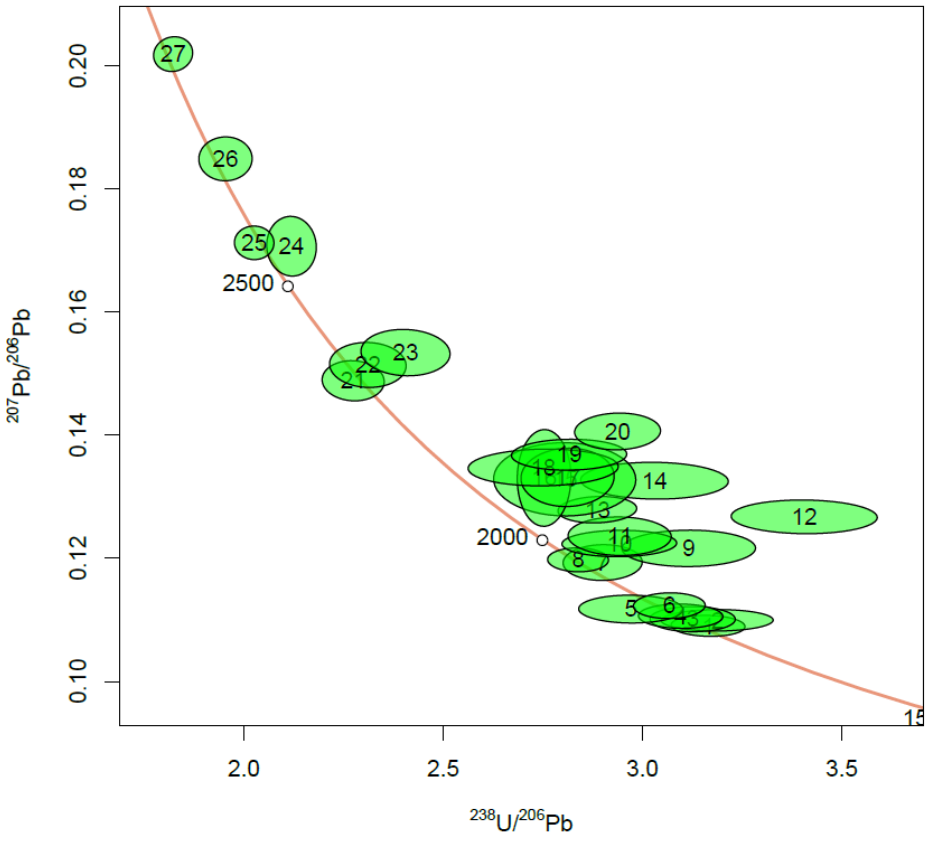

Figure 20: Tera-Wasserburg concordia diagram of 16MT03. A wide spread of ages is suggestive of a detrital origin.

16MT04

Nineteen concordant analyses of the twenty-nine taken for 16MT04 (Fig. 21) were used to obtain a concordia of 1,858.05 ± 1.00 Ma, with an MSWD value of 1.7. Analyses 1, 2, and 29 were removed the age calculation due to a large differential – greater than five percent – from the proposed mean. Analyses 3, 5, 6, 9, 14, 15, and 20 were more than five percent discordant and not considered for age calculation. The age of 1.858 Ma is interpreted to reflect the age of protolith crystallization.

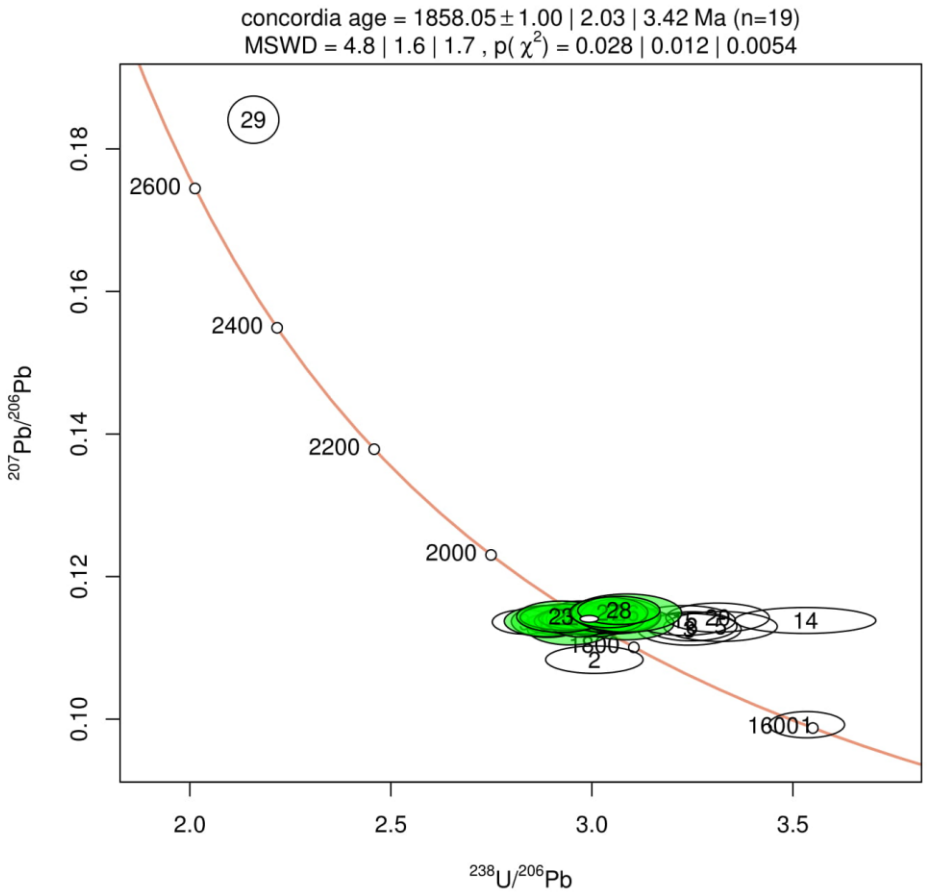

Figure 21: Tera-Wasserburg concordia diagram of 16MT04.

16MT05

16MT05 (Fig. 22) yielded a mean age of 1,860.46 ± 1.00 Ma with an MSWD of 3.9. Thirty analyses were conducted with 25 concordant analyses being utilized to calculate age. Analyses 1, 2, 7, 29 and 30 were disregarded due to poor concordancy and/or a large discrepancy in age from the proposed mean. Two zircons were ablated near their cores and rims. Analyses 18 (core) and 13 (near the rim) revealed ages of 1,851.56 ± 10.77 Ma and 1,840.96 ± 13.10 Ma respectively. Analyses 26 and 8 were also a part of a core-rim age test with ages of 1,868.99 ± 12.13 Ma and 1,834.19 ± 13.61 Ma respectively. The age of 1,860 Ma is interpreted to reflect the age of protolith crystallization.

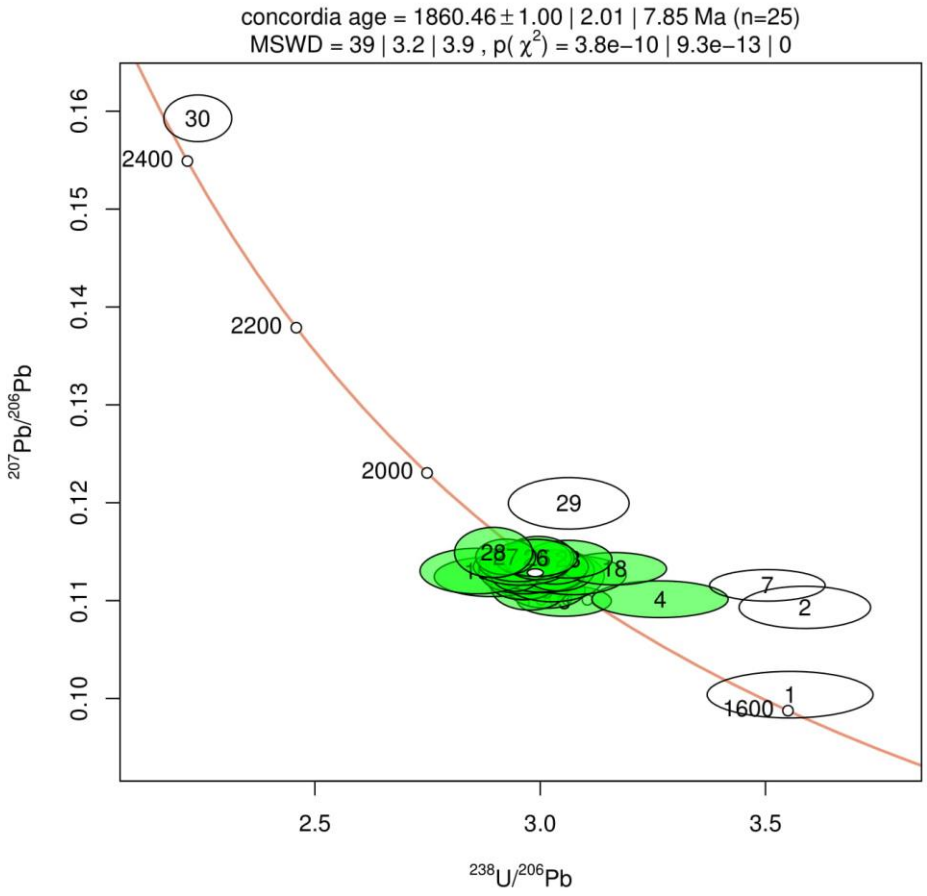

Figure 22: Tera-Wasserburg concordia diagram of 16MT05.

16MT07

Twenty-four concordant analyses were utilized for an age proposal of 1,857.73 ± 1.00 Ma for 16MT07 with an MSWD value of 1.9. Analyses 1, 22, 32, and 35 were not considered due to discordancy values greater than five percent. Analyses 2, 6, 8, 19, 30 and 34 were not considered in part to their ages and discordance values of about three percent. Analyses 26 and 10 were a part of a core-rim test with ages of 1,854.12 ± 11.96 Ma and 1,834.12 ± 10.42 Ma. Three other core-rim tests were conducted, but they were several percent discordant. The age of 1,854 Ma is interpreted to reflect the age of the host rock crystallization.

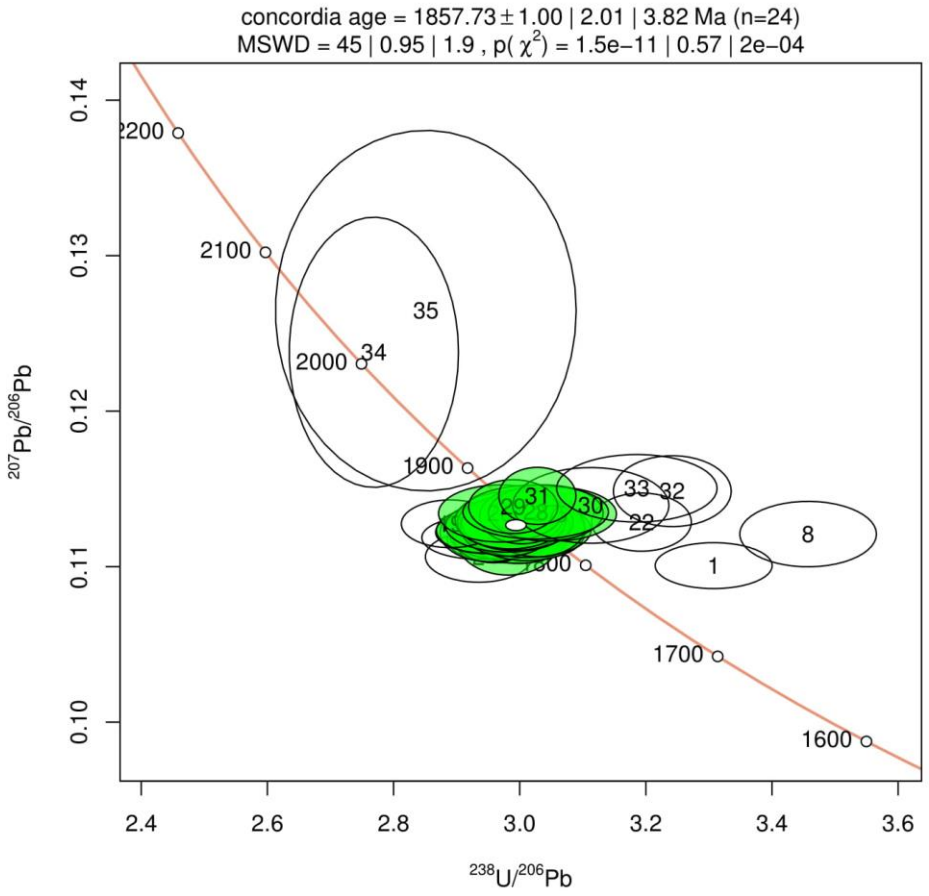

Figure 23: Tera-Wasserburg concordia diagram of 16MT07.

16MT09

Analyses 1, 3, 8, 13, 14, 22, 23 and 23 were not considered for age calculation from 16MT09 (Fig. 24) due to age discrepancies or greater than five percent discordancy. An age of 2,542.72 ± 1.00 Ma with an MSWD of 0.83 is proposed. This age is calculated from twenty concordant analyses from a total of twenty-eight collected. The age of 2,542 Ma is interpreted to reflect the age of protolith crystallization.

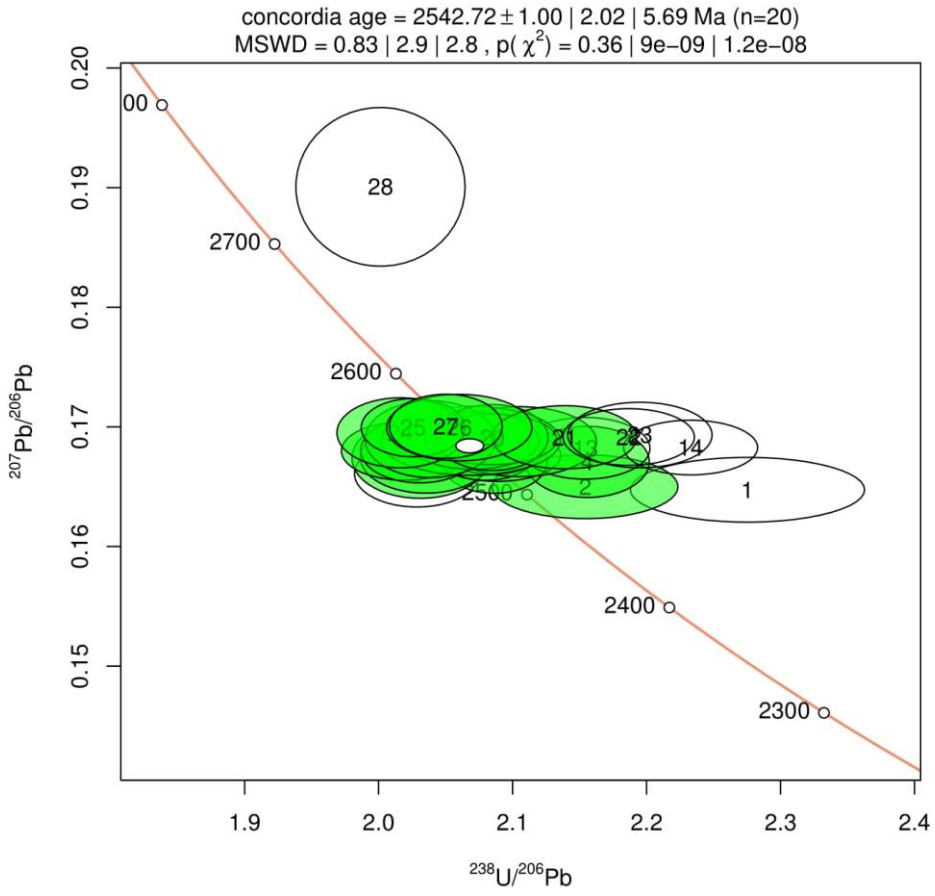

Figure 24: Tera-Wasserburg concordia diagram of 16MT09.

Lu-Hf system

16MT03 was not analyzed due for Lu-Hf because of the wide spread of ages suggests a detrital origination and not enough detrital samples were collected to generate conclusive results. Lu-Hf data collected from 16MT04, 16MT05, 16MT07, and 16MT09 are presented in figure 25. 16MT04, the porphyritic amphibole biotite schist has yielded a crystallization age of 1,858 Ma. Lu-Hf depleted mantle model ages indicate an older source, with a model age of c. 2,160 Ma. εHf lies between 2.1 and 5.3 for most of the analyses indicating a juvenile origin. 16MT05, an amphibole quartzofeldspathic gneiss yielded a crystallization age of 1,860.46 ± 1.00 Ma. Lu-Hf

depleted mantle model ages indicate an older source with a model age of c. 2,250 Ma. εHf values lay between 0.4 and 3.4 for most of the analyses indicating a juvenile origin. 16MT07 is a biotite alkali feldspar granite with a crystallization age of 1,857 Ma. Lu-Hf model ages depict a much older source with a depleted mantle model age of c. 3,150 Ma. εHf values lay between -13.2 and -15.4 for most analyses. 16MT09 is an altered and weathered meta-rhyolite with a crystallization age of 2,542 Ma. Lu-Hf depleted mantle model ages range around c. 3,350 Ma. εHf values lay between -6.3 and -10.6 for most analyses.

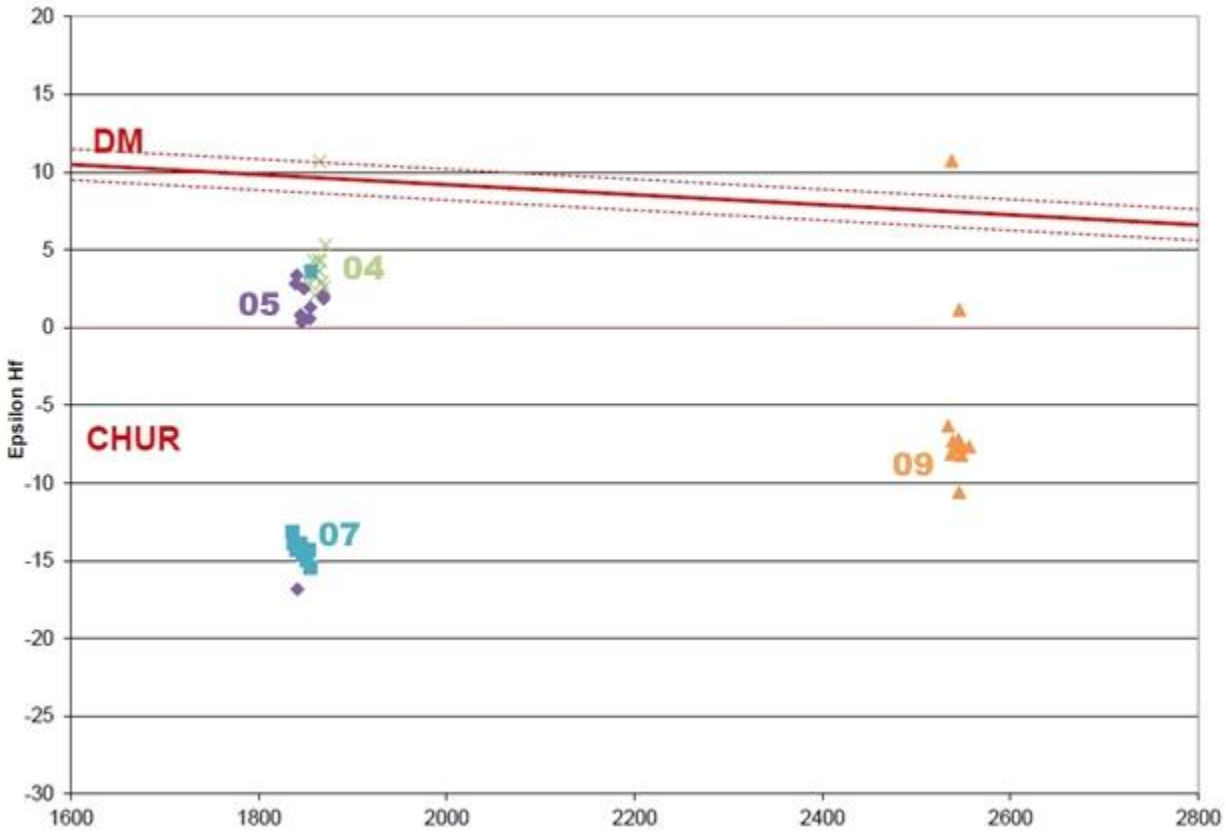

Figure 25: $\varepsilon Hf_{(t)}$ versus U-Pb crystallization ages for 16MT04 (green xs), 16MT05 (purple diamonds), 16MT07 (blue squares) and 16MT09 (orange triangles). Average error of εHf analyses is 0.7.

Discussion

Geochemical evidence for a volcanic arc origin from trace element variations

Several normalized multi-element variation diagrams were generated based on ICPMS data, to help characterize the plate tectonic setting that the samples originated in. Figure 28 displays N-type MORB normalization of the Marshfield Terrane utilizing values from Sun and McDonough (1989). The Marshfield Terrane samples all feature enrichment in the more incompatible elements and depletion of the more compatible elements when compared to MORB. There are strong depletions of Sr, and Ta-Nb-Ti. Depleted levels of strontium in granitic rocks are not to be unexpected in older rocks, as it is a very mobile element with respect to weathering (Middelburg et al., 1988). Depletions of niobium compared to potassium, lanthanum and titanium compared to europium, terbium and dysprosium is characteristic of both continental crust as well as consistent with material originating in arc systems (Fig. 29) (Kelemen et al., 1993; Sun and McDonough, 1989), and is not seen in mid-ocean ridge basalts (Kelemen et al., 1993; Pearce and Cann, 1973). For arc magmas, these depletions may be accompanied by depletion of zirconium (Kelemen et al., 1993) as well as Ta and Ti (Szilas, 2018). Negative Ta-Nb-Ti anomalies are observed in all samples (Fig. 30). These depletion values re-support our tectonic discrimination diagrams showing that the Superior Province, Pembine-Wausau Terrane and the Marshfield Terrane converged together through a modern style plate tectonic regime during the Paleoproterozoic Penokean Orogeny. There is some dispute regarding whether plate tectonics is active this early in Earth's history (Stern, 2008; Hamilton, 2011), however previous data and data presented in this study are consistent with a modern style volcanic arc setting

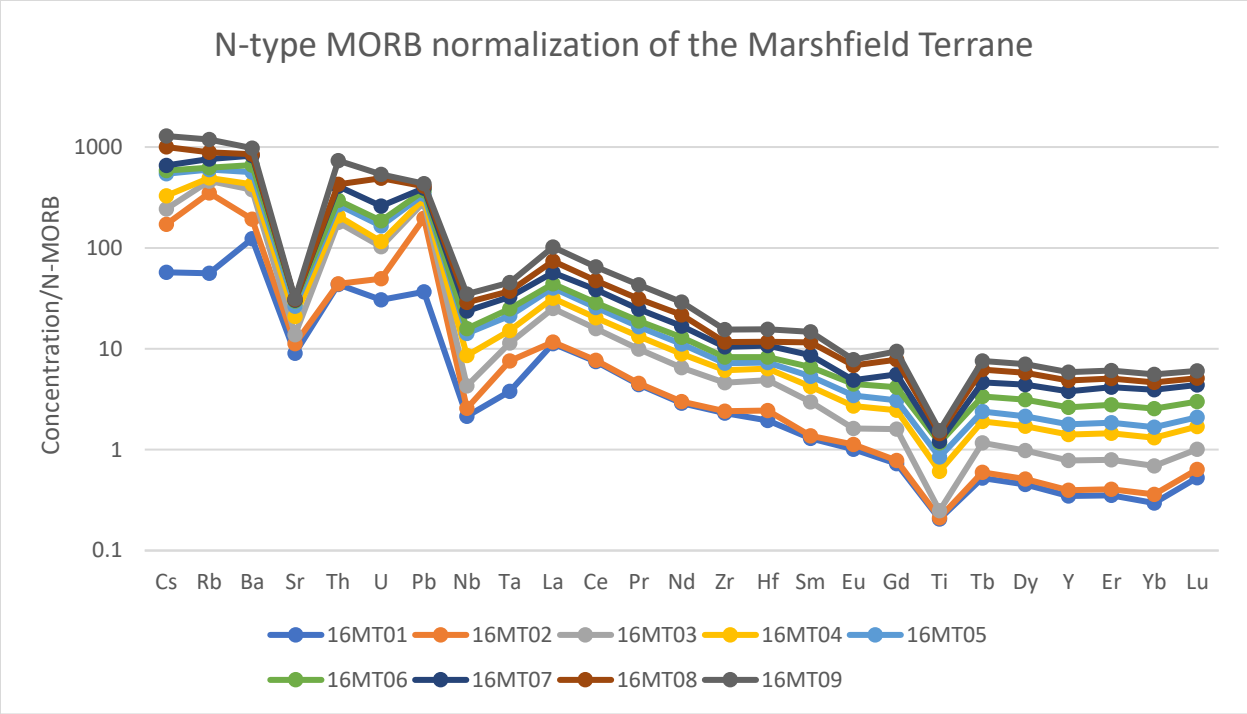

Figure 28: Whole-rock trace element plot for the nine Marshfield terrane sample, normalized to N-MORB values after Sun and McDonough (1989).

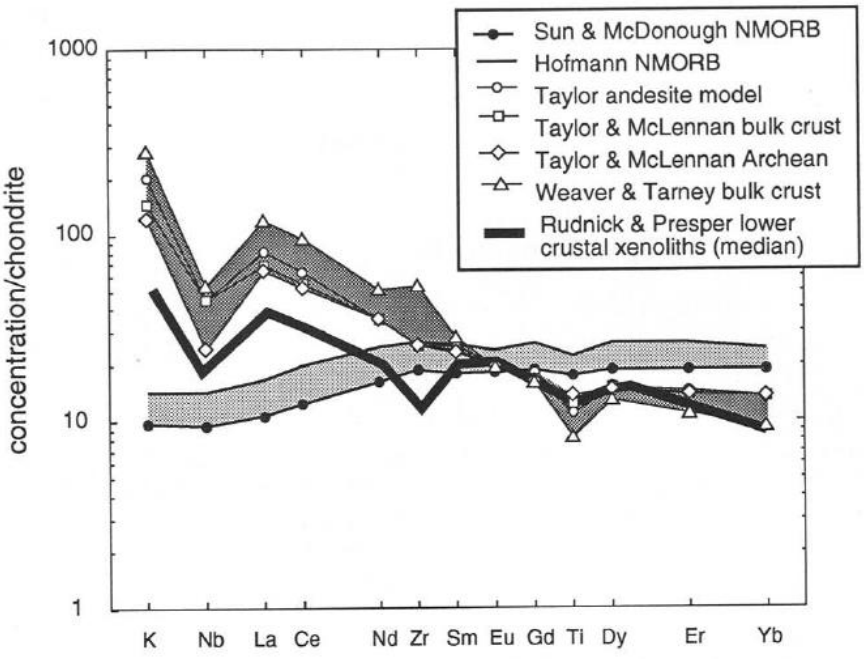

Figure 29: Trace element mean compositions for continental crust, lower crustal xenoliths, high Mg andesites and others. All Marshfield terrane samples show enrichment in light REE and depletions of Nb and Ti commonly observed in the continental crust, and rock formed in volcanic arc environments (Keleman et al., 1993).

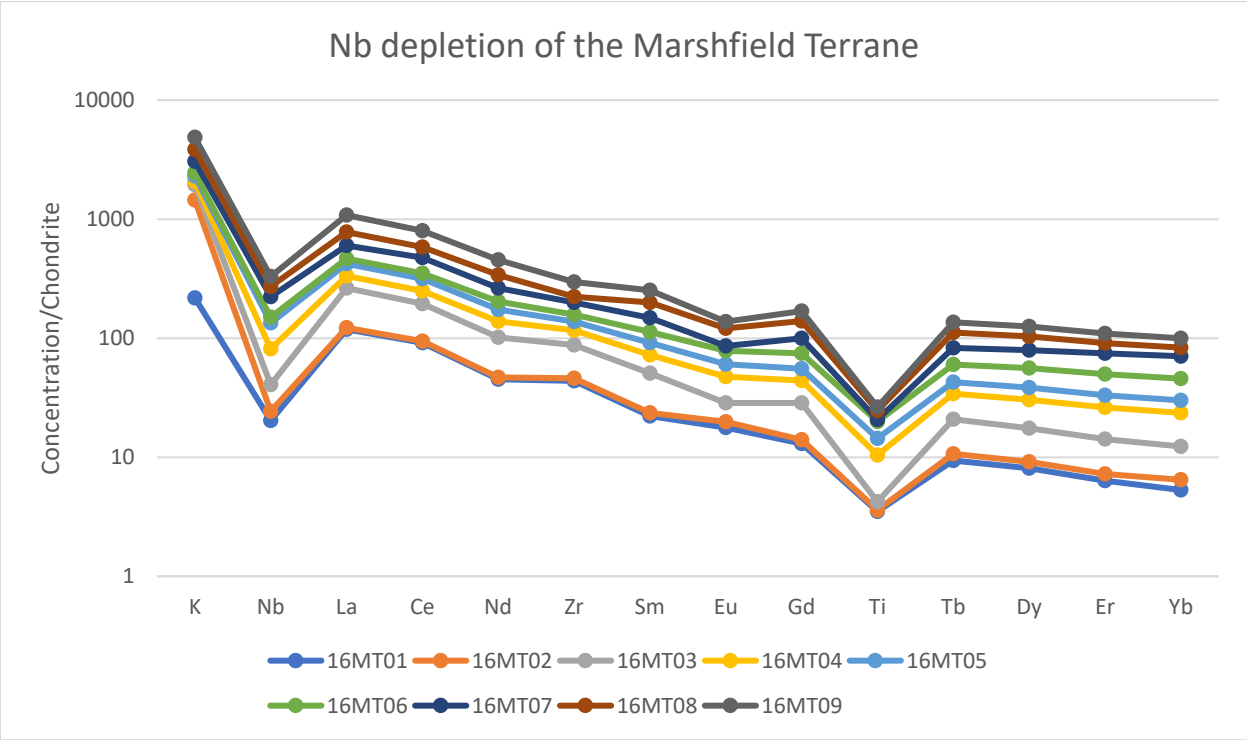

Figure 30: A trace element variation diagram as formatted by Kelemen et al. (1993) to highlight Nb and Ti anomalies commonly associated with continental crust and volcanic arc rock. As shown in the figure 29, most samples display similar trends and feature depletions of Nb and Ti. Chondrite normalization after Sun and McDonough (1989).

Most of the discussion above is based on investigations utilizing modern rock; however, due to the age of the Marshfield terrane samples, it is informative to utilize geochemical signals tested in such old rock. Recent geochemical analyses on mid-Archean metavolcanic rocks from southwestern Greenland (3.0-2.8 Ga) highlight two distinct geochemical suites, tholeiitic basalts and calc-alkaline andesites (Szilas, 2018). These two suites may be separated by their La/Sm ratio where a value lower than three indicates tholeiitic protoliths and values greater than three

indicates calc-alkaline andesitic protoliths (Szilas, 2018). The tholeiitic basaltic group is the much more common of the two and consists of mantle derived rocks with relatively flat slopes on chondrite normalized multi-element variation diagrams (Szilas, 2018). This pattern on multi-element variation diagrams is reflected globally in Archean greenstone terranes (Szilas, 2018). The calc-alkaline andesite group is unusual because it features a much less common lithology with respect to Archean cratons (Szilas, 2018). The group has a significant felsic component which may be a representation of felsic-mafic mixing or due to partial melting of mafic crust (Szilas, 2018). This group is characterized by a more steeply dipping slopes on multi-element variation diagrams. Both geochemical suites feature the negative Ta-Nb-Ti anomalies associated with modern-style volcanic arc rocks (Szilas, 2018; Zheng, 2019). Except for 16MT06, all our samples feature La/Sm ratios above three which is indicative of a calc-alkaline andesite. It is unlikely that these two groups could be split by fractional crystallization because there is little to no negative Eu anomaly – an indication of plagioclase fractionation. To test this connection, we generated two multi-element variation diagrams in the same format as Szilas (2018) (Fig. 31 and 32). Our geochemical signature is very similar to that of the calc-alkaline andesite group with negative Ta-Nb-Ti anomalies and a negative slope towards compatible elements. This high La/Sm group is characterized by a steeply sloping chondrite normalized REE diagram with small Eu negative anomalies. The same signature is found for the Marshfield Terrane samples in this study (Fig. 32). These data indicate that the Marshfield Terrane has a strong arc influence when compared to Archean greenstone terranes, and the andesitic protolith indicates a potential for felsic and mafic mixing as confirmed by Lu-Hf zircon geochemistry. Chondrite normalized variation diagrams diagram shows distinct trends as well with prominent depletion in Pb, Sr and Ti. Samples 05, 07 and 08 which were identified to have shoshonitic affinities (Fig. 19).

Shoshonites typically feature pronounced enrichment in LIL elements with respect to chondrite normalization (Murphy, 2006; Murphy, 2007) and that signature is reflected in figure 32. Shoshonites are subduction related, alkali-rich trachyandesites that may occur with calc-alkaline volcanism or continental arcs (Murphy, 2007). Subduction in these systems is usually identified by pronounced negative Ta-Nb-Ti anomalies (Murphy, 2007). which has been identified on all our normalized multi-element variation diagrams.

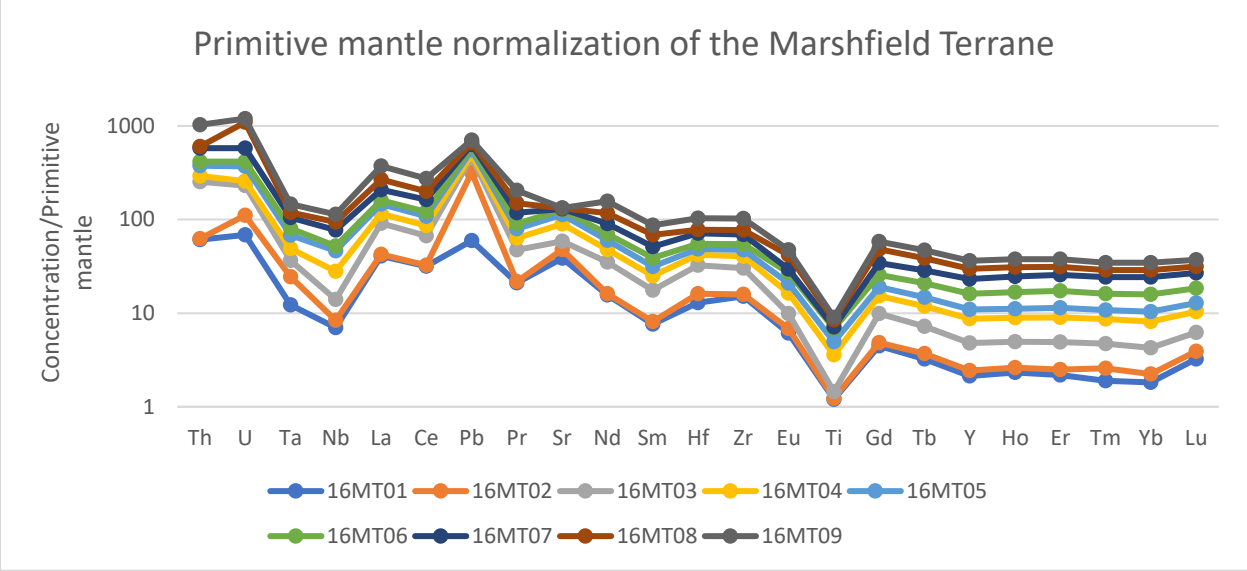

Figure 31: Primitive mantle normalization of the Marshfield Terrane. Element order as by Szilas (2018) and normalization from Sun and McDonough (1989).

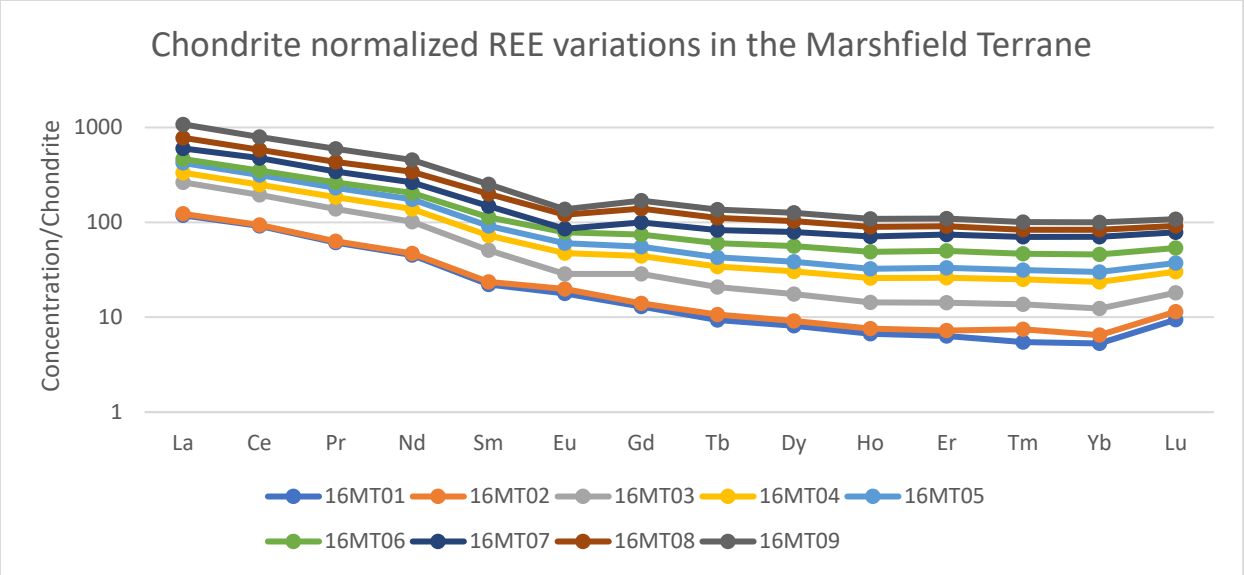

Figure 32: Chondrite normalized of Rare Earth Elements (REE) variation diagram. Element order as by Szilas (2018) and normalization from Sun and McDonough (1989).

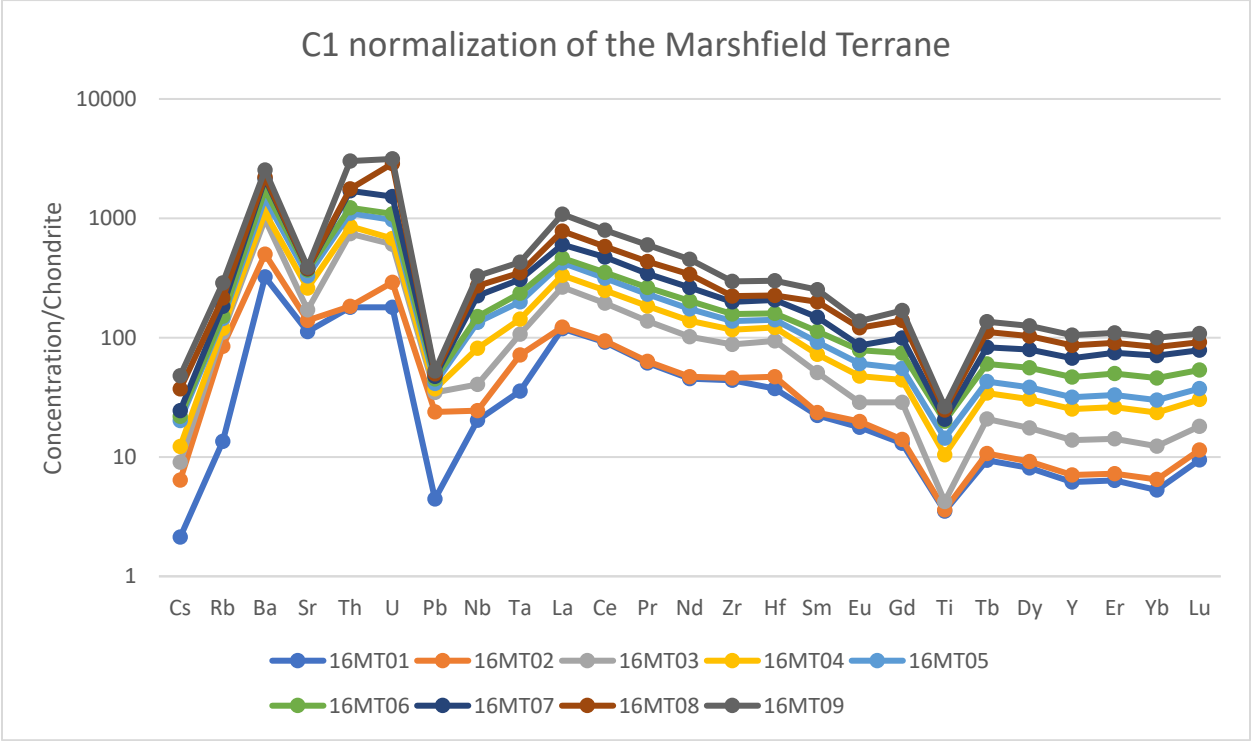

Figure 33: Chondrite normalized multi-element variation diagram of the Marshfield Terrane samples. Element order and normalization from Sun and McDonough (1989).

Geochemical evidence for a volcanic arc origin from tectonic discrimination diagrams

To constrain possible tectonic settings for our samples, two tectonic discrimination diagrams were created. Figures 33 and 34 (Hollocher et al., 2012) utilize immobile trace elements to help constrain the plate tectonic environment our rocks formed in. Figure 33 plots the ratio of Nb'/La versus La/Yb. Nb' may represent either actual Nb values or Ta which is converted to an equivalent of Nb through an equation (Hollocher et al., 2012). The data herein uses actual Nb values many Ta values were below the detection limit. 16MT01, 16MT05, 16MT08 and 16MT09 plotted in the alkaline arc field, whereas 16MT04, 16MT06, and 16MT07 plot in the continental arc field. 16MT02 and 16MT03 are not included on the diagram due to their pegmatitic and detrital respective origins. Figure 34 utilizes the ratio of Th/Nb versus La/Yb and tells a very similar story. Except for 16MT08, which lies in the oceanic island arc field, the rest of the samples plot in the same fields as they did on the previous diagram. Figure 35 a and b utilizes immobile elements from Pearce et al. (1984) for felsic discrimination. Again, samples 16MT02 and 16MT03 are not included on the diagram. These felsic discrimination diagrams utilize the ratios of Nb versus Y and Ta vs Yb. All viable samples plot in the volcanic arc granitoid field which indicates a paleotectonic system of either an oceanic or continental arc and agrees with figures 33 and 34 (Pearce et al., 1984; Pearce 1996; Winter, 2010). The data from these discrimination diagrams support previous studies that suggest that the Marshfield Terrane is a displaced continental fragment, and that the Superior Province, Marshfield Terrane, and Pembine-Wausau Terrane converged together through tectonic processes (subduction of oceanic crust) during the Paleoproterozoic Penokean Orogeny.

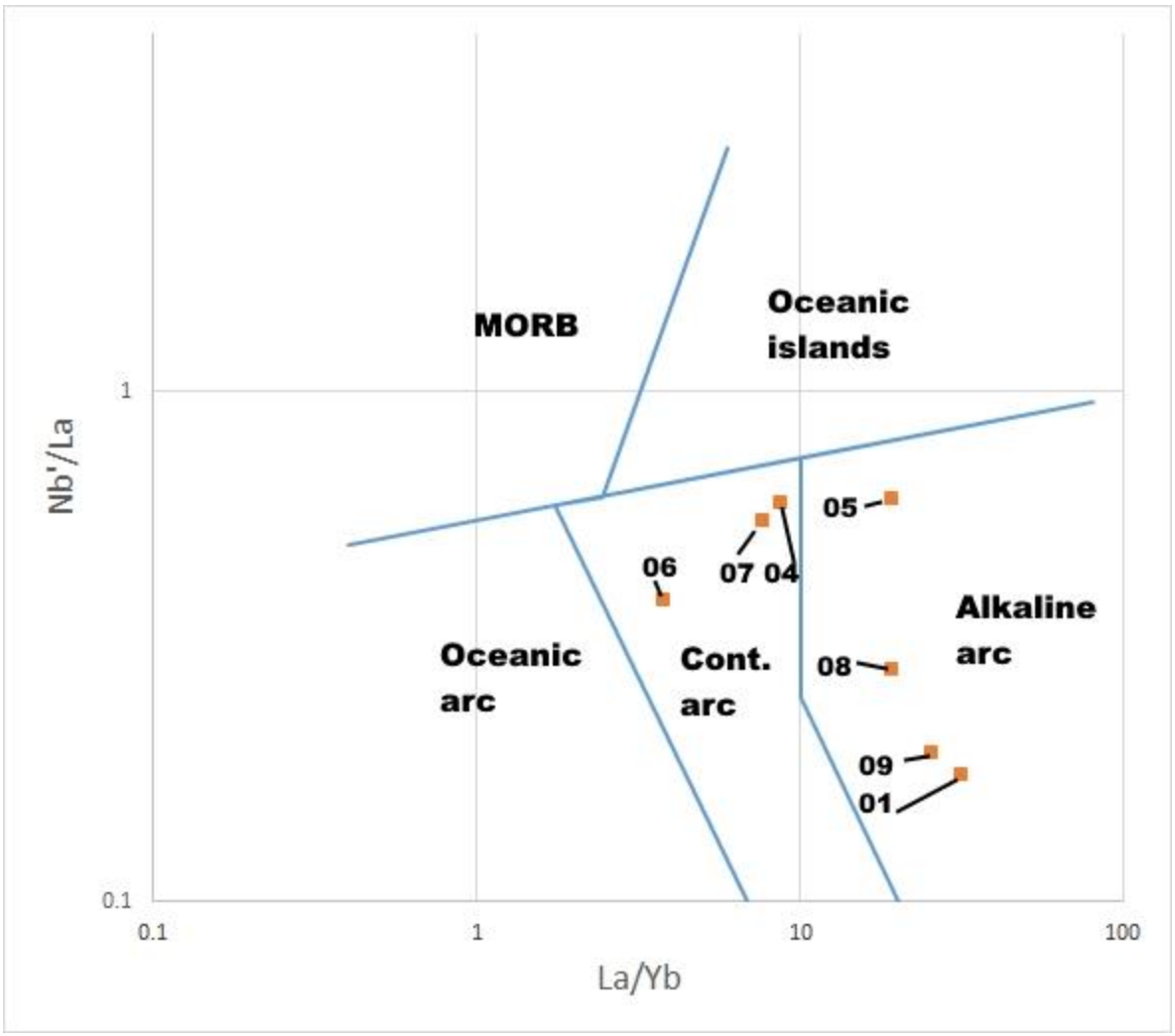

Figure 33: Tectonic discrimination of viable samples. Discrimination diagram from Hollocher et al. (2012).

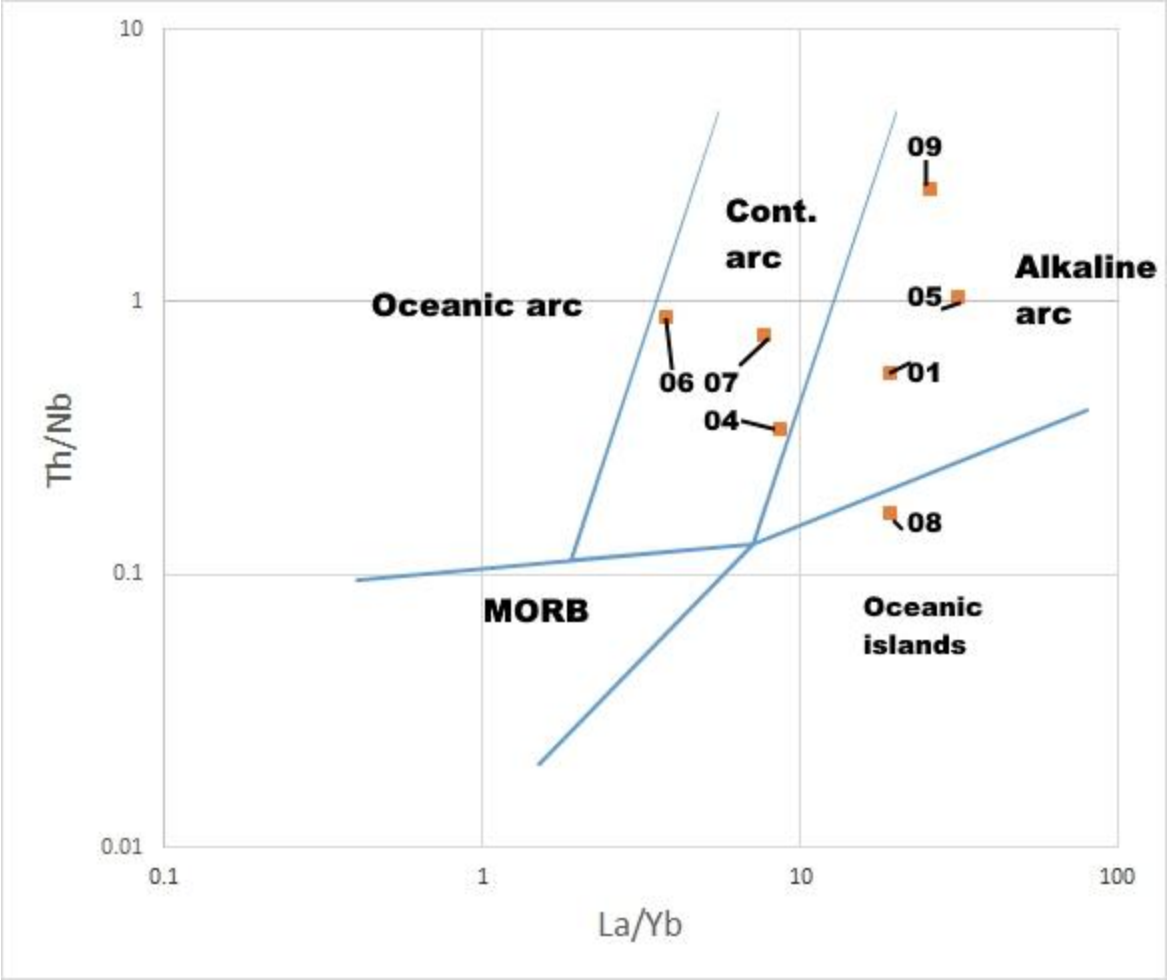

Figure 34: Tectonic discrimination of viable samples. Discrimination diagram from Hollocher et al. (2012).

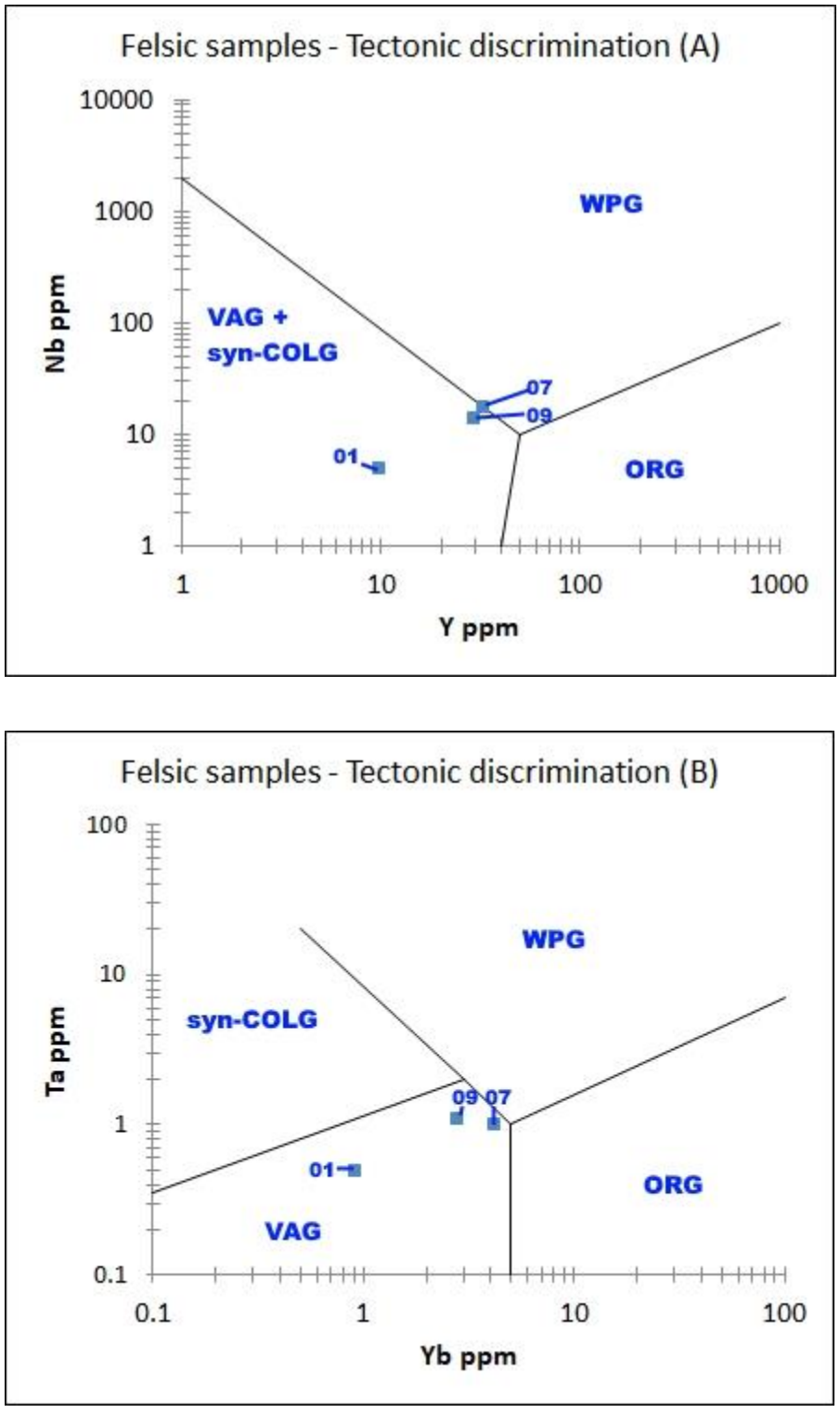

Figure 35: Tectonic discrimination of felsic samples. Discrimination diagram from Pearce et al. (1984). Figure A utilizes the ratio between Nb, and Y and figure B utilizes Ta and Yb.

Evolution of the Marshfield Terrane evaluated from zircon U-Pb and Lu-Hf data

The Marshfield Terrane is proposed herein to be a Late Archean, Early Proterozoic entity based on five analyses which agrees with previous studies. Our Paleoproterozoic ages are clustered between 1,857 Ma and 1,860 Ma (Late Orosirian) and our single Archean age is 2,542 Ma (Late Neoarchean). The Orosirian ages fit well with the c. 1,890-1,850 Ma time frame of the Penokean orogenic event as described by Sims et al. (1989) and Schulz and Cannon (2007). The U-Pb ages presented herein vary quite strongly from Hf model ages that indicate an older source environment. Mafic samples 16MT04 and 16MT05 have model ages 302 Ma and 390 Ma older with, $\varepsilon Hf_{(T)}$ ranging between +2.8 – +5.3, and +0.4 – +3.4 respectively. 16MT04, the amphibole biotite schist, is proposed to be a metamorphosed calc-alkaline basalt produced in a subduction related continental arc setting, and this concurs with positive εHf which indicate the source environment is somewhat depleted. The most likely outcome to yield these results is an original mafic melt which was generated much earlier than the crystallization age and later crystallized in the lower crust. After this point, it likely laid dormant for at least 302 Ma before being remelted during the Penokean arc magmatism event at 1,858 Ma. A similar geological history is proposed for 16MT05, as the Lu-Hf model age precedes the crystallization age by 390 Ma. Whole-rock geochemistry suggests that the protolith was an alkaline basalt or basaltic-andesite with shoshonitic affinities produced in a subduction related continental arc setting. Positive εHf values again suggest that the rock originated from modest reworking of older material in a relatively juvenile system. In both cases, the age of the source material is difficult to constrain, with the model ages only suggestive of minimum ages of separation from a depleted mantle source.

This is contrasted by the two felsic samples, 16MT07 and 16MT09, which both have enriched $\varepsilon Hf_{(t)}$ values between -13.2 – -15.4 and -6.3 – -10.6, respectively. T_{DM} model ages are

1,293 Ma older and 808 Ma older than the crystallization ages respectively. Like 16MT04 and 16MT05, 16MT07 is among the Orosirian ages, but its T_{DM} model age is much older, at 3,150 Ma (Paleoarchean). 16MT07 is proposed to be a volcanic arc granite that has been microstructurally deformed and enriched in Potassium and has shoshonitic affinities. This sample is presumed to have originated from c. 3,150 Ma crust, which was later melted during the Penokean Orogeny in a subduction related volcanic arc system. This led to the crystallization of the granite at 1,857 Ma. 16MT09 is enriched as well (-6.3 – -10.6) but to a lesser degree that 16MT07. The 16MT09 age crystallization age is considerably older than our other samples at 2,542 Ma. 16MT09 is proposed to be a deformed, weathered rhyolite with a much older source than its crystallization age, with a T_{DM} model age of c. 3,350 Ma. This sample, which was collected near a c.2.8 Ga metagabbro (Sims et al., 1989), provides a geochemical glimpse into the Archean basement to the terrane, tentatively revealing an earlier phase of subduction and crustal reworking.

Preliminary whole-rock geochemical results across the board illustrate the role of subduction in the terrane origin and tectonic evolution. Felsic samples yielded a geochemical signature typical of a volcanic arc system, including enrichments in LIL elements, depletions in HFS elements, and characteristic negative Nb and Ta anomalies – consistent with a supra-subduction zone origin. Tectonic discrimination diagrams based on trace element geochemistry help to further constrain the origins of these metaigneous rocks. Mafic samples of the Marshfield Terrane were found to be plate margin basalts which formed in a continental arc system. These data support previous studies which suggest that the Marshfield Terrane is a displaced continental fragment, and that the Superior Province, Marshfield Terrane, and Pembine-Wausau Terrane converged together through subduction of oceanic crust during the Paleoproterozoic

Penokean Orogeny. These data concur with the highly potassic and shoshonitic affinities from 16MT05, 16MT07 and 16MT09 which is also indicative of subduction (Morrison, 1980). Evidence for tectonic deformation is found petrographically. The samples commonly feature micro-deformation structures such as undulatory extinction in quartz and feldspars, bent twinning in feldspars, domino-type fragmented porphyroclastic feldspars, dynamic quartz recrystallization, and general strain textures. The straining across all samples was unexpected because it was not always shown at the macroscopic level, as was the case for 16MT01 and 16MT07. The samples all feature a variable amount of weathering with development of symplectic sericite within feldspar grains.

Comparison with previous studies

U-Pb geochronology and Lu-Hf geochemistry on Marshfield Terrane zircons reflect upon a much more complex assemblage than historical studies have identified. The relationship between the Archean and Paleoproterozoic ages is complex (Fig. 31). Sims et al. (1989) had little age data, but a few are available for comparison. Gneiss at Jim Falls (Sims sample thirty-nine) (16MT03) and felsic gneiss at Arbutus dam (16MT09) (Sims sample forty-one) which have been dated at 2.5 and 2.8 Ga respectively (Sims et al., 1989) and were resampled for this study. 16MT03 yielded metasedimentary origins, whereas 16MT09 yielded an age of 2542 which is several hundred Ma younger than the c. 2,800 Ma proposed in Sims et al. (1989). This may represent a different sample lithology, however, as several are present in a small area below the dam. Sims et al. (1989) samples 6, 7, 32, 38, 40, 41 were taken in river valleys near Neillsville, WI, which have been eroded down from the overlying sedimentary Paleozoic strata. Sims et al. (1989) samples 6, 7, and 32 constitute a foliated tonalite, two granites with Paleoproterozoic ages of 1,831 ± 7, 1,835 ± 6 Ma, and 1,871 ± 5 Ma. In contrast, gneissic samples 38, 40 and 41 reflect

Archean ages of 2,516 ± 5 Ma, 2,522 ± 22, and c. 2,800 (Sims et al., 1989). Our dated samples 16MT07 and 16MT09 were taken from the same region (Fig. 31) and reflect this Paleoproterozoic-Archean juxtaposition. Approximately 80-100 miles to the northwest of the Neillsville, WI bands is a triangular shaped region, which constitutes Mesoarchean gneisses (Sims et al., 1989). Samples 16MT04 and 16MT05 were sampled from the same area and feature much younger crystallization ages of 1,858 Ma and 1,860 Ma (Orosirian); however, Lu-Hf T_{DM} model ages are 2,160 Ma and 2,250 Ma (Rhyacian). The crystallization ages are consistent with Penokean orogenic event, but the Lu-Hf model ages predate known evidence of the orogeny. Van Wyck and Johnson (1997) utilized Sm-Nd isotopic studies to determine Marshfield Terrane model ages. Sm-Nd which is roughly comparable to Lu-Hf. Nd-Sm provide an origin for the initial composition of the melt and are not easily influenced by metamorphic events (Fisher et al., 2010). Like Lu-Hf, Nd-Sm are not easily disturbed and the initial Nd composition can be calculated and is suggestive of a tectonic setting – the initial composition of the source material. By chance, Marshfield sampling herein is greater than a few miles away from sites chosen by Van Wyck and Johnson (1997). Regardless of different isotopic systems and sampling of different sites, Sm-Nd and Lu-Hf are roughly comparable (Kinny and Maas, 2003). Most of the samples analyzed by Van Wyck and Johnson (1997) consist of synorogenic intrusive rocks with ages between 1,825 Ma – 1,871 Ma which aligns well with our Paleoproterozoic samples. Three pre-Penokean gneisses that were identified yielded crystallization ages between 2,530 and 3,200 Ma (Van Wyck and Johnson, 1997). Where our samples tell a story of both depletion (+2.8 – +5.3 and +0.4 – +3.4) and enrichment (-13.2 – -15.4), Van Wyck and Johnson (1997) samples are mostly enriched with Paleoproterozoic initial εNd values between (-1.49 – -6.67). This enrichment value is somewhat comparable to the latter enrichment values which is proposed for

16MT09; however, the U-Pb clocks do not agree as 16MT09 is dated as Late Archean. Of the three pre-Penokean gneisses identified for the Marshfield Terrane, only two were examined for εNd values, -1.49 and +13.57 respectively.

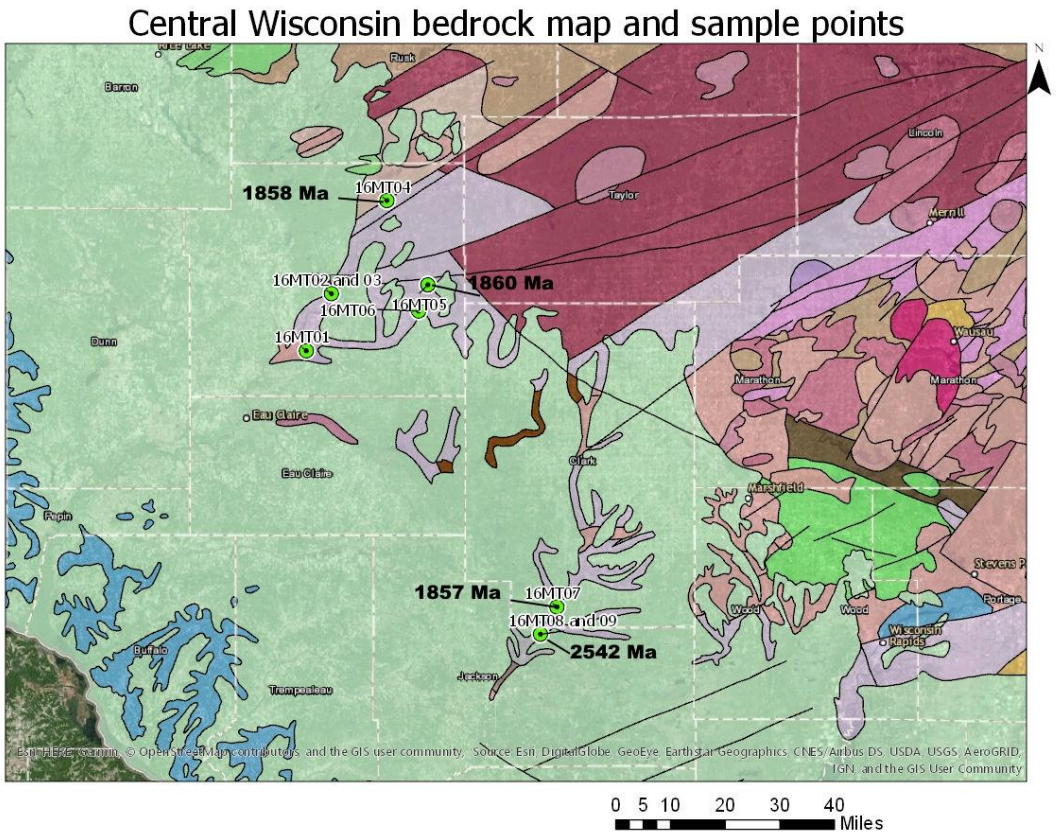

Figure 36 A map of western Wisconsin, depicting our sample locations and determined crystallization ages.

Synopsis of the Marshfield Terrane

Results presented here are often contradictory to historical studies. However, due to our small sampling size, their results cannot be excluded, and they will be combined based with this dataset. The Marshfield Terrane may be defined as a mid-Mesoarchean to late Orosirian (middle Archean to middle Paleoproterozoic) entity of metaigneous rocks which initial Hf values have

suggested to be depleted (+0.4 – +5.3) or enriched (-6.3 – -15.4). The crystallization ages described herein are consistent with Penokean Orogeny and Lu-Hf agree with previous Sm-Nd studies which indicate older source environments. Preliminary whole-rock geochemical results illustrate the role of subduction in the terrane origin and tectonic evolution and agree with previous studies that suggest the Marshfield Terrane is a displaced continental fragment, and that the Superior Province, Marshfield Terrane, and Pembine-Wausau Terrane converged together through subduction of oceanic crust during the Paleoproterozoic Penokean Orogeny.

Comparable parent terranes

Superior Province

The Superior Province and the Marshfield Terrane have been proposed to be separate entities based on Pb isotopes (Van Wyck and Johnson, 1997) and the same is suggested herein based on U-Pb geochronology, Lu-Hf geochemistry, and whole-rock geochemistry. The Superior Province is proposed to be tectonically stable since 2.6 Ga. The youngest non-detrital U-Pb reported age is 2.6 Ga (Percival, 2007). However, it should be noted one zircon from 16MT04, 16MT09 and two zircons from 16MT03 did yield ages between 2.6-2.8 Ga. Basaltic rocks from the southern Superior Province have εHf values of +8.7 –+11.3 with model ages of 3,100-2,900 Ma (Smith et al., 1987). εHf values on felsic and intermediate samples for the southern Superior Province ranged between -1.3 – +3.9 (Smith et al., 1987) whereas 16MT07 and 16MT09 proper have more negative values of -13.2 – -15.4 and -6.3 – -10.6 respectively and are likely derived from a similar crustal source. Archean aged basalts from the northern Superior Province are too old (c. 2.9 Ga) and enriched in Nb, rather than strongly depleted as seen in the Marshfield Terrane (Hollings, 2002). Samples from the western Superior Province are likely too old to be related to the Marshfield Terrane with U-Pb crystallization age/lithology provinces of 2.75-2.68

Ga, 2.7-3.0 Ga and 3.0-3.3 Ga (Davis et al., 2005). Lu-Hf data indicate model ages of 3.5 Ga (Davis et al., 2005) εHf (-1 – +3) and εNd (-2 – +1) from gneisses and granitoids from the northeastern Superior Province resemble similar εHf for the Marshfield Terrane; however, U-Pb crystallization ages are still too old (2.8-2.9 Ga) (Isnard and Gariépy, 2004). Felsic metavolcanics of Archean age domains differ in terms of their geochemistry. Lesher et al. (1986) proposed four geochemical groups of which FI (dacite and rhyodacites) has steeply dipping REE patterns and pronounced enrichment in strontium, FII (rhyodacites and rhyolites) have small slopes, FIIIa (rhyolites and high silica rhyolites) nearly flat REE patterns and enrichment of scandium, and FIIIb (rhyolites and high silica rhyolites) nearly flat REE patterns and depletion of scandium (Lesher et al., 1986). Only 16MT09 is proximal in age for comparison. 16MT09 may be comparable to the FIII which is composed of rhyolites and high silica rhyolites. FIIIa is also characterized by intermediate abundances in Sr and FIIIb exhibits a pronounced Eu anomaly. 16MT09 had silica values above 70 percent but is strongly depleted in Sr and the negative Eu anomaly isn't pronounced. The REE pattern is also not nearly flat. These data, taken together, suggests that the Marshfield terrane likely did not originate as a rift fragment of the Superior craton, reattached during the Penokean Orogeny.

Wyoming Province

The Wyoming Province has been extensively investigated by Miller, Wooden and others, but much of the data collected are too old for the Marshfield Terrane (2.7-4.0 Ga) (Mueller et al., 2014; Mueller and Wooden, 2012; Frost et al., 2006) as we have been able to define thus far. Lu-Hf data are available for Hadean and early Archean (Mueller and Wooden, 2012) but studies on younger samples are limited to Nd data. εNd on Late Archean igneous rocks lie between -1.5 – -3.1, but crystallization ages lie between 2.74-2.79 Ga (Wooden and Mueller, 1988). These rocks

are also distinctly enriched $^{207}Pb/^{204}Pb$ signature (Mueller and Frost, 2006), which did not appear to be so in Pb isotopic studies by Van Wyck and Johnson (1997). A similar result comes from the Archean Sask Craton, a proposed rift fragment of the Wyoming Province (Bickford et al., 2005). It yields three U-Pb zircon age domains of 2,450-3,100 Ma and has elevated an elevated Pb isotopic signature similar to the Wyoming Province (Bickford et al., 2005).

Comparisons with the Northern Wyoming province

The northern Wyoming Province has two terranes which merit further investigation, the Beartooth-Bighorn magmatic terrane and the Montana Metasedimentary Terrane. The Montana Metasedimentary Terrane consists of mostly metasedimentary rocks with ages between 3.2-3.0 and as such, is questionable to be associated with Marshfield Terrane. The Beartooth-Bighorn magmatic terrane consists of 2.90 – 2.74 Ga Archean magmatic rocks which have typical continental arc signatures (Mogk et al., 1992) with calc-alkaline affinities and enrichment in K (Frost et al., 2003). The samples feature strong depletions in Nb and Ti (Mueller and Wooden, 1988) with initial εNd values between -1.5 – -3.2 (Wooden and Mueller, 1988). Two series of metamorphism are known for these rocks with pressures of 6 kBar and temperatures between 750-800 Celsius and pressures of 5 kBar and temperatures between 575-625 Celsius respectively. Through the utilization of a hornblende-plagioclase thermometer, suggested metamorphic temperatures for the Marshfield Terrane 606-646°C and pressures between 5.74-6.64 Kbar have been proposed for presumed Archean amphibolite (Hafften and Radwany, 2018). Hannack and Radwany (2018) utilized a sample from the Eau Claire River Complex for edenite-richterite thermometry in a presumed late Archean metagabbro. The sample had undergone temperatures between 719-769°C (Upper Amphibolite facies) (Hannack and Radwany, 2018). While the rocks have both undergone similar temperatures and pressures, the timing of these

events is uncertain, which prevents a more in-depth comparison. If there is a correlation between the Marshfield Terrane and the Wyoming Province, more sampling would be needed from both terranes to ensure a proper identification.

Medicine Hat Block

The Medicine Hat Block is another small crustal entity like the Marshfield Terrane, which plays an important role in the amalgamation of Laurentia, and still is poorly understood – most of the terrane lies under Phanerozoic cover (LaDouceur et al., 2018). The Medicine Hat Block consists of Archean aged strata (2.6-3.1 Ga) and Proterozoic c. (1.75 Ga) (Gifford et al., 2018). U-Pb ages on Archean aged strata are between 2.4-3.3 Ga (median is 2.6-2.8 Ga) with Sm-Nd model ages depicting a 3.1-4.0 Ga source environment. εNd values range between -0.9 – -10.5. Paleoproterozoic (1.78-1.82 Ga) samples from LaDouceur et al., (2018) reveal εHf between -6.8 – -21. εHf may comparable to the Marshfield Terrane, recall initial values of -6.3 – -10.6 for Archean samples and εHf between +0.4-+5.3 and -13.2 – -15.4 for early Proterozoic samples. U-Pb Paleoproterozoic ages for the Marshfield Terrane lie between 1,857-1,860 Ma and may be a match to the Medicine Hat Block.

Conclusions

The Marshfield Terrane is a c. 3.2 – 1.8 Ga rift fragment with possible ties to either the Beartooth-Bighorn Magmatic Terrane of the Wyoming Province or the Medicine Hat Block. These rocks have geochemical depletions and trace elemental compositions which indicate the role of subduction in the terrane origin and tectonic evolution, in agreement with models from previous studies. Lu-Hf studies reaffirm these rocks have an older source environment and have been reworked tectonically. The Marshfield Terrane is not likely to be a fragment of the Superior

Province based on geochronology, zircon geochemistry and whole-rock geochemistry. An association between the Marshfield Terrane, the Beartooth-Bighorn Magmatic Terrane of the Wyoming Province and the Medicine Hat Block cannot be assessed in more detail because these terranes are still poorly constrained. To best constrain an origin, in-depth zircon trace element geochemistry, with additional U-Pb and Lu-Hf sampling will be needed from all three continental bodies. These examinations would be strengthened with whole-rock geochemistry and in-depth petrographic analyses. To recap:

1. The Marshfield Terrane from this study indicate U-Pb crystallization ages of Late Orosirian – Neoarchean. Older ages proposed by Sims and others (Paleo/Mesoarchean) cannot be excluded at this time.
2. Lu-Hf isotopic studies indicate that these rocks are much more complex than previous studies have suggested with both depleted and enriched histories for the samples of the Marshfield Terrane. Model ages suggest Rhyacian to Paleoarchean sources.
3. Geochemical data herein, combined with previous studies, strongly suggest that these samples were produced in volcanic arc and continental arc systems and experienced contamination from source rocks during the Paleoproterozoic Orogenic event in a subduction-related tectonic regime.
4. U-Pb and Lu-Hf/Sm-Nd analyses from the Superior Province do not seem to correlate as well to the Marshfield Terrane, the Wyoming Province, or the Medicine Hat Block.

To better constrain the Marshfield Terrane, more extensive U-Pb dating is needed to understand the relationship between the Archean and Paleoproterozoic age domains. Is it a progressive sequence? Will expanded sampling better explain the relationship of the two age

domains as seen in Fig. 31? How does this change our view on the Penokean Orogeny? With more in-depth sampling, what can be learned about Paleoproterozoic tectonics?

Acknowledgements

This research was partially funded by the department of Geological Sciences at Ball State University. I would like to thank them for supplying an assistantship for the past two years as well as assisting in travel to the University of Arizona. This work could not have been completed without significant support from my thesis chair, thesis committee, faculty of the department, as well as support from my colleagues, family and friends.

Appendix A: XRF data:

SAMPLE NAME	Na2O wt%	MgO wt%	Al_2O_3 wt%	SiO_2 wt%	P_2O_5 wt%	K2O wt%	CaO wt%	Sc ppm	TiO2 wt%	V ppm
16 MT 01 A	4.655	4.494	16.68	67.97	0.323	1.642	4.406	18.212	0.735	89.317
16 MT 01 B	4.498	4.547	16.033	66.361	0.314	1.78	4.375	18.45	0.758	80.508
16 MT 02 A	2.936	2.711	17.135	84.547	0.058	9.599	0	15.957	0.027	7.398
16 MT 02 B	2.721	2.732	16.912	83.838	0.057	9.533	0	15.853	0.025	4.503
16 MT 03 A	3.631	3.331	15.396	85.837	0.103	5.125	0.545	10.972	0.223	26.409
16 MT 03 B	4.02	3.187	15.361	85.781	0.098	5.136	0.569	11.065	0.217	13.619
16 MT 04 A	2.125	6.491	14.92	48.358	0.462	0.886	8.654	24.241	1.107	291.048
16 MT 04 B	2.26	6.467	14.817	47.783	0.457	0.914	8.637	21.79	1.125	257.881
16 MT 05 A	4.211	2.566	14.822	71.8	0.078	1.326	3.672	12.615	0.251	25.335
16 MT 05 B	3.954	2.415	14.76	71.486	0.081	1.27	3.697	16.343	0.246	34.709
16 MT 06 A	2.222	5.77	13.086	48.446	0.228	0.995	8.89	21.242	0.94	265.608
16 MT 06 B	2.239	6.248	13.244	49.093	0.248	0.975	8.957	29.985	0.934	297.918
16 MT 07 A	3.258	2.202	11.605	78.441	0.04	4.05	0.029	7.158	0.187	6.502
16 MT 07 B	3.459	1.852	11.55	78.113	0.04	4.044	0.031	7.3	0.183	6.714
16 MT 08 A	0.2	10.167	16.539	53.975	1.321	6.837	1.737	11.275	0.807	165.977
16 MT 08 B	0.819	11.232	16.666	54.136	1.352	6.789	1.689	10.306	0.821	136.623
16 MT 09 A	2.217	4.819	18.409	72.635	0.109	7.919	0.01	11.281	0.367	37.175
16 MT 09 B	1.114	3.484	18.339	71.971	0.092	7.988	0.026	11.601	0.378	39.671
XX MT X1 Sand	2.142	4.228	1.17	103.998	0.04	0.034	1.149	2.37	0.016	0
XX MT X2 Sand	2.128	4.082	1.222	101.404	0.043	0.035	1.105	2.377	0.015	0

SAMPLE NAME	Cr ppm	MnO wt%	Fe2O3 wt%	Co ppm	Ni ppm	Y ppm	Zr ppm	Nb ppm	Ba ppm	Pb ppm
16 MT 01 A	66.581	0.097	5.373	24.743	27.061	5.527	171.063	4.911	791.245	10.1
16 MT 01 B	47.303	0.107	5.474	25.875	20.309	9.359	162.9	4.783	757.797	10.54
16 MT 02 A	20.992	-0.018	0.504	4.49	1.944	0.467	6.698	1.514	334.909	20.941
16 MT 02 B	16.322	-0.018	0.49	2.846	0	0	0	1.514	315.543	24.885
16 MT 03 A	7.669	0.025	1.765	6.887	13.014	9.321	148.474	5.369	1191.22	12.611
16 MT 03 B	10.797	0.025	1.744	6.212	2.661	9.991	145.797	4.299	1138.58	11.049
16 MT 04 A	77.033	0.192	11.472	59.285	40.331	13.431	74.638	10.786	418.452	9.77
16 MT 04 B	73.967	0.182	11.519	54.94	37.419	18.004	72.563	11.571	438.365	9.586
16 MT 05 A	13.941	0.08	2.496	10.52	14.145	1.621	90.735	5.419	682.307	9.503
16 MT 05 B	16.804	0.08	2.463	11.485	4.133	0.736	80.107	8.837	773.95	9.503
16 MT 06 A	115.621	0.253	10.994	50.118	38.915	19.127	66.065	4.768	426.566	10.942
16 MT 06 B	118.399	0.248	11.049	45.598	50.095	14.299	65.332	5.149	346.349	10.208
16 MT 07 A	0	0.03	2.26	2.627	10.819	40.217	223.976	28.855	874.516	9.503
16 MT 07 B	0	0.034	2.212	7.182	11.007	42.301	228.308	31.225	863.569	9.503
16 MT 08 A	245.439	0.152	8.716	42.521	109.921	33.967	90.846	15.282	223.392	11.35
16 MT 08 B	238.143	0.156	8.766	42.182	126.775	35.978	87.135	14.79	100.319	11.173
16 MT 09 A	0	0.052	3.564	10.734	10.826	35.044	287.956	15.143	777.966	10.819
16 MT 09 B	0	0.053	3.596	8.684	31.96	37.179	285.496	16.044	720.112	9.503
XX MT X1 Sand	5.131	-0.022	0.411	4.429	3.931	2.381	29.711	1.514	65.675	9.503
XX MT X2 Sand	9.464	-0.023	0.409	2.191	0.415	0.571	32.832	1.514	53.98	9.503

SAMPLE NAME	Cu ppm	Zn ppm	Ga ppm	Rb ppm	Sr ppm
16 MT 01 A	15.709	86.131	22.68	27.644	871.931
16 MT 01 B	29.148	87.406	23.575	29.053	877.406
16 MT 02 A	9.62	72.266	25.069	242.616	252.551
16 MT 02 B	14.943	71.63	23.218	243.904	256.216
16 MT 03 A	49.972	121.532	22.518	106.627	221.553
16 MT 03 B	62.003	120.957	26.366	111.006	226.06
16 MT 04 A	44.644	94.918	17.881	14.479	500.26
16 MT 04 B	41.79	92.349	20.211	14.201	494.787
16 MT 05 A	10.917	81.1	24.848	36.705	755.448
16 MT 05 B	9.49	82.166	25.682	34.417	754.334
16 MT 06 A	11.874	84.614	18.691	11.572	219.939
16 MT 06 B	20.905	88.986	17.347	9.542	223.734
16 MT 07 A	8.752	76.463	24.001	85.411	73.266
16 MT 07 B	11.504	77.675	23.905	85.592	72.562
16 MT 08 A	14.613	91.331	15.182	62.962	25.219
16 MT 08 B	24.25	92.29	12.574	62.768	27.942
16 MT 09 A	18.77	76.452	23.427	191.467	37.382
16 MT 09 B	14.445	75.892	24.945	186.989	36.05
XX MT X1 Sand	7.526	74.042	3.786	0.093	63.902
XX MT X2 Sand	1.026	71.717	6.048	2.638	64.067

Appendix B: ICP-MS Geochemical data:

Sample	Al (wt. %)	Ba (ppm)	Be (ppm)	Ca (wt. %)	Cr (ppm)	Cu (ppm)	Fe (wt. %)
16MT01	8.63	777	<5	3.3	278	24	3.77
16MT02	7.36	432	<5	0.2	240	14	0.3
16MT03	7.45	1160	<5	1.2	472	18	1.16
16MT04	9.72	325	<5	6.6	132	67	8.76
16MT05	8.17	854	<5	3.5	1113	88	5.19
16MT06	8.9	625	<5	6.5	131	20	8.26
16MT07	6.03	1001	<5	0.2	438	11	2.27
16MT08	8.29	179	<5	1.9	249	26	5.8
16MT09	7.24	770	<5	0.2	278	11	2.05
REP-16MT09	7.24	775	<5	0.2	344	12	2.13

Sample	K (wt. %)	Li (ppm)	Mg (Wt. %)	Mn (ppm)	Ni (ppm)	P (Wt. %)	Sc (ppm)
16MT01	1.4	22	1.13	688	21	0.09	10
16MT02	7.9	<10	0.02	30	7	<0.01	<5
16MT03	3.2	13	0.3	175	15	0.03	<5
16MT04	0.8	10	2.75	1528	38	0.15	33
16MT05	1.5	20	1.59	726	58	0.08	12
16MT06	0.9	14	2.74	1882	21	0.08	35
16MT07	3.9	<10	0.18	263	18	0.01	<5
16MT08	5.1	21	4	951	102	0.78	21
16MT09	6.5	<10	0.63	137	20	0.04	<5
REP-16MT09	6.5	<10	0.64	147	21	0.04	<5

Sample	Si (wt. %)	Sr (ppm)	Ti (wt. %)	V (ppm)	Zn (ppm)	Ag (ppm)	As (ppm)
16MT01	28.9	815	0.39	76	83	<1	<5
16MT02	>30	196	<0.01	<5	20	<1	<5
16MT03	>30	226	0.07	15	146	<1	<5
16MT04	22.7	650	0.69	268	109	<1	<5
16MT05	27.6	497	0.44	90	74	<1	<5
16MT06	23.9	291	0.62	275	84	<1	<5
16MT07	>30	62	0.08	6	32	<1	<5
16MT08	23.4	39	0.44	131	90	<1	<5
16MT09	>30	37	0.19	30	26	<1	<5
REP-16MT09	>30	37	0.19	29	26	<1	<5

Sample	Bi (ppm)	Cd (ppm)	Ce (ppm)	Co (ppm)	Cs (ppm)	Dy (ppm)	Er (ppm)
16MT01	<0.1	<0.2	56.1	13.1	0.4	2.06	1.05

16MT02	<0.1	0.9	1.5	0.6	0.8	0.26	0.15
16MT03	<0.1	0.5	61.6	3.8	0.5	2.14	1.15
16MT04	<0.1	<0.2	33.3	32.2	0.6	3.28	1.98
16MT05	<0.1	<0.2	40.2	21.5	1.5	2.03	1.16
16MT06	0.2	<0.2	22.1	28.9	0.3	4.46	2.79
16MT07	0.2	<0.2	75.6	2	0.5	5.91	4.06
16MT08	<0.1	<0.2	65	35.5	2.4	6.1	2.67
16MT09	<0.1	<0.2	132	6.4	2	5.69	3.08
REP-16MT09	<0.1	<0.2	129	6.4	2.2	5.7	3.15

Sample	Eu (ppm)	Ga (ppm)	Gd (ppm)	Ge (ppm)	Hf (ppm)	Ho (ppm)	In (ppm)
16MT01	1.03	20	2.67	<1	4	0.38	<0.2
16MT02	0.12	14	0.21	1	<1	0.05	<0.2
16MT03	0.51	16	3	<1	5	0.38	<0.2
16MT04	1.1	21	3.19	2	3	0.65	<0.2
16MT05	0.75	18	2.3	1	2	0.37	<0.2
16MT06	1.04	16	3.92	2	2	0.93	<0.2
16MT07	0.43	16	5.17	<1	5	1.27	<0.2
16MT08	2.02	14	8.16	<1	2	1.06	<0.2
16MT09	0.97	20	6.11	<1	8	1.08	<0.2
REP-16MT09	0.94	20	6.18	<1	8	1.08	<0.2

Sample	La (ppm)	Lu (ppm)	Mo (ppm)	Nb (ppm)	Nd (ppm)	Pb (ppm)	Pr (ppm)
16MT01	28.1	0.24	4	5	21.1	11	5.81
16MT02	1	0.05	3	<1	0.8	48	0.19
16MT03	33.5	0.17	6	4	25.5	27	7.11
16MT04	16.5	0.31	<2	10	17.3	6	4.4
16MT05	21	0.18	13	13	16.8	10	4.41
16MT06	10.2	0.41	<2	4	13.5	9	3.06
16MT07	32.3	0.63	10	18	27.8	6	7.57
16MT08	41.9	0.34	<2	12	36	6	8.68
16MT09	71.3	0.42	4	14	53.4	7	15.5
REP-16MT09	69.4	0.41	5	14	51.2	7	15.1

Sample	Rb (ppm)	Sb (ppm)	Sm (ppm)	Sn (ppm)	Ta (ppm)	Tb (ppm)	Th (ppm)
16MT01	31.4	<0.1	3.4	3	<0.5	0.35	5.2
16MT02	165	0.1	0.2	<1	<0.5	<0.05	0.1
16MT03	61.7	<0.1	4.2	2	0.5	0.38	16.2
16MT04	18.2	0.2	3.3	2	<0.5	0.5	3.4
16MT05	58.7	0.2	2.9	5	0.8	0.32	7.1

16MT06	15.3	0.2	3.3	8	<0.5	0.65	3.5
16MT07	74.9	0.1	5.4	2	1	0.85	13.7
16MT08	72.8	0.1	7.8	1	0.6	1.08	2
16MT09	167	<0.1	8.1	4	1.1	0.91	36.5
REP-16MT09	166	0.1	8.1	2	1.1	0.9	35.6

Sample	Tl (ppm)	Tm (ppm)	U (ppm)	W (ppm)	Y (ppm)	Yb (ppm)	Zr (ppm)
16MT01	<0.5	0.14	1.44	<1	9.7	0.9	170
16MT02	1	<0.05	0.89	<1	1.4	0.2	7.9
16MT03	<0.5	0.16	2.51	<1	10.7	1	162
16MT04	<0.5	0.29	0.57	<1	17.8	1.9	112
16MT05	<0.5	0.16	2.33	<1	10.2	1.1	80
16MT06	<0.5	0.39	0.99	<1	23.7	2.7	78.4
16MT07	<0.5	0.6	3.45	<1	32.1	4.2	162
16MT08	<0.5	0.34	10.8	<1	29.9	2.2	91.2
16MT09	0.9	0.43	2.17	<1	29.2	2.8	281
REP-16MT09	0.9	0.43	2.16	<1	29.4	2.8	292

Appendix C: U-Pb data table

16MT03

Analysis	207Pb/235U	7/5 error	206Pb/238U	6/8 error	error correlation	Best age (Ma)	± (Ma)	Concordance (%)
16TM03 Spot 42	4.75	1.39	0.32	1.23	0.89	1782.36	11.59	99.32
16TM03 Spot 60	4.75	1.90	0.31	1.79	0.94	1797.50	11.58	97.85
16TM03 Spot 54	4.86	1.59	0.32	1.40	0.88	1800.65	13.62	99.36
16TM03 Spot 39	4.92	1.55	0.32	1.39	0.89	1808.87	12.71	99.74
16TM03 Spot 43	5.18	2.01	0.34	1.83	0.91	1827.20	15.21	102.37
16TM03 Spot 47	5.05	1.40	0.33	1.18	0.84	1836.40	13.89	99.05
16TM03 Spot 53	5.67	1.72	0.34	1.40	0.81	1945.13	18.03	98.19
16TM03 Spot 65	5.82	1.29	0.35	1.11	0.86	1951.80	11.54	99.69
16TM03 Spot 37	5.38	2.39	0.32	2.17	0.91	1979.56	17.73	90.63
16TM03 Spot 59	5.73	2.08	0.34	1.96	0.94	1991.24	12.18	94.71
16TM03 Spot 38	5.79	2.10	0.34	1.82	0.87	2008.16	18.62	93.90
16TM03 Spot 62	5.13	2.35	0.29	2.19	0.93	2052.88	15.16	80.83
16TM03 Spot 44	6.11	1.54	0.35	1.38	0.89	2068.81	12.13	92.68
16TM03 Spot 63	6.03	2.67	0.33	2.50	0.94	2132.50	16.36	86.20
16TM03 Spot 56	6.53	3.23	0.36	2.64	0.82	2135.46	32.70	92.03
16TM03 Spot 46	6.66	2.61	0.36	0.98	0.37	2138.31	42.33	93.40

16TM03 Spot 66	6.53	2.21	0.36	1.66	0.75	2139.44	25.62	91.67
16TM03 Spot 64	6.75	2.94	0.36	2.78	0.95	2160.26	16.38	92.53
16TM03 Spot 70	6.70	2.23	0.36	2.09	0.94	2186.82	13.44	89.58
16TM03 Spot 52	6.60	1.72	0.34	1.49	0.86	2234.12	15.06	84.54
16TM03 Spot 50	9.02	1.69	0.44	1.44	0.85	2332.41	15.13	100.72
16TM03 Spot 67	9.03	1.98	0.43	1.72	0.87	2361.58	16.56	98.15
16TM03 Spot 57	8.79	2.15	0.42	1.92	0.89	2383.80	16.65	94.01
16TM03 Spot 41	11.10	1.68	0.47	1.23	0.73	2564.13	19.17	97.17
16TM03 Spot 40	11.65	1.25	0.49	1.05	0.84	2569.72	11.29	100.64
16TM03 Spot 49	13.05	1.64	0.51	1.43	0.87	2696.88	13.16	98.80
16TM03 Spot 58	15.27	1.23	0.55	1.08	0.88	2841.56	9.73	99.23

16MT04

Analysis	207Pb/235U	7/5 error	206Pb/238U	6/8 error	Overall error	Best age (Ma)	± (Ma)	Concordance (%)
16TM04 Spot 32	3.87	1.33	0.28	1.09	0.82	1608.67	14.14	99.85
16TM04 Spot 21	4.97	1.80	0.33	1.65	0.92	1770.89	13.26	104.54
16TM04 Spot 15	4.79	1.81	0.31	1.62	0.90	1840.92	14.62	94.13
16TM04 Spot 22	5.27	1.69	0.34	1.47	0.87	1842.66	15.07	102.27
16TM04 Spot 35	4.69	1.90	0.30	1.74	0.92	1847.39	13.72	91.88
16TM04 Spot 28	4.80	1.60	0.31	1.42	0.89	1847.78	13.37	93.64
16TM04 Spot 01	5.35	1.32	0.34	1.19	0.90	1853.94	10.26	102.44
16TM04 Spot 06	5.07	1.78	0.32	1.58	0.88	1854.28	15.00	97.60
16TM04 Spot 30	5.53	1.31	0.35	1.16	0.88	1857.44	11.06	104.94
16TM04 Spot 24	5.42	1.52	0.35	1.29	0.85	1858.62	14.55	103.04
16TM04 Spot 25	5.43	1.69	0.35	1.50	0.89	1859.22	14.12	103.09
16TM04 Spot 12	5.21	1.49	0.33	1.27	0.85	1859.34	14.03	99.45
16TM04 Spot 27	5.31	1.46	0.34	1.30	0.89	1859.82	12.02	101.16
16TM04 Spot 02	4.44	2.14	0.28	2.03	0.95	1860.78	11.81	86.39
16TM04 Spot 18	4.86	1.77	0.31	1.60	0.91	1860.82	13.54	93.43

16TM04 Spot 08	5.25	1.76	0.33	1.58	0.90	1863.75	13.89	99.72
16TM04 Spot 31	5.29	1.46	0.34	1.14	0.78	1864.08	16.34	100.35
16TM04 Spot 26	5.28	1.61	0.34	1.52	0.94	1864.87	9.88	100.09
16TM04 Spot 33	5.14	1.60	0.33	1.40	0.87	1865.60	14.03	97.74
16TM04 Spot 16	4.75	1.75	0.30	1.59	0.91	1867.21	13.17	91.08
16TM04 Spot 03	5.16	1.76	0.33	1.59	0.90	1867.23	13.76	97.93
16TM04 Spot 20	5.37	1.72	0.34	1.59	0.92	1868.12	11.84	101.16
16TM04 Spot 29	5.39	1.74	0.34	1.55	0.89	1869.18	14.20	101.46
16TM04 Spot 19	5.12	1.43	0.32	1.16	0.81	1870.64	15.19	96.79
16TM04 Spot 13	5.17	1.38	0.33	1.11	0.80	1871.00	14.79	97.62
16TM04 Spot 07	5.13	2.05	0.32	1.82	0.89	1877.27	17.16	96.38
16TM04 Spot 23	5.21	1.51	0.33	1.30	0.86	1878.40	13.66	97.54
16TM04 Spot 11	3.87	1.33	0.28	1.09	0.82	1608.67	14.14	99.85
16TM04 Spot 14	4.97	1.80	0.33	1.65	0.92	1770.89	13.26	104.54

16MT05

Analysis	207Pb/235U	7/5 error	206Pb/238U	6/8 error	Overall error	Best age (Ma)	± (Ma)	Concordance (%)
16TM05 Spot 28	3.89	2.33	0.28	2.12	0.91	1630.54	17.99	98.01
16TM05 Spot 08	4.20	1.85	0.28	1.66	0.90	1787.16	14.71	88.70
16TM05 Spot 18	4.96	1.51	0.33	1.40	0.92	1798.15	10.64	101.56
16TM05 Spot 34	4.65	2.02	0.31	1.89	0.94	1800.94	12.68	95.62
16TM05 Spot 32	5.08	1.33	0.33	1.15	0.86	1815.79	12.20	101.69
16TM05 Spot 13	5.16	1.45	0.34	1.18	0.81	1820.77	15.48	102.55
16TM05 Spot 31	4.39	1.61	0.29	1.50	0.93	1824.15	10.69	88.72
16TM05 Spot 26	5.21	1.24	0.34	0.99	0.80	1834.20	13.62	101.99
16TM05 Spot 33	5.36	1.93	0.35	1.78	0.92	1838.32	13.30	104.18
16TM05 Spot 24	5.23	1.45	0.34	1.16	0.80	1838.96	15.75	101.94
16TM05 Spot 19	5.12	1.83	0.33	1.56	0.85	1839.73	17.36	100.04
16TM05 Spot 22	5.23	1.47	0.34	1.31	0.89	1840.45	12.28	101.81
16TM05 Spot 04	5.05	1.74	0.33	1.58	0.91	1840.96	13.11	98.68
16TM05 Spot 27	5.17	1.43	0.33	1.23	0.86	1844.61	13.31	100.28
16TM05 Spot 17	5.18	1.54	0.33	1.35	0.88	1845.83	13.33	100.44

16TM05 Spot 05	5.45	1.99	0.35	1.80	0.91	1847.77	15.25	104.64
16TM05 Spot 07	5.12	1.31	0.33	1.07	0.82	1848.17	13.55	99.18
16TM05 Spot 03	4.93	1.61	0.32	1.49	0.93	1851.56	10.79	95.60
16TM05 Spot 20	5.31	1.23	0.34	0.84	0.69	1853.87	16.06	101.63
16TM05 Spot 10	5.16	1.19	0.33	1.00	0.85	1854.49	11.44	99.07
16TM05 Spot 01	5.29	1.61	0.34	1.46	0.91	1854.82	12.33	101.24
16TM05 Spot 09	5.31	1.35	0.34	1.19	0.89	1858.31	11.32	101.26
16TM05 Spot 11	5.14	1.47	0.33	1.30	0.88	1866.98	12.47	97.58
16TM05 Spot 02	5.26	1.23	0.33	1.02	0.83	1868.77	12.39	99.40
16TM05 Spot 21	5.26	1.35	0.33	1.09	0.81	1868.86	14.27	99.36
16TM05 Spot 25	5.27	1.43	0.33	1.26	0.88	1868.99	12.24	99.51
16TM05 Spot 23	5.40	1.14	0.34	0.93	0.82	1870.59	11.75	101.39
16TM05 Spot 12	3.89	2.33	0.28	2.12	0.91	1630.54	17.99	98.01
16TM05 Spot 35	4.20	1.85	0.28	1.66	0.90	1787.16	14.71	88.70
16TM05 Spot 15	4.96	1.51	0.33	1.40	0.92	1798.15	10.64	101.56

16MT07

Analysis	207Pb/235U	7/5 error	206Pb/238U	6/8 error	Overall error	Best age (Ma)	± (Ma)	Concordance (%)
16TM07 Spot 07	4.59	1.27	0.30	1.15	0.90	1799.64	9.98	94.63
16TM07 Spot 31	5.19	1.32	0.34	1.18	0.89	1808.98	10.98	104.48
16TM07 Spot 34	5.17	1.36	0.34	1.25	0.92	1826.78	9.81	102.24
16TM07 Spot 22	5.17	1.40	0.34	1.12	0.80	1827.31	15.24	102.03
16TM07 Spot 24	5.14	1.21	0.33	1.05	0.87	1828.86	10.92	101.47
16TM07 Spot 30	5.25	1.35	0.34	1.25	0.93	1829.14	9.20	103.34
16TM07 Spot 14	5.20	1.29	0.34	1.15	0.89	1832.56	10.70	102.02
16TM07 Spot 10	4.47	1.49	0.29	1.28	0.86	1832.81	13.90	89.36
16TM07 Spot 08	5.22	1.13	0.34	0.89	0.79	1833.45	12.46	102.40
16TM07 Spot 16	5.09	1.04	0.33	0.87	0.83	1834.13	10.42	100.00
16TM07 Spot 18	5.23	1.30	0.34	1.11	0.85	1834.32	12.38	102.48
16TM07 Spot 11	5.24	1.26	0.34	1.16	0.92	1834.72	9.08	102.56
16TM07 Spot 26	5.14	1.43	0.33	1.25	0.87	1835.99	12.58	100.66
16TM07 Spot 01	5.26	1.17	0.34	1.04	0.89	1836.58	9.57	102.67
16TM07 Spot 28	5.14	1.52	0.33	1.37	0.90	1837.34	11.76	100.58

16TM07 Spot 35	5.12	1.22	0.33	1.02	0.83	1839.58	12.35	100.01
16TM07 Spot 02	5.20	1.21	0.34	1.01	0.83	1839.64	12.16	101.39
16TM07 Spot 23	5.21	1.49	0.34	1.35	0.91	1841.36	11.09	101.27
16TM07 Spot 19	5.38	1.23	0.35	1.10	0.89	1843.47	10.07	103.91
16TM07 Spot 25	5.20	1.29	0.33	1.12	0.87	1844.29	11.67	100.84
16TM07 Spot 32	5.20	1.41	0.33	1.25	0.89	1844.79	11.66	100.73
16TM07 Spot 29	4.87	1.22	0.31	1.01	0.83	1845.20	12.27	95.18
16TM07 Spot 13	5.22	1.38	0.33	1.21	0.87	1847.22	12.08	100.82
16TM07 Spot 15	5.20	1.11	0.33	0.91	0.82	1851.19	11.54	100.09
16TM07 Spot 09	5.11	1.45	0.33	1.31	0.90	1853.54	11.28	98.47
16TM07 Spot 17	5.27	1.50	0.34	1.34	0.90	1854.12	11.97	100.93
16TM07 Spot 05	5.14	1.38	0.33	1.22	0.88	1854.56	11.73	98.81
16TM07 Spot 20	4.59	1.27	0.30	1.15	0.90	1799.64	9.98	94.63
16TM07 Spot 03	5.19	1.32	0.34	1.18	0.89	1808.98	10.98	104.48
16TM07 Spot 33	5.17	1.36	0.34	1.25	0.92	1826.78	9.81	102.24
16TM07 Spot 21	5.17	1.40	0.34	1.12	0.80	1827.31	15.24	102.03
16TM07 Spot 04	5.14	1.21	0.33	1.05	0.87	1828.86	10.92	101.47

16TM07 Spot 06	5.25	1.35	0.34	1.25	0.93	1829.14	9.20	103.34
16TM07 Spot 27	5.20	1.29	0.34	1.15	0.89	1832.56	10.70	102.02
16TM07 Spot 12	4.47	1.49	0.29	1.28	0.86	1832.81	13.90	89.36

16MT09

Analysis	207Pb/235U	7/5 error	206Pb/238U	6/8 error	Overall error	Best age (Ma)	± (Ma)	Concordance (%)
16TM09 Spot 43	9.98	1.71	0.44	1.57	0.92	2504.17	11.30	93.78
16TM09 Spot 41	10.56	1.47	0.46	1.32	0.89	2506.75	11.12	98.06
16TM09 Spot 49	11.28	1.16	0.49	0.94	0.81	2517.85	11.53	102.60
16TM09 Spot 44	10.68	1.14	0.46	0.88	0.77	2527.78	12.22	97.18
16TM09 Spot 42	11.04	1.02	0.48	0.78	0.76	2528.38	11.02	99.84
16TM09 Spot 45	11.36	1.31	0.49	1.02	0.78	2530.97	13.80	101.97
16TM09 Spot 56	11.34	1.22	0.49	0.98	0.80	2531.58	12.26	101.77
16TM09 Spot 64	11.06	1.07	0.48	0.93	0.87	2533.34	8.94	99.56
16TM09 Spot 48	11.11	0.88	0.48	0.71	0.81	2533.77	8.76	99.88
16TM09 Spot 36	11.47	1.12	0.50	0.95	0.85	2536.97	9.99	102.22
16TM09 Spot 52	11.41	1.11	0.49	0.89	0.80	2537.57	11.15	101.72
16TM09 Spot 38	11.11	0.89	0.48	0.72	0.81	2538.77	8.82	99.47
16TM09 Spot 59	10.76	1.11	0.46	0.92	0.83	2539.16	10.51	96.81
16TM09 Spot 51	10.39	1.07	0.45	0.92	0.86	2539.79	9.31	93.93

16TM09 Spot 61	11.05	1.31	0.47	1.11	0.84	2544.66	11.89	98.44
16TM09 Spot 60	11.25	1.49	0.48	1.32	0.88	2545.37	11.70	99.87
16TM09 Spot 54	11.24	1.14	0.48	0.98	0.86	2545.59	9.76	99.80
16TM09 Spot 58	11.17	1.09	0.48	0.96	0.88	2546.55	8.57	99.21
16TM09 Spot 53	11.42	1.25	0.49	0.98	0.78	2546.75	13.04	101.03
16TM09 Spot 39	11.18	1.05	0.48	0.82	0.77	2548.09	11.17	99.12
16TM09 Spot 57	10.90	1.21	0.47	1.03	0.85	2548.31	10.69	97.04
16TM09 Spot 63	10.66	1.08	0.46	0.92	0.85	2548.52	9.60	95.26
16TM09 Spot 47	10.63	1.20	0.46	1.00	0.83	2550.18	11.08	94.89
16TM09 Spot 62	11.59	1.19	0.50	0.96	0.81	2552.02	11.82	101.74
16TM09 Spot 40	11.56	0.97	0.49	0.78	0.80	2556.24	9.79	101.18
16TM09 Spot 46	11.37	1.27	0.49	1.08	0.85	2556.28	11.20	99.78
16TM09 Spot 50	11.43	1.06	0.49	0.84	0.79	2557.36	10.80	100.14
16TM09 Spot 37	9.98	1.71	0.44	1.57	0.92	2504.17	11.30	93.78

Appendix D: Lu-Hf Data Table

16MT04

Sample	(^{176}Yb + ^{176}Lu) / ^{176}Hf (%)	Volts Hf	^{176}Hf/^{177}Hf	± (1σ)	^{176}Lu/^{177}Hf	^{176}Hf/^{177}Hf (T)	E-Hf (0)	E-Hf (0) ± (1σ)	E-Hf (T)	Age (Ma)
16MT04 Spot 01	11.6	5.1	0.281734	0.000016	0.000928	0.281701	-37.2	0.6	3.5	1854
16MT04 Spot 03	27.4	4.1	0.281745	0.000024	0.001961	0.281676	-36.8	0.9	2.9	1867
16MT04 Spot 06	14.8	4.0	0.281718	0.000023	0.001074	0.281680	-37.7	0.8	2.8	1854
16MT04 Spot 08	21.3	5.1	0.281771	0.000014	0.001499	0.281718	-35.9	0.5	4.4	1864
16MT04 Spot 12	14.8	5.4	0.281727	0.000022	0.000977	0.281692	-37.4	0.8	3.3	1859
16MT04 Spot 13	12.7	4.9	0.281775	0.000020	0.000967	0.281740	-35.7	0.7	5.3	1871
16MT04 Spot 24	34.9	5.4	0.281801	0.000020	0.002292	0.281720	-34.8	0.7	4.3	1859
16MT04 Spot 26	5.5	5.6	0.281914	0.000025	0.000510	0.281896	-30.8	0.9	10.7	1865
16MT04 Spot 27	19.8	5.2	0.281703	0.000019	0.001316	0.281656	-38.3	0.7	2.1	1860
16MT04 Spot 29	22.0	4.8	0.281720	0.000017	0.001529	0.281665	-37.7	0.6	2.6	1869
16MT04 Spot 31	17.3	5.6	0.281741	0.000017	0.001226	0.281698	-36.9	0.6	3.7	1864
16MT04 Spot 33	20.8	5.2	0.281766	0.000015	0.001460	0.281714	-36.0	0.5	4.3	1866

16MT05

Sample	(^{176}Yb + ^{176}Lu) / ^{176}Hf (%)	Volts Hf	^{176}Hf/^{177}Hf	± (1σ)	^{176}Lu/^{177}Hf	^{176}Hf/^{177}Hf (T)	E-Hf (0)	E-Hf (0) ± (1σ)	E-Hf (T)	Age (Ma)
16MT05 Spot 01	32.2	5.5	0.281708	0.000017	0.002011	0.281638	-38.1	0.6	1.3	1855
16MT05 Spot 02	8.3	5.4	0.281668	0.000020	0.000531	0.281649	-39.5	0.7	2.0	1869
16MT05 Spot 04	16.4	7.9	0.281176	0.000020	0.001124	0.281136	-56.9	0.7	-16.8	1841
16MT05 Spot 07	26.3	5.2	0.281739	0.000019	0.001792	0.281676	-37.0	0.7	2.5	1848
16MT05 Spot 10	6.1	5.4	0.281632	0.000021	0.000427	0.281617	-40.8	0.7	0.6	1855
16MT05 Spot 17	6.7	6.0	0.281634	0.000019	0.000485	0.281617	-40.7	0.7	0.4	1846
16MT05 Spot 22	23.9	4.9	0.281758	0.000022	0.001512	0.281705	-36.3	0.8	3.4	1840
16MT05 Spot 24	9.0	5.7	0.281712	0.000020	0.000590	0.281691	-38.0	0.7	2.8	1839
16MT05 Spot 25	7.3	5.7	0.281662	0.000019	0.000495	0.281644	-39.7	0.7	1.9	1869
16MT05 Spot 27	27.4	5.4	0.281690	0.000015	0.001705	0.281631	-38.7	0.5	0.8	1845

16MT07

Sample	(^{176}Yb + ^{176}Lu) / ^{176}Hf (%)	Volts Hf	^{176}Hf/^{177}Hf	± (1σ)	^{176}Lu/^{177}Hf	^{176}Hf/^{177}Hf (T)	E-Hf (0)	E-Hf (0) ± (1σ)	E-Hf (T)	Age (Ma)
16MT07 Spot 02	46.2	5.6	0.281303	0.000023	0.002710	0.281208	-52.4	0.8	-14.3	1840
16MT07 Spot 05	29.8	5.7	0.281231	0.000021	0.001831	0.281166	-55.0	0.7	-15.4	1855
16MT07 Spot 13	38.8	6.2	0.281274	0.000018	0.002265	0.281195	-53.4	0.7	-14.6	1847
16MT07 Spot 15	34.2	5.1	0.281254	0.000017	0.002073	0.281181	-54.1	0.6	-15.0	1851
16MT07 Spot 17	32.7	5.4	0.281268	0.000019	0.001921	0.281200	-53.7	0.7	-14.3	1854
16MT07 Spot 20	26.7	4.8	0.281759	0.000023	0.001570	0.281703	-36.3	0.8	3.6	1856
16MT07 Spot 23	35.3	4.9	0.281289	0.000017	0.002071	0.281216	-52.9	0.6	-14.0	1841
16MT07 Spot 25	32.3	5.9	0.281284	0.000020	0.001899	0.281217	-53.1	0.7	-13.9	1844
16MT07 Spot 26	31.6	6.2	0.281308	0.000019	0.001882	0.281242	-52.2	0.7	-13.2	1836
16MT07 Spot 28	44.9	5.3	0.281313	0.000018	0.002586	0.281222	-52.1	0.6	-13.9	1837
16MT07 Spot 32	28.9	6.7	0.281268	0.000014	0.001724	0.281208	-53.6	0.5	-14.2	1845
16MT07 Spot 35	22.4	5.0	0.281254	0.000017	0.001314	0.281208	-54.2	0.6	-14.3	1840

16MT09

Sample	(^{176}Yb + ^{176}Lu) / ^{176}Hf (%)	Volts Hf	^{176}Hf/^{177}Hf	± (1σ)	^{176}Lu/^{177}Hf	^{176}Hf/^{177}Hf (T)	E-Hf (0)	E-Hf (0) ± (1σ)	E-Hf (T)	Age (Ma)
16MT09 Spot 36	21.6	5.8	0.280985	0.000015	0.001195	0.280927	-63.7	0.5	-8.1	2537
16MT09 Spot 38	18.0	5.2	0.280996	0.000021	0.000976	0.280949	-63.3	0.7	-7.3	2539
16MT09 Spot 39	20.3	5.3	0.280976	0.000015	0.001211	0.280917	-64.0	0.5	-8.2	2548
16MT09 Spot 46	18.7	5.1	0.280983	0.000013	0.001138	0.280927	-63.7	0.5	-7.6	2556
16MT09 Spot 48	15.0	4.7	0.281033	0.000021	0.001102	0.280980	-62.0	0.8	-6.3	2534
16MT09 Spot 52	38.0	4.4	0.281588	0.000032	0.002704	0.281457	-42.3	1.1	10.7	2538
16MT09 Spot 53	13.3	5.4	0.280972	0.000018	0.000823	0.280932	-64.1	0.6	-7.7	2547
16MT09 Spot 54	25.3	5.3	0.281252	0.000023	0.001434	0.281182	-54.2	0.8	1.1	2546
16MT09 Spot 58	11.6	6.6	0.280974	0.000014	0.000714	0.280939	-64.1	0.5	-7.5	2547
16MT09 Spot 60	20.4	5.9	0.280901	0.000018	0.001006	0.280852	-66.6	0.7	-10.6	2545
16MT09 Spot 61	11.0	6.6	0.280981	0.000017	0.000677	0.280948	-63.8	0.6	-7.2	2545

References

Afifi, A., Doe, B.R., Sims, P.K., and Delevaux, M.H., 1984, U-Th-Pb isotope chronology of sulfide ores and rocks in the Early Proterozoic metavolcanic belt of Northern Wisconsin: Economic Geology, v. 79, p. 338-353.

Allen, D.J., and Hinze, W.J., 1991, The Wisconsin gravity minimum; source and implications: Proceedings and abstracts for the annual Institute on Lake Superior Geology, v. 37, part 1, p. 1-3.

Anderson, J.L., and Cullers, R.L., 1987, Crust-enriched, mantle-derived tonalities in the Early Proterozoic Penokean Orogen of Wisconsin: The Journal of Geology, v. 95, no. 2, p. 139-154.

Barth, A.P., Wooden, J.L., Coleman, D.S., and Fanning, C.M., Geochronology of the Proterozoic basement of southwesternmost North America, and the origin and evolution of the Mojave crustal province: tectonics, v. 19, no. 4, p. 616-629.

Bickford, M.E., Mock, T.D., Steinhart III, W.E., Collerson, K.D., and Lewry, J.F., 2005, Origin of the Archean Sask craton and its extent within the Trans-Hudson orogen: evidence from Pb and Nd isotopic compositions of basement rocks and post-orogenic intrusions: Canadian Journal of Earth Sciences, v. 42, p. 659-684.

Blackwelder, E., 1914, A Summary of the Orogenic Epochs in the Geologic History of North America: The Journal of Geology, v. 22, no. 7, p. 633-654.

Bollmann, T.A., van der Lee, S., Frederiksen, A.W., Wolin, E., Revenaugh, J., Wiens, D.A., Darbyshire, F.A., Stein, S., Wysession, M.E., and Jurdy, D., 2019, P wave teleseismic traveltime tomography of the North American Midcontinent: Journal of Geophysical Research Solid Earth, v. 124, p. 1-18.

Card, K.D., 1990, A review of the Superior Province of the Canadian Shield, a product of Archean accretion: Precambrian Research, v. 48, p. 99-156.

Carroll, D., 1953, Weatherability of zircon: Journal of Sedimentary Petrology, v. 23, no. 2, p. 106-116.

Chandler, V.W., Boerboom, T.J., and Jursa, M.A., 2007, Penokean tectonics along a promontory-embayment margin in east-central Minnesota: Precambrian Research, v. 157, p.26-49.

Craddock, J.P., Rainbird, R.H., Davis, W.J., Davidson, C., Vervoort, J.D., Konstantinou, A., Boerboom, T., Vorhies, S., Kerber, L., and Lundquist, B., 2013, Detrital Zircon Geochronology and Provenance of the Paleoproterozoic Huron (~2.4-2.2 Ga) and Animikie (2.2-1.8 Ga) Basins, Southern Superior Province: The Journal of Geology, v. 121, p. 623-644.

Davis, D.W., Williams, I.S., and Krogh, T.E., 2003, Historical Development of Zircon Geochronology: Reviews in Mineralogy and Geochemistry, v. 53, p. 145-181.

Davis, D.W., Amelin, Y., Nowell, G.M., and Parrish, R.R., 2005, Hf isotopes in zircon from the western Superior province, Canada: Implications for Archean crustal development and

evolution of the depleted mantle reservoir: Precambrian Research, v. 140, no. 3-4, p. 132-156.

DeMatties, T.A., 2018, Effects of paleoweathering and supergene activity on volcanogenic massive sulfide (VMS) mineralization in the Penokean Volcanic Belt, northern Wisconsin, Michigan and east-central Minnesota, USA: Implications for future exploration: Ore Geology Reviews, v. 95, 216-237.

Edwards, G.H., and Blackburn, T., 2018, Detecting the extent of ca. 1.1 Ga Midcontinent Rift plume heating using U-Pb thermochronology of the lower crust: Geology, v. 46, p. 911-914.

Fisher, C.M., Loewy, S.L., Miller, C.F., Berquist, P., Van Schmus, W.R., Hatcher Jr., R.D., Wooden, J.L., and Fullagar, P.D., 2010, Whole-rock Pb and Sm-Nd isotopic constraints on the growth of southeastern Laurentia during Grenvillian orogenesis: GSA Bulletin, v. 122, no. 9-10, p. 1646-1659.

Frost, B.R., Barnes, C.G., Collins, W.J., Arculus, R.J., Ellis, D.J., and Frost, C.D., 2001, A geochemical classification for granitic rocks: Journal of Petrology, v. 41, no. 11, p. 2033-2048.

Frost, C.D., Frost, B.R., Kirkwood, R., and Chamberlain, K.R., 2006, the tonalite-trondhjemite-granodiorite (TTG) to granodiorite-granite (GG) transition in the late Archean plutonic rocks of the central Wyoming Province, v. 43, p. 1419-1444.

Geisler, T., Schaltegger, U., and Tomaschek, F., 2007, Re-equilibration of Zircon in Aqueous Fluids and Melts: Elements, v. 3, p. 43-50.

Gehrels, G., and Pecha, M., 2014, Detrital zircon U-Pb geochronology and Hf isotope geochemistry of Paleozoic and Triassic passive margin strata of western North America: Geosphere, v. 10, no. 1, p. 49-65.

Gifford, J.N., Mueller, P.A., Foster, D.A., and Mogk, D.W., 2018, Extending the realm of Archean crust in the Great Falls tectonic zone: Evidence from the Little Rocky Mountains, Montana: Precambrian Research, v. 315, p. 264-281.

Grimes, C.B., Wooden, J.L., Cheadle, M.J., and John, B.E., 2015, "Fingerprinting" tectono-magmatic provenance using trace elements in igneous zircon: Contributions to Mineralogy and Petrology, v. 170, p. 1-46.

Hafften, D., and Radwany, M., 2018, Geothermobarometry of a Precambrian amphibolite from Cornell WI: Proceedings of the Institute on Lake Superior Geology, v. 64, p. 45-46.

Hamilton, W.B., 2011, Plate tectonics began in Neoproterozoic time, and plumes from deep mantle have never operated: Lithos, v. 123, p. 1-20.

Hannack, G., and Radwany, M, 2018, Hornblende-Plagioclase thermometry of the Eau Claire River Complex, western Wisconsin: Proceedings of the Institute on Lake Superior Geology, v. 64, p. 47-48.

Harley, S.L., and Kelly, N.M., 2007, Zircon: Tiny but Timely: Elements, v. 3, p. 13-18.

Haroldson, E.L., Beard, B.L., Satkoski, A.M., Brown, P.E., and Johnson, C.M., 2018, Gold remobilization associated with Mississippi Valley-type fluids: A Pb isotope perspective: GSA Bulletin, v. 130, no. 9/10, p. 1583-1595.

Hastie, A.R., Kerr, A.C., Pearce, J.A., and Mitchell, S.F., 2007, Classification of altered volcanic island arc rocks using immobile trace elements: development of the Th-Co discrimination diagram: Journal of Petrology, v. 48, no. 12, p. 2341-2357.

Hatcher, R.D., Jr., Bream, B.R., Miller, C.L., Eckert, J.O., Jr., Fullagar, P.D., and Carrigan, C.W., 2004, Paleozoic structure of Southern Appalachian Blue Ridge Grenvillian Internal Basement Massifs, *in* Bartholomew, M.J., Corriveau, L., McLelland, J., and Tollo, R.P., eds., Proterozoic Evolution of the Grenville Orogen in North America: Geological Society of America Special Paper, Memoir 197.

Hollings, P., 2002, Archean Nb-enriched basalts in the northern Superior Province: Lithos, v. 64, no. 1-2, p. 1-14.

Hollocher, K., Robinson, P., Walsh, E., and Roberts, D., 2012, Geochemistry of amphibolite-facies volcanics and gabbros of the støren nappe in extensions west and southwest of Trondheim, western gneiss region, Norway: a key to correlations and paleotectonic settings: American Journal of Science, v. 312, p. 357-416.

Horstwood, M.S.A., Košler, J., Gehrels, G., Jackson, S.E., McLean, N.M., Paton, C., Pearson, N.J., Sircombe, K., Sylvester, P., Vermeesch, P., Bowring, J.F., Condon, D.J., and Schoene, B., 2016, Community-Derived Standards for LA-ICP-MS U-(Th-)Pb Geochronology – Uncertainty Propagation, Age Interpretation and Data Reporting: Geostandards and Geoanalytical Research, v. 40, No. 3, p. 311-332.

Hoskin, P.W.O., and Black, L.P., 2000, Metamorphic zircon formation by solid-state recrystallization of protolith igneous zircon: Journal of Metamorphic Geology, v. 18, p. 423-439.

Irving, R.D., and Van Hise, C.R., 1892, The Penokee Iron-Bearing Series of Michigan and Wisconsin: Monographs of the United States Geological Survey, v. 19, p. 1-534.

Isnard, H., and Gariépy, C., 2004, Sm-Nd, Lu-Hf and Pb-Pb signatures of gneisses and granitoids from the La Grande belt: extent of late Archean crustal recycling in the northeastern Superior Province, Canada: Geochimica et Cosmochimica Acta, v. 68, no. 5, p. 1099-1113.

James, H.L., 1954, Sedimentary Facies of Iron-Formation: Economic Geology, v. 49, no. 3, p. 235-293.

James, H.L., 1958, Stratigraphy of Pre-Keweenawan Rocks in Parts of Northern Michigan: Shorter Contributions to General Geology, Geological Survey Professional Paper 314-C, p. 27-44.

Karlstrom, K.E., Harlan, S.S., Williams, M.L., McLelland, J., Geissman, J.W., and Åhall, K.-L., 1999, Refining Rodinia: Geologic evidence for the Australia-western U.S. connection in the Proterozoic: GSA Today, v. 10, p. 1-7.

Kinney, P.D., and Maas, R., 2003, Lu-Hf and Sm-Nd isotope systems in zircon: Reviews in Mineralogy and Geochemistry, v. 53, p. 327-341.

Kelemen, P.B., Shimizu, N., and Dunn, T., 1993, Relative depletion of niobium in some arc magmas and the continental crust: partitioning of K, Nb, La, and Ce, during melt / rock reaction in the upper mantle: Earth and Planetary Science Letters, v. 120, p. 111-134.

Košler, J., and Sylvester, P.J., 2003, Present Trends and the Future of Zircon in Geochronology: Laser Ablation ICPMS: Reviews in Mineralogy and Geochemistry, v. 53, p. 243-275.

LaDouceur, B., Gifford, J., Malone, S.J., and Davis, B., 2018, The Significance of the Medicine Hat Block (Southern Alberta, Northern Montana) in the Assembly of Laurentia: New Interpretations from Single Grain Zircon U-Pb and Lu-Hf Data: Goldschmidt abstracts 1392.

Larue, D.K., and Sloss, L.L., 1980, Early Proterozoic sedimentary basins of the Lake Superior region: Geological Society of America Bulletin v. 91, part 2, p. 1836–1874.

Larue, D.K., 1981a, The Chocolay Group, Lake Superior region, U.S.A.: Sedimentologic evidence for deposition in basinal and platform settings on an early Proterozoic craton: Geological Society of America Bulletin, v. 92, part 1, p. 417-435.

Larue, D.K., 1981b, The Early Proterozoic Pre-Iron-formation Menominee Group Siliciclastic Sediments of the Southern Lake Superior Region: Evidence for Sedimentation in Platform and Basinal Settings: Journal of Sedimentary Petrology, v. 51, no. 2, p. 397-414.

Lesher, C.M., 1986, Trace-element geochemistry of ore-associated and barren, felsic metavolcanics rocks in the Superior Province, Canada: Canadian Journal of Earth Sciences, v. 23, p. 222-237.

Ludwig, K.R., 2012, User's Manual for Isoplot 3.75: A Geochronological Toolkit for Microsoft Excel: Berkeley Geochronology Center Special Publication no. 5, p. 1-75.

Ludwig, K.R., 1998, On the treatment of concordant uranium-lead ages: Geochimica et Cosmochimica Acta, v. 62, no. 4, p. 665-676.

Maass, R.S., Medaris Jr., L.G., and Van Schmus, W.R., 1980, Penokean deformation in central Wisconsin: Geological Society of America – special paper 182, p. 147-157.

Magnani, M.B., Miller, K.C., Levander, A., and Karlstrom, K., 2004, The Yavapai-Mazatzal boundary: A long-lived tectonic element in the lithosphere of southwestern North America: GSA Bulletin, v. 116, no. 7-8, p. 1-6.

Malone, S.J., McClelland, W.C., von Gosen, W., and Piepjohn, K., 2017, The earliest Neoproterozoic magmatic record of the Pearya terrane, Canadian high Arctic: Implications for Caledonian terrane reconstructions: Precambrian Research, v. 292, p. 323-349.

Malone, S.J., McClelland, W.C., von Gosen, W., and Piepjohn, K., 2018, Detrital Zircon U-Pb and Lu-Hf analysis of Paleozoic sedimentary rocks from the Pearya terrane and Ellesmerian Fold Belt (northern Ellesmere Island): A comparison with Circum-Arctic

datasets and their implications on terrane tectonics: Geological Society of America Special Paper 541, p. 1–24.

Marsden, R.W., 1955, Precambrian correlations in the Lake Superior region in Michigan, Wisconsin, and Minnesota: Proceedings of the Geological Association of Canada, v. 7, no. 2, p. 107-116.

Marshall, D., 1996, Ternplot: An Excel spreadsheet for ternary diagrams: Computers and Geosciences v. 22, no. 6. p. 697-699.

Martin, H., 1994, The Archean grey gneisses and the genesis of continental crust *in* Condie, K.C., Archean crustal evolution, p. 205-259.

McDannell, K.T., Zeitler, P.K., and Schneider, D.A., 2018, Instability of the southern Canadian Shield during the late Proterozoic: Earth and Planetary Science Letters, v. 490, p. 100-109.

Middelburg, J.J., Van Der Weijden, C.H., and Woittiez, J.R.W., 1988, Chemical processes affecting the mobility of major, minor and trace elements during weathering of granitic rocks: Chemical Geology, v. 68, p. 253-273.

Mogk, D., Mueller, P.A., and Wooden, J.L., 1992, The nature of Archean terrane boundaries: an example from the northern Wyoming Province: Precambrian Research, v. 56, no. 1, p. 155-168.

Morrison, G., 1980, Characteristics and tectonic setting of the shoshonite rock association: Lithos, v. 13, p. 97-108.

Mueller, P.A., and Frost, C.D., 2006, The Wyoming Province: a distinctive Archean craton in Laurentian North America: Canadian Journal of Earth Science, v. 43, p. 1391-1397.

Mueller, P.A., and Wooden, J.L., 1988, Evidence for Archean subduction and crustal recycling, Wyoming province: Geology, v. 16, p. 871-874.

Mueller, P.A., and Wooden, J.L., 2012, Trace Element and Lu-Hf Systematics in Hadean-Archean Detrital Zircons: Implications for Crustal Evolution: The Journal of Geology, v. 120, p. 16-30.

Mueller, P.A., Mogk, D.W., Henry, D.J., Wooden, J.L., and Foster, D.A., 2014, The plume to plate transition: Hadean and Archean Crustal Evolution in the Northern Wyoming Province, U.S.A., *in* Y. Dilek, and H. Furnes, eds., Evolution of Archean Crust and Early Life, Modern Approaches in Solid Earth Sciences 7, Springer Science + Business Media Dordrecht, p. 23-32.

Murphy, J.M., 2006, Igneous Rock Associations 7. Arc Magmatism I: Relationship between subduction and magma genesis: Geoscience Canada, v. 33, no. 4, p. 145-167.

Murphy, J.M., 2007, Igneous Rock Associations 8. Arc Magmatism II: Geochemical and isotopic characteristics: Geoscience Canada, v. 34, no. 1, p. 7-35.

NICE Working Group, 2007, Reinterpretation of Paleoproterozoic accretionary boundaries of the north-central United States based on a new aeromagnetic-geologic compilation: Precambrian research, v. 157, p. 71-79.

Nelson, B.K., and DePaolo, D.J., 1985, Rapid production of continental crust 1.7-1.9 b.y. ago; Nd isotopic evidence from the basement of the North American mid-continent: Geological Society of America Bulletin, v. 96, p. 746-754.

Nesse, W.D., 2013, Introduction to Optical Mineralogy: New York, Oxford University Press, 361 p.

Ojakangas, R.W., Morey, G.B., and Southwick, D.L., 2001, Paleoproterozoic basin development and sedimentation in the Lake Superior region, North America: Sedimentary Geology, v. 141-142, p. 319-341.

Pearce, J.A., and Cann, J.R., 1973, Tectonic setting of basic volcanic rocks determined using trace element analyses: Earth and planetary science letters, v. 19, no. 2, p. 290-300.

Pearce, J.A., and Gale, G.H, 1977, Identification of ore-deposition environment from trace-element geochemistry of associated igneous host rocks: Geological Society, London, Special Publications v. 7, no. 1, p. 14-24.

Pearce, J.A., 1983, Role of the sub-continental lithosphere in magma genesis at active continental margins. *In*: Hawkesworth, C.J. and Nurry, M.L., Eds., Continental Basalts and Mantle Xenoliths, Shiva, Nantwich, p. 230-249.

Pearce, J.A., Harris N.B.W., and Tindle, A.G., 1984, Trace element discrimination diagrams for the tectonic interpretation of granitic rocks: Journal of petrology, v. 25, no. 4, p. 956-983.

Pearce, J.A., 1996, Sources and settings of granitic rocks: Episodes, v. 19, no. 4, p. 120-125.

Percival, J.A., Sanborn-Barrie, M., Skulski, T., Stott, G.M., Helmstaedt, H., and White, D.J., 2006, Tectonic evolution of the western Superior Province from NATMAP and Lithoprobe studies: Canadian Journal of Earth Science, v. 43, p. 1085-1117.

Percival, J.A., and Helmstaedt, H., 2006, The Western Superior Province Lithoprobe and NATMAP transects: introduction and summary: Canadian Journal of Earth Sciences, v. 43, p. 743-747.

Percival, J.A., 2007, Geology and Metallogeny of the Superior Province, Canada *in* Goodfellow, W.D., ed., Mineral Deposits of Canada: A Synthesis of Major Deposit-Types, District Metallogeny, the Evolution of Geological Provinces, and Exploration Methods: Geological Association of Canada, Mineral Deposits Division, Special Publication, p. 1-27.

Percival, J.A., Skulski, T., Sanborn-Barrie, M., Stott, G.M., Leclair, A.D., Corkery, M.T., and Boily, M., 2012, Chapter 6 Geology and Tectonic evolution of the Superior Province, Canada, *in* Percival, J.A., et al., Tectonic Styles in Canada: The lithoprobe perspective: Geological Association of Canada, Special Paper 49, p. 321-378.

Rollinson, H.R., 1993, Using geochemical data: evaluation, presentation, interpretation: London, Longman Geochemistry Series, 327 p.

Rubatto, D., 2002, Zircon trace element geochemistry: partitioning with garnet and the link between U-Pb ages and metamorphism: Chemical geology, v. 184, p. 123-138.

Scherer, E.E., Whitehouse, M.J., and Münker, C., 2007, Zircon and a Monitor of Crustal Growth: Elements, v. 3, p. 19-24.

Schneider, D.A., Bickford, M.E., Cannon, W.F., Schulz, K.J., and Hamilton, M.A., 2002, Age of volcanic rocks and syndepositional iron formations, Marquette Range Supergroup: implications for tectonic setting of Paleoproterozoic iron formations of the Lake Superior region: Canadian Journal of Earth Sciences, v. 39, p. 999–1012.

Schulz, K.J., and Cannon W.F., 2007, The Penokean Orogeny in the Lake Superior region: Precambrian research, v. 157, p. 4-25.

Schoene, B., 2014, U-Th-Pb- Geochronology: Reference Module in Earth Systems and Environmental Sciences – Treatise on Geochemistry, v. 4, p. 341-378.

SGS, 2014, Rocks to Results: A practical guide to laboratory operations, 87 p.

SGS, 2018, Analytical Services Guide, 88 p.

Sims, P.K., 1976, Precambrian Tectonics and Mineral Deposits, Lake Superior Region: Society of Economic Geologists, v. 71, p. 1097-1127.

Sims, P.K., and Peterman, Z.E., 1976, Geology and Rb-Sr ages of reactivated Precambrian gneisses and granite in the Marenisco-Watersmeet area, Northern Michigan: Journal Research of the United States Geological Survey, v.4, no.4, 1976, p. 405-414.

Sims, P.K., 1980, Boundary between Archean greenstone and gneiss terranes in northern Wisconsin and Michigan: Geological Society of America Special Paper 182, p. 113-124.

Sims, P.K., Kisvarsanyi, E.B., and Morey, G.B., 1987, Geology and Metallogeny of Archean and Proterozoic Basement Terranes in the Northern Midcontinent, U.S.A. – An Overview: U.S. Geological Survey Bulletin 1815, 51 p.

Sims, P.K., Van Schmus, W.R., Schulz, K.J., and Peterman, Z.E., 1989, Tectono-stratigraphic evolution of the Early Proterozoic Wisconsin Magmatic Terranes of the Penokean orogen: Canadian Journal of Earth Sciences, v. 26, p. 2145-2158.

Sims, P.K., Schulz, K.J., and Peterman, Z.E., 1992, Geology and Geochemistry of Early Proterozoic Rocks in the Dunbar Area, Northeastern Wisconsin: U.S. Geological Survey Professional Paper 1517, 61 p.

Sims, P.K., Schulz, K.J., Dewitt, E., and Brasaemle, B., 1993, Petrography and Geochemistry of Early Proterozoic Granitoid Rocks in Wisconsin Magmatic Terranes of Penokean Orogen, Northern Wisconsin: U.S. Geological Survey Bulletin 1904, p. J1-J30.

Sinha, A.K., and McLelland, J.M., 1999, Lead isotope mapping of crustal reservoirs within the Grenville superterrane: II. Adirondack massif, New York, in Sinha, A.K., ed., Basement Tectonics, v. 13, p. 97–312.

Smith, P.E., Tatsumoto, M., and Farquhar, R.M., 1987, Zircon Lu-Hf systematics and the evolution of the Archean crust in the southern Superior Province, Canada: Contributions to Mineralogy and Petrology, v. 97, p. 93-104.

Stern, R.J., 2008, Modern-style plate tectonics began in Neoproterozoic time: An alternative interpretation of Earth's tectonic history: The Geological Society of America Special Paper 440, p. 265 – 280.

Stipp, M., Stünitz, H., Heilbronner, R., and Schmid, S.M., 2002, Dynamic recrystallization of quartz: correlation between natural and experimental conditions: Geological Society of London Special Publications, v. 200, p. 171-190.

Stockmal, G.S., Colman-Sadd, S.P., Keen, C.E., O'Brien, S.J., and Quinlan, G., 1987, Collision along an irregular margin: a regional plate tectonic interpretation of the Canadian Appalachians: Canadian Journal of Earth Sciences, v. 24, p. 1098-1107.

Sun, S., and McDonough, W.F., 1989, Chemical and isotopic systematics of oceanic basalts: implications for mantle composition and process: Geological Society of London Special Publications, v. 42, p. 313-345.

Szilas, K., 2018, A geochemical overview of Mid-Archaean Metavolcanic rocks from Southwest Greenland: Geosciences, v. 8, p. 0266-0286.

Tera, F., and Wasserburg, G.J., 1975, Precise Isotopic Analysis of Lead in Picomole and Subpicomole Quantities: Analytical Chemistry, v. 47, no. 13, p. 2214-2220.

Ueng, W.C., and Larue, D.K., 1988, The early Proterozoic structural and tectonic history of the south-central Lake Superior region: Tectonics, v. 7, no. 3, p. 369-388.

Vallini, D.A., Cannon, W.F., and Schulz, K.J., 2006, Age constraints for Paleoproterozoic glaciation in the Lake Superior Region: detrital zircon and hydrothermal xenotime ages for the Chocolay Group, Marquette Range Supergroup: Canadian Journal of Earth Sciences, v. 43, p. 571-591.

Van Schmus, W.R., 1976, Early and Middle Proterozoic History of the Great Lakes Area, North America: Philosophical Transactions of the Royal Society of London, Series A, Mathematical and Physical Sciences, v. 280, p, 605-628.

Van Schmus, W.R., and Anderson, J.L., 1977, Gneiss and migmatite of Archean age in the Precambrian basement of Central Wisconsin: Geology, v. 5, p. 45-48.

Van Schmus, W.R., Schnieder, D.A., Holm, D.K., Dodson, S., and Nelson, B.K., 2007, New insights into the southern margin of the Archean–Proterozoic boundary in the north-central United States based on U–Pb, Sm–Nd, and Ar–Ar geochronology: Precambrian Research, v. 157, p. 80-105.

Van Wyck, N.V., and Johnson, C.M., 1997, Common lead, Sm-Nd, and U-Pb constraints on petrogenesis, crustal architecture, and tectonic setting of the Penokean orogeny (Paleoproterozoic) in Wisconsin: GSA Bulletin, v. 109, no. 7, p. 799-808.

Vermeesch, P., 2018, IsoplotR: A free and open toolbox for geochronology: Geoscience Frontiers, v. 9, p. 1479-1493.

Wendt, I., and Carl, C., 1991, The statistical distribution of the mean squared weighed deviation: Chemical Geology: Isotope Geoscience Section: v. 86, no. 4, p. 275-285.

Wetherill, G.W., 1956, Discordant Uranium-Lead ages, I: Transactions, American Geophysical Union, v. 37, no. 3, p. 320-326.

Whitmeyer, S.J., and Karlstrom, K.E., 2007, Tectonic model for the Proterozoic growth of North America: Geosphere, v. 3, no. 4, p. 220-259.

Whitney, D.L., and Evans, B.W., 2010, Abbreviations for names of rock-forming minerals: American Mineralogist, v. 95, p. 185-187.

Winchester, J. A., and Floyd, P.A., 1977, Geochemical discrimination of different magma series and their differentiation products using immobile elements: Chemical geology v. 20, p. 325-343.

Winter, J.D., 2010, Principles of igneous and metamorphic petrology: New Jersey, Prentice Hall, 682 p.

Wooden, J.L., and Mueller, P.A., 1988, Pb, Sr, and Nd isotopic compositions of a suite of Late Archean, igneous rocks, eastern Beartooth Mountains: implications for crust-mantle evolution: Earth and Planetary Science Letters, v. 87, p. 59-72.

Wunderman, R.L., Wannamaker, P.E., and Young, C.T., 2018, Architecture of the hidden Penokean terrane suture and Midcontinent rift system overprint in eastern Minnesota and western Wisconsin from magnetotelluric profiling: Lithosphere, p. 1-10.

Zheng, Y-F., 2019, Subduction zone geochemistry: Geoscience Frontiers, p. 1-32.